Cosmology with Power Spectrum Measurements from Galaxy Surveys

Edward Macaulay

Department of Physics

University of Oxford

A thesis submitted for the degree of

Doctor of Philosophy

September 20, 2012

Acknowledgements

I would like to thank my supervisors Gavin Dalton and Pedro Ferreira. I would also like to thank Hume Feldman, Andrew Jaffe, Shankar Agarwal, Mike Hudson, Rick Watkins, David Marsh, Maxime Treibitsch, Thibaut Louis, Tessa Baker, Graeme Addison, Joe Zuntz, Tom Mauch, Fergus Simpson, Will Percival, Jo Dunkley, Tim Davis, Renée Hlozek, Pat Roche, and the staff and students at the astrophysics department.

Authorship

This work makes use of the publicly available codes CAMB by Lewis et al. [2000] and HALOFIT by Smith et al. [2003] to generate power spectra. The publicly available code Fisher4Cast by Bassett, Fantaye, Hlozek, & Kotze [2009] was used to forecast uncertainties on BAO Hubble parameter and angular diameter distance uncertainties, and calculate survey volumes, used in chapters 5 and 6. The modified gravity forecasts in chapter 6 used an extension to CAMB written by Tessa Baker, presented in Baker [2011].

Chapters 2 and 3 of this thesis present work from Macaulay et al. [2011] and Macaulay et al. [2012], which have both been accepted for publication in Monthly Notices of the Royal Astronomical Society. Macaulay et al. [2011] was written in collaboration with Hume Feldman, Pedro Ferreira, Mike Hudson, and Rick Watkins. Macaulay et al. [2012] was written in collaboration with Hume Feldman, Pedro Ferreira, Andrew Jaffe, Shankar Agarwal, Mike Hudson, and Rick Watkins. The peculiar velocity analysis uses moments and the COMPOSITE catalogue compiled by Hume Feldman, Rick Watkins and Mike Hudson, presented in Feldman et al. [2010] and Watkins et al. [2009]. The matrix inversion code was provided by Joe Zuntz, and the MCMC routine used to analyse the peculiar velocity catalogues was provided by Graeme Addison. The simulated catalogues were provided by Shankar Agarwal and Hume Feldman. The code to calculate the survey window functions was provided by Andrew Jaffe. In Macaulay et al. [2011] I contributed the analysis of the moments of the peculiar velocity field to estimate the underlying matter power spectrum. In Macaulay et al. [2011] I contributed the analysis of the peculiar velocity catalogues to estimate the underlying matter power spectrum, and also estimate the peculiar velocity dipole.

Chapter 5 presents results from Marsh, Macaulay, Trebitsch, & Ferreira [2012], which has been accepted for publication in Physical Review D. The forecasts for axion dark matter used an extension to

CAMB written by David Marsh. The weak lensing Fisher matrices were calculated by Maxime Trebitsch. The CMB forecasts were made with the publicly available FisherCodes software by Das [2011]. In Marsh et al. [2012] I contributed the results for the galaxy redshift survey and CMB Fisher forecasts on the cosmological parameters.

Abstract

The nature of dark matter and dark energy are currently two of the most important questions in cosmology. In this thesis, we consider studying the dark universe with the redshifts and peculiar velocities of galaxies. In the first half of the thesis, we analyse current peculiar velocity measurements of the bulk flow of our local volume to estimate the underlying dark matter power spectrum. In the second half of the thesis, we consider the prospects for measuring dark matter and dark energy with future galaxy redshift surveys, particularly via redshift space distortions. Fundamentally, bulk flow measurements and redshift space distortions are both sensitive probes of the power spectrum and growth rate of cosmic structure. In the final chapter, we directly compare power spectrum measurements with both methods.

Contents

Chapter 1

Cosmology, Dark Energy and the Power Spectrum Review

1.1 The Background Expansion

In this section we review the development of cosmology, and the evidence for dark matter and dark energy, based on introductions found in Peebles [1993], Liddle [2003] and Dodelson [2003]. The two key assumptions in cosmology are that the universe is isotropic and homogeneous. Based on these assumptions, the Freidman-Robertson-Walker (FRW) metric can be derived, as is given by

$$ds^2 = c^2dt^2 - a^2(t)\left(\frac{dr^2}{1-kr^2} + r^2d\theta^2 + r^2\sin^2\theta d\phi^2\right) , \tag{1.1}$$

where r is the comoving distance. The scale factor a is related to the redshift z by

$$a = \frac{1}{1+z} , \tag{1.2}$$

and describes the relative scale of the universe now to the scale of the universe at redshift z. The redshift is given in terms of wavelength λ by

$$z = \frac{\lambda_{\text{observed}} - \lambda_{\text{emitted}}}{\lambda_{\text{emitted}}} . \tag{1.3}$$

Hubble [1929] found that this redshift was directly proportional to the distance d to the observed galaxy

$$cz = H_0 d \ . \tag{1.4}$$

This apparent 'Hubble Flow' is due to the expansion of the Universe, and this relation is only complete for low redshifts. The subscript 0 indicates that this is the value of Hubble's constant H at redshift zero (i.e., now). The variation of H with redshift depends on the densities of various components which constitute the Universe

$$H^2(z) = H_0^2 \sum_n \Omega_n (1+z)^{3(1+w_n)} \ , \tag{1.5}$$

where the equation of state w_n is the ratio of the pressure p_n to the energy density $\rho_n c^2$, given by

$$w_n = \frac{p_n}{\rho_n c^2} \ . \tag{1.6}$$

The density Ω_n is defined in terms of the density relative to the critical density ρ_c

$$\rho_c = \frac{3H^2}{8\pi G} \ , \tag{1.7}$$

so that Ω_n is then given by

$$\Omega_n = \frac{\rho_n}{\rho_c} \ . \tag{1.8}$$

The three most important density components are matter, radiation, and the cosmological constant. The cosmological constant is an allowed additional constant term in the Einstein field equations, and can be considered as an additional component of the energy-momentum tensor, with a constant density, Ω_Λ. Since the density must be independent of redshift, we can see from equation 1.5 that $w_\Lambda = -1$. We can then see from equation 1.6 that $w_\Lambda = -1$ implies the surprising result that the cosmological constant exerts a constant negative pressure, which becomes increasingly dominant as the density of the matter and radiation components decrease. Since it is the equation of state of the cosmological constant which we will most frequently consider, we will refer to $w_\Lambda = -1$ as simply w.

The equation of state for matter w_m is 0, so the density of matter Ω_m scales as the volume of the universe, as intuitively expected. As for radiation, the number density of particles scales as with matter, although the additional redshift of

the radiation (which scales linearly with the scale factor) causes the density of radiation Ω_r to scale proportionally to a^{-4}, so the equation of state w_r is 1/3. For a cosmological constant, the density Ω_Λ is independent of redshift, so the equation of state is given by $w_\Lambda = -1$. The matter density can be specified in terms of the density in cold dark matter, Ω_c, and the density in baryons, Ω_b. In later chapters, we also consider measuring the density of an ultra-light axion component of dark matter, Ω_a.

One of the most successful methods for measuring the values of the density parameters (and other cosmological parameters) has been through measurements of temperature fluctuations in the cosmic microwave background, most recently by the Wilkinson Microwave Anisotropy Probe (WMAP). The model of an isotropic and homogenous universe, with gravity described by general relativity, density dominated by the cosmological constant, and the majority of the matter consisting of cold dark matter has come to be known as the Λ Cold Dark Matter model, or ΛCDM. Throughout this work we will assume a flat, ΛCDM cosmology with parameters based on the seven year data release from WMAP, from Larson et al. [2011], with the matter density $\Omega_m h^2 = 0.1334$ and the baryon density $\Omega_b h^2 = 0.0226$.

The behaviour of $H(z)$, and, correspondingly, the values of the density parameters, has been measured via the luminosity distance to standard candles, most famously by Riess et al. [1998] and Perlmutter et al. [1999], with the detection of Ω_Λ. The expansion of the Universe has also been measured by the 'standard ruler' of the Baryon Acoustic Peak in the distribution of galaxies surveys at low redshift ($z \sim 0.5$), and in the CMB (although both galaxy surveys and the CMB provide further parameter constraints beyond a measurement of the angular diameter distance).

In the expanding FRW metric, the luminosity distance (the distance as measured with a standard candle) and angular diameter distance (the distance as measured with a standard ruler) are different, and can both be expressed in terms of the comoving distance. For an $H(z)$ with no redshift dependence, the comoving distance $D_C(z)$ could be written simply from Hubble's law:

$$D_C(z) = c\frac{z}{H_0} \, . \tag{1.9}$$

To include the redshift dependance, we integrate $H(z)$ from 0 to z:

$$D_C(z) = c \int_0^z \frac{dz'}{H(z')} \, . \tag{1.10}$$

Etherington [1933] showed that the comoving distance is related to the luminosity distance by

$$D_L(z) = (1+z) D_C(z) \, , \tag{1.11}$$

and the angular diameter distance by

$$D_A(z) = \frac{D_C(z)}{(1+z)} \, . \tag{1.12}$$

The comoving distance and angular diameter distance are plotted in Figure 1.1 tested against results from iCosmos [Trotta, 2008]. For completeness, the comoving volume enclosed to redshift z is also plotted, given by

$$V_C = \frac{4\pi}{3} D_C^3 \, . \tag{1.13}$$

1.2 Dark Energy

Although the discovery of dark energy is often associated with supernova light curve results from Riess et al. [1998] and Perlmutter et al. [1999], there were several other previous indications for a non-zero cosmological constant. Inflation, as proposed by Guth [1981] suggested a flat universe, with $\Omega = 1$, while Efstathiou et al. [1990] found tentative evidence in the APM (Automatic Plate Measuring) galaxy survey for a low Ω_m, which suggested that Ω_Λ may be as high as 0.8. In general, early measurements of $\Omega_m \approx 0.3$, combined with the assumption of flatness, set the scene for a dominant cosmological constant (for example, Kofman et al. [1993]), confirmed by the supernovae results of Riess et al. [1998] and Perlmutter et al. [1999]. With the advent of WMAP, the ΛCDM paradigm was largely confirmed by the first-year results [Spergel et al., 2003]. Contemporary results from the 2dFGRS and SDSS galaxy redshift surveys further compounded

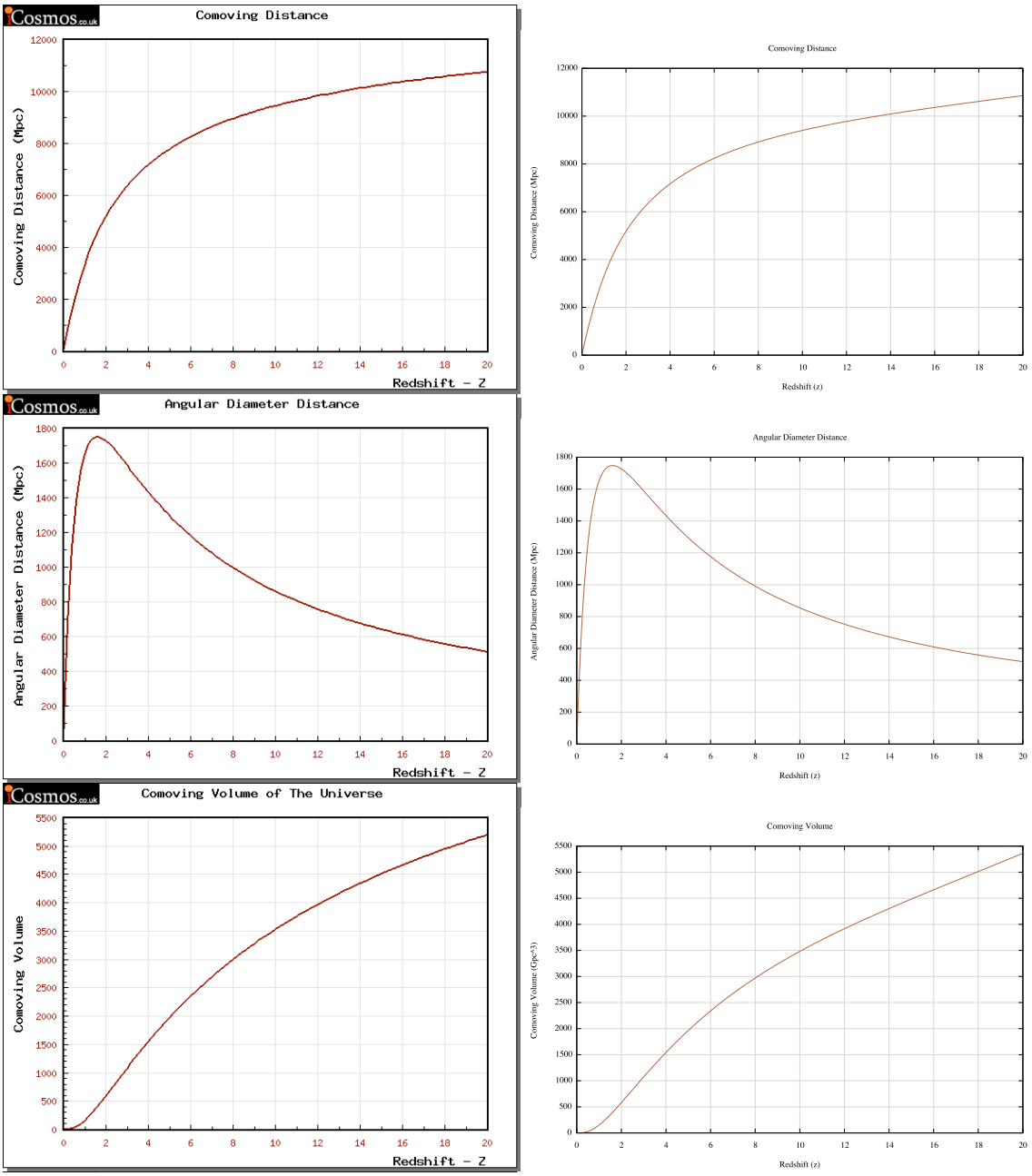

Figure 1.1: The comoving distance, angular diameter distance, and comoving volume, plotted on the right, verified against results from iCosmos [Trotta, 2008], plotted on the left.

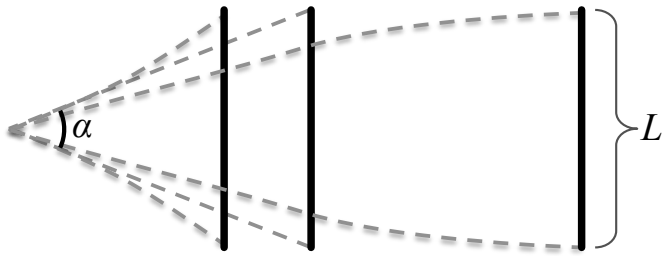

Figure 1.2: Illustrating the effect of curvature on determining distance. An object of fixed length L can subtend the same angle α at different distances, if the space has significant curvature. For a positively curved, closed space, an object of fixed length L will be further away than an object of the same length in flat space subtending the same angle. For a negatively curved space, the same object will subtend the same angle when it is closer to the observer than the same object in flat space.

the ΛCDM model (for example, Cole et al. [2005]; Peacock et al. [2001]; Percival et al. [2001, 2007a,b]).

Measurements of the primordial CMB cannot constrain dark energy alone, due to the degeneracy between distance and curvature. As illustrated in Figure 1.2, curvature causes an object of the same size and orientation to subtend the same angle while being at different distances. Although CMB measurements (of the last scattering surface) provide strong constraints on the parameters of the ΛCDM model, these measurements must be combined with low redshift measurements (such as supernovae) to break the degeneracy between curvature and dark energy. Sherwin et al. [2011] combined WMAP measurements with CMB lensing measurements from ACT (the Atacama Cosmology Telescope) and found evidence for dark energy from CMB measurements alone. Recently, Schrabback et al. [2010] found evidence for dark energy in weak lensing tomography measurements, and Reyes et al. [2010] found evidence for dark energy in a combined analysis of weak lensing and galaxy clustering.

If dark energy is genuinely due to a cosmological constant, the equation of state is exactly $w = -1$. Departures from behaviour as a cosmological constant can be parametrised with a variable equation of state $w(z)$. The most widely

used parametrisation was proposed by Linder & Huterer [2005], as

$$w(z) = w_0 + w_a(1+z) \ , \tag{1.14}$$

with $w_0 = -1$ and $w_a = 0$ corresponding to a cosmological constant. Huterer & Turner [2001] proposed the 'pivot redshift' parametrisation w_p, which is the value of w at which measurements of w_0 and w_a are uncorrelated, and depends on the observable technique with which w is measured. Measuring w at the pivot redshift allows for the smallest uncertainty on the dark energy parameters.

The cosmological constant represents the simplest explanation for dark energy, and – so far – appears in agreement with cosmological observations. However, the value of $\Omega_\Lambda \approx 0.7$ presents a serious fine-tuning problem with predictions from quantum field theory, which disagree by around 120 orders of magnitude in the density of the cosmological constant. The strange nature of the cosmological constant dark energy has motivated an enormous number of theories beyond the ΛCDM model to explain the accelerated expansion (see Clifton et al. [2012] for a review).

1.3 The Growth Rate

Since any dark energy theory must at least reproduce the apparent accelerated expansion at the background level, it can be difficult to test theories with only measurements of the background expansion, such as supernovae or BAOs. However, measuring the effect of gravity on smaller scales presents, in principle, a promising method to discriminate between models, since an incorrect theory which can reproduce the overall expansion will not necessarily be able to reproduce small scale features. The background to the growth of anisotropies we consider in this section is based on reviews by Coles & Lucchin [1995] and Gong [2008].

We consider the growth of small over or under-densities in matter, δ, defined as

$$\delta = \frac{\rho - \overline{\rho}}{\overline{\rho}} \ , \tag{1.15}$$

where ρ is the density and $\overline{\rho}$ is the average density at which δ is considered.

In the linear regime (i.e., perturbations which are only a small deviation from average) we can consider the observed density perturbations as a superposition of δ_k (of wavelength λ), with amplitudes given by the power spectrum, $P(k)$. If a perturbation is sufficiently dense (compared to the wavelength of the mode), the mode will tend to collapse due to gravitational Jeans instability. The gravitational potential of the over-density Φ can be described by the Poisson equation, so that $\nabla^2\Phi = 4\pi G\rho$. However, in the case of an expanding universe, there is an additional effect on the growth rate due to the expansion of the background, so the growth is given by

$$\ddot{\delta} + 2H\dot{\delta} - 4\pi G_{\rm eff}\rho\delta = 0\,, \tag{1.16}$$

where the third term models the growth under gravity, and the second term models the competing effect due to the background expansion. It is useful to define f, the perturbation growth rate, in terms of the e-folding time of the scale factor, as

$$f \equiv \frac{d\ln\delta}{d\ln a}\,. \tag{1.17}$$

Substituting the definition for f from 1.17 into 1.16, we find

$$\frac{df}{d\ln a} + f^2 + \left(\frac{\dot{H}}{H^2} + 2\right) f = \frac{3}{2}\frac{G_{\rm eff}}{G}\Omega\,. \tag{1.18}$$

$G_{\rm eff}$ depends on the particular model of gravitation, and equals 1 for ΛCDM. As an example, $G_{\rm eff}$ for the modified gravity DGP Braneworld model of Dvali, Gabadadze, & Porrati [2000] is given in

$$\frac{G_{\rm eff}}{G} = \frac{2(1+2\Omega^2)}{3(1+\Omega^2)}\,. \tag{1.19}$$

In general, f can only be solved numerically, although an approximate solution is given by

$$f = \Omega_m^{\gamma}\,. \tag{1.20}$$

The exponent γ can be set to trace out the growth history for a wide variety of cosmological models. For ΛCDM, $\gamma \approx 0.55$, whereas for DGP, $\gamma \approx 0.69$. The growth rate for several different cosmologies, with current measurements from

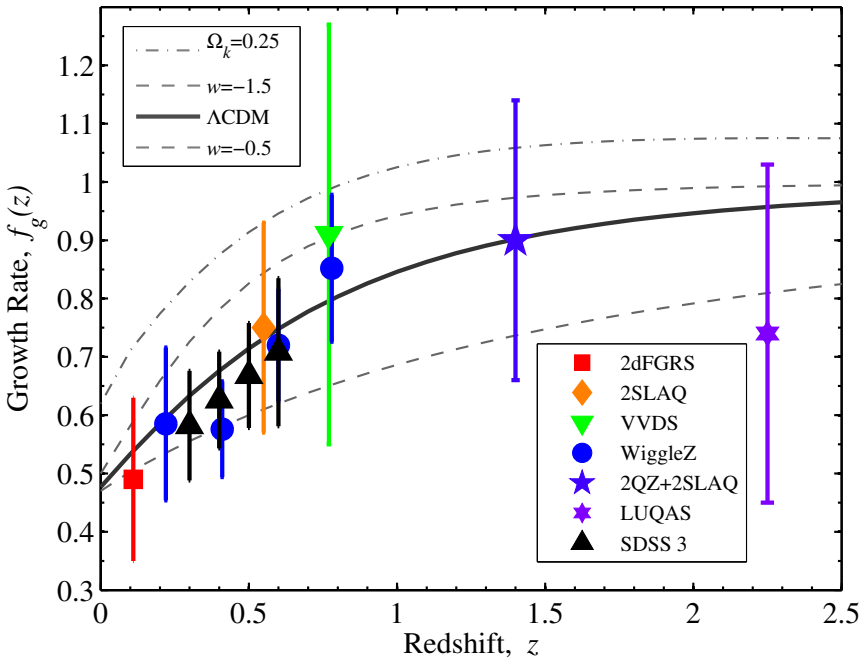

Figure 1.3: A plot of the growth rate for different parameters, with current measurements from 2dFGRS from Peacock et al. [2001], 2SLAQ from Ross et al. [2007], VVDS from Guzzo et al. [2008], WiggleZ Blake et al. [2010], 2QZ+2SLAQ da Ângela et al. [2008], LUQAS Viel et al. [2004] and SDSS Reid et al. [2012].

Redshift Space Distortions, is plotted in Figure 1.3.

1.4 The Power Spectrum & the Two-Point Correlation Function

A key concept that we will consider in this thesis is the power spectrum $P(k)$ of the density fluctuations, δ_k, and the real-space equivalent, the two-point correlation function, $\xi(r)$. The power spectrum is such a crucial concept because it relates the underlying theory and parameters to observables we can measure. The two-point correlation function $\xi(r)$ is defined as

$$\xi(\vec{r}) \equiv \langle \delta(\vec{x})\delta(\vec{x}+\vec{r}) \rangle \ . \tag{1.21}$$

The power spectrum is defined as

$$P(k) \equiv \left\langle |\delta_k|^2 \right\rangle \ . \tag{1.22}$$

$P(k)$ is related to $\xi(r)$ by the Fourier transform

$$P(k) = \frac{1}{2\pi^2} \int_0^\infty dr \xi(r) \frac{\sin kr}{kr} \ . \tag{1.23}$$

We next consider how the growth rate, angular diameter distance, and Hubble parameter can be measured with the power spectrum in galaxy redshift surveys. All methods rely on the two-point correlation function, $\xi(r)$, and the power spectrum, $P(k)$. For a galaxy redshift survey, $\xi(r)$ can be calculated, starting with an arbitrary first galaxy, and then counting the number of galaxies over a range of distances. This process is then repeated for all the galaxies in the survey to find the 'Data-Data' term of the correlation function, DD. The process must then be repeated for a set of random points with the same average density as the real sample, to find the 'Random-Random' term, RR. The simplest estimate of the correlation function is then given by

$$\xi(r) = \frac{DD}{RR} - 1 \ . \tag{1.24}$$

Landy & Szalay [1993] proposed an improved estimator, given by

$$\xi(r) = \frac{DD - 2DR + RR}{RR} \ . \tag{1.25}$$

Although the two point correlation function is defined as a function of distance, we will frequently consider the distance in terms of distance parallel and perpendicular to the line of sight, $\xi(r_{||}, r_\perp)$. Similarly, we can consider the power spectrum in terms of parallel and perpendicular k modes, $P(k_\perp, k_{||})$. This two dimensional power spectrum is often written as $P(k, \mu)$, where $\mu = \cos(k_\perp / k_{||})$ and $k = \sqrt{k_\perp^2 + k_{||}^2}$.

A key assumption of our cosmological model is that in real space $\xi(r)$ will be spherically symmetric. However, the measured position of the galaxies is given by the coordinates RA, Dec, and redshift, which can be converted to Cartesian

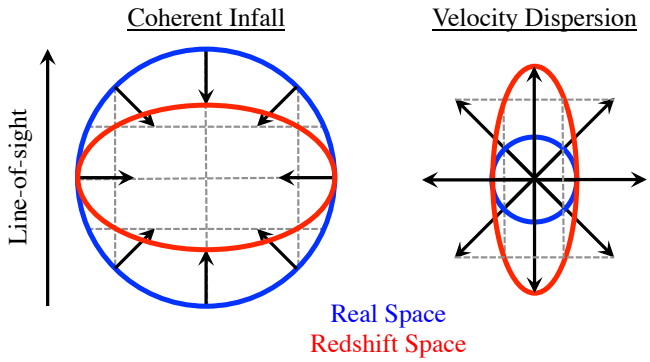

Figure 1.4: The two main redshift space distortion effects. On the left the effect of coherent infall (also known as the Kaiser effect) is illustrated, which causes over-dense regions to appear compressed along the line of sight (and under-dense regions to appear elongated along the line of sight). On the right, the effect of velocity dispersion is illustrated (also known as the Fingers of God effect), which causes an elongation along the line of sight.

coordinates X, Y, and Z. In converting redshift to distance, we have assumed Hubble's law, in the absence of distortion due to peculiar velocities. Peculiar velocities can often be comparable to, or larger than, the apparent velocities due to the Hubble flow, which introduce Redshift Space Distortions (RSD) along the line of sight. There are two main effects to consider, illustrated in Figure 1.4. The first effect is coherent infall into overdensities, which causes overdense regions to appear compressed along the line of sight, and underdense regions to appear elongated along the line of sight. Kaiser [1987] showed that this effect can be modelled as

$$P_{\text{galaxy}}(k,\mu) = b^2\left(1+\frac{f}{b}\mu^2\right)^2 \times P_{\text{matter}}(k) \tag{1.26}$$

where f is the growth rate, and b is the linear galaxy bias, defined as

$$\delta_{\text{galaxy}} = b\delta_{\text{matter}}\,. \tag{1.27}$$

The effect of bias is illustrated for a 1-D power spectrum in Figure 1.5, against the SDSS Large Red Galaxy power spectrum [Tegmark et al., 2006].

Thus by measuring the redshift space distortion compression in the two dimensional power spectrum $P(k,\mu)$, it is possible to measure the growth rate via the

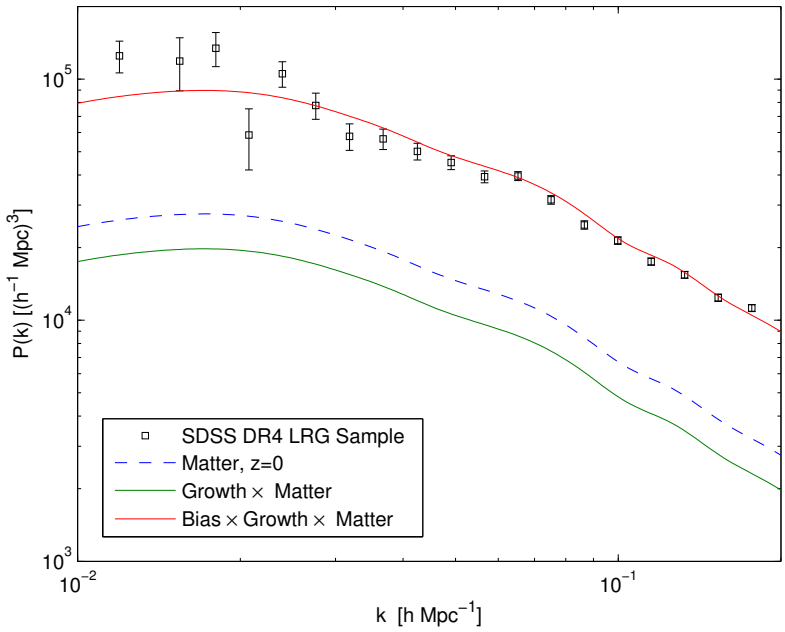

Figure 1.5: The matter power spectrum generated with CAMB [Lewis et al., 2000] with HALOFIT [Smith et al., 2003] to model non linearities at small scales, to match the SDSS LRG Sample from Tegmark et al. [2006] at $z = 0.3$ and a bias of 2.13. The error bars are plotted at the 1 σ level. We start with the matter power spectrum at $z = 0$ (blue dashed line) then divide by the growth rate from $z = 0.3$ to $z = 0$ to find the matter power spectrum at $z = 0.3$ (the green solid line). We then multiply the matter power spectrum at $z = 0.3$ by the linear galaxy bias (squared) to find the biased galaxy power spectrum (the solid red line).

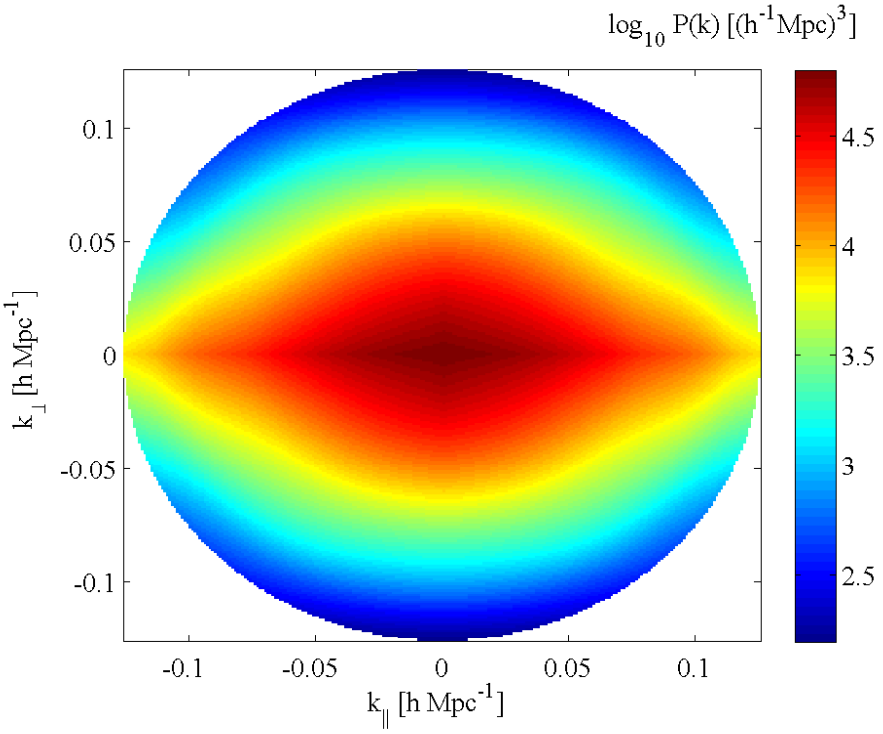

Figure 1.6: The two dimensional redshift space power spectrum at $z = 0.5$. Only one quadrant of the plot is unique – the other sections have been mirrored to illustrate the symmetry of the redshift space distortion.

$\frac{f}{b}$ term in the power spectrum. The ratio of $\frac{f}{b}$ is known as the RSD compression parameter, β.

On smaller scales ($\sim$5 h^{-1}Mpc) where galaxies are found within virialized clusters, the peculiar velocity due to velocity dispersion causes clusters of galaxies to appear elongated along the line of sight, also illustrated in Figure 1.4. In a similar manner to the compression parameter, this effect can be modelled with an additional factor as

$$P_{\text{galaxy}}(k,\mu) = b^2 \times \left(\frac{1}{1+(k\mu\sigma_v)^2/2}\right) \times \left(1+\beta\mu^2\right)^2 \times P_{\text{matter}}(k) \qquad (1.28)$$

where σ_v is the velocity dispersion parameter, typically around 350 km s^{-1}.

In this thesis, we consider measuring the power spectrum with galaxy surveys,

and constraints that can be placed on underlying cosmological parameters with such measurements. We consider redshift surveys and peculiar velocity surveys. The outline for the rest of the thesis is illustrated in Figure 1.7.

In chapter two we review peculiar velocity surveys, and present the likelihood approach we use to measure the power spectrum from the COMPOSITE peculiar velocity catalogue. In chapter three we present results for measurements of the power spectrum with peculiar velocities. Chapters four and five can be considered in parallel to chapters two and three, and concern Fisher forecasts for future galaxy redshift surveys. Chapter four introduces Fisher matrix techniques, reviews the background to galaxy redshift surveys, and presents forecasts for the standard ΛCDM model, with a focus on survey design and optimisation of measurements. In chapter five, we extend the forecasts to include extended cosmological parameters, and present detailed forecasts for neutrino and ultra-light axion dark matter, and preliminary forecasts for testing General Relativity with a parametrised modified gravity approach. Chapter 6 combines both branches of the thesis to compare forecasts for future redshift and peculiar velocity surveys.

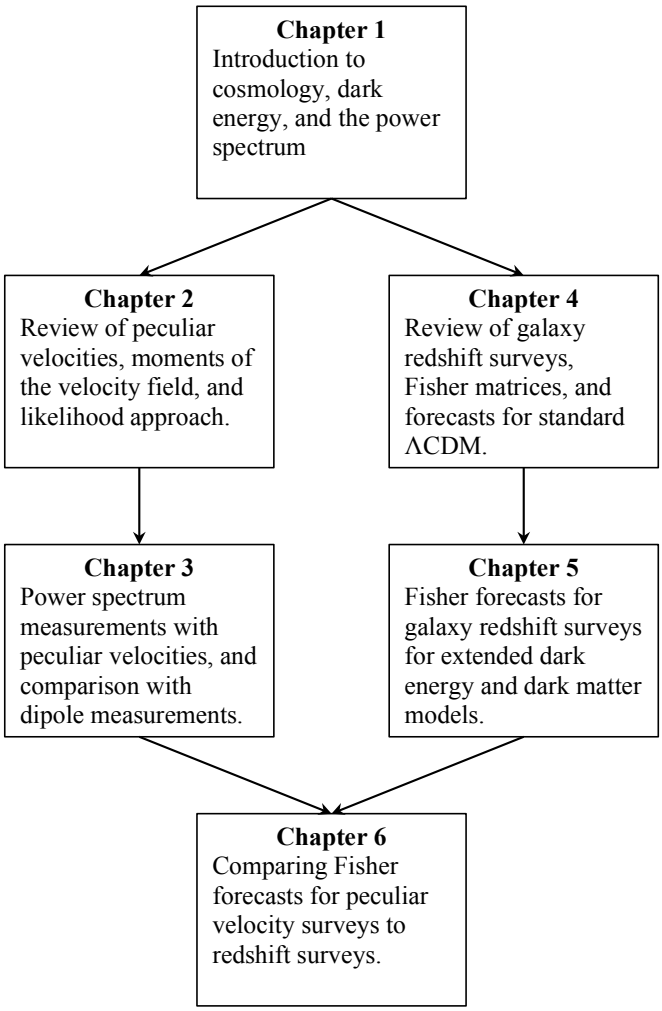

Figure 1.7: A schematic outline of the chapters in the this thesis. Chapter 1 contains introductory material which is common to both branches of the thesis.

Chapter 2

Peculiar Velocity Surveys & the Power Spectrum Likelihood Framework

2.1 Introduction & Background

The peculiar velocities of galaxies are a unique cosmological probe, which directly traces the underlying dark matter distribution (independent of galaxy bias) and is also sensitive to scales much larger than the size of the survey.

We can measure the peculiar velocity via the effect it has on the redshift of the galaxy. The redshift z of a galaxy is given by a contribution from the Hubble flow, $H_0 r$, and the line of sight component of the peculiar velocity S:

$$cz = H_0 r + S \tag{2.1}$$

where, for a galaxy labelled m, at position $\mathbf{r}_m$, we have the line of sight peculiar velocity, S_m given by

$$S_m = \hat{\mathbf{r}}_m \cdot \mathbf{v}(\mathbf{r}_m) \tag{2.2}$$

where $\hat{\mathbf{r}}_m$ is a unit vector in the direction of galaxy m. To measure S we thus need to combine the redshift of the galaxy with an *independent* measure of the distance r. In principle, we can calculate the peculiar velocity of any galaxy for

which we have the luminosity distance, measured using distance indicators such as supernovae, Brightest Cluster Galaxies [Postman & Lauer, 1995], Tully-Fisher [Tully & Fisher, 1977] or Fundamental-Plane [Dressler et al., 1987] measurements.

The Brightest Cluster Galaxies method assumes that the brightest elliptical galaxy within any cluster of galaxies always has the same intrinsic luminosity. Lauer & Postman [1994] found a bulk flow of 689±178 km s^{-s} in 119 Abell clusters with the Brightest Cluster Galaxy method. However, Hudson & Ebeling [1997] found slower bulk flows which were inconsistent with the Lauer & Postman [1994] bulk flow, and found that the luminosity distance indicators depended significantly on calibration with X-ray luminosity.

The Tully-Fisher method [Tully & Fisher, 1977] can be used to estimate the intrinsic luminosity in spiral galaxies. The method is based on an observed correlation between line width due to rotation (which can be measured directly), and intrinsic luminosity. The Fundamental-Plane is an analogous method for elliptical galaxies, which reduces the scatter of the Faber-Jackson method it is based on. Faber & Jackson [1976] noted a correlation between luminosity and the velocity dispersion of stars in elliptical galaxies, which can be used a distance indicator, although with considerably large scatter. [Dressler et al., 1987] noted that luminosity and velocity dispersion were also correlated with the effective radius of the galaxy. Taken together, these three parameters form the 'Fundamental Plane' for elliptical galaxies. By measuring the radius and velocity dispersion, the intrinsic luminosity can be inferred with a smaller uncertainty than with the Faber-Jackson method alone. The Tully-Fisher and Fundamental plane methods both assume the mass to light ratio of the galaxies, although consistency with Cepheid distance indicators (where both can be simultaneously measured) suggests that both methods are sufficiently robust. Individual uncertainties on luminosity distances are typically rather large (5% for supernovae, and around 10 to 20% for Tully-Fisher and Fundamental-Plane), which propagates to a large uncertainty in the peculiar velocity.

Before the detection of temperature fluctuations in the CMB (e.g. Smoot et al. [1992]), peculiar velocity measurements presented (in principle) one of the most promising methods to measure Ω_m. However, much previous work was troubled by systematic issues with peculiar velocity data, and difficulties with

analysis methods, which tended to suggest high bulk flows, and favour $\Omega_m \sim 1$, in particular the Mark III peculiar velocity catalogue, and the POTENT velocity field reconstruction method. For example, Dekel & Rees [1994] appeared to rule out $\Omega_m \sim 0.3$ at the 2.4 σ level, and Nusser & Dekel [1993] rule out $\Omega_m \sim 0.3$ at the 4 to 6 σ level. Since then, with the rise of other cosmological observables, cosmology with peculiar velocities has become less popular. However, with recent improvements in peculiar velocity data, and more robust analysis methods, the field is attracting attention again.

Recent interest in peculiar velocities has been driven by the high dipole moment of our local velocity field, which can appear to be in some tension with the ΛCDM model. The ΛCDM model indicates that we should expect a peculiar velocity dipole of magnitude around 100 km s^{-1}, although many independent peculiar velocity surveys show evidence for a bulk flow at redshift zero of around 416±78 km s^{-1} in the direction $l = 280$ $b = 10$ degrees [Feldman et al., 2010; Hudson et al., 2004; Ma et al., 2010; Watkins et al., 2009]. However, Nusser & Davis [2011] find evidence for a flow more commensurate with ΛCDM of around 257 ± 44 km s^{-1} (in a similar direction as the other bulk flow results).

In more tension with ΛCDM are significantly higher bulk flows at redshift ∼0.25, which curiously appear to be in the same direction as the low redshift bulk flows. Abate & Feldman [2012] found evidence for an extremely high bulk flow of 4450^{+1350}_{-1100} km s^{-1} at redshift ∼0.3, in a similar direction to other bulk flows. Kashlinsky et al. [2010] find a bulk flow of around 1000±300 km s^{-1} extending to $z \simeq 0.2$ from kinematic Sunyaev-Zel'dovich measurements. If substantiated, these bulk flows would indicate a non convergence of the peculiar velocity dipole, and present a serious challenge to the assumptions of isotropy and homogeneity. However, these bulk flow measurements are far from as robust as the directly measured peculiar velocity measurements we consider here; Abate & Feldman [2012] note that their result may be entirely due to systematic effects. In this work, we will only consider the direct peculiar velocity measurements at low redshift.

In addition to the high dipole moment, there also appears to be a low shear of the velocity field [Feldman et al., 2010; Jaffe & Kaiser, 1995], which indicates that the density contrast responsible for the velocity dipole is on extremely large

scales. At the depths of the peculiar velocity surveys (up to 100 h^{-1}Mpc), this suggests an excess density contrast on scales $\sim 1\ h^{-1}$Gpc. The volume of space probed by spectroscopic galaxy redshift surveys (e.g. Cole et al. 2005; Reid et al. 2010 and Blake et al. 2010) is currently too small to robustly constrain clustering on these scales, although Thomas et al. [2010] found some evidence for excess large scale power in the MegaZ photometric redshift survey, although Ross et al. [2011] suggest the excess may be due to systematic errors. Measurements of the CMB can probe anisotropies on these large scales [Hlozek et al., 2012; Larson et al., 2011], although to compare to results at low redshift, the growth of these anisotropies must be assumed, which depends on the cosmological model.

There are many possible explanations for the high dipole moment, ranging from systematic effects to more exotic explanations invoking extended cosmology or modified gravity. Hudson et al. [2004] considered systematic effects in the SMAC peculiar velocity survey, such as a dipole variation in the velocity dispersion, galactic extinction, and calibration across different observations. They found that systematic effects could account for at most half of the high dipole moment of the SMAC survey, leaving a dipole moment which is still at least three times higher than the ΛCDM expectation. There are many theoretical possibilities to extend the ΛCDM model to produce a large scale excess of power and a peculiar velocity dipole, such as modifications to gravity, [Ayaita et al., 2009; Khoury & Wyman, 2009], dark energy clustering [Potter & Chongchitnan, 2011], vorticity, [Palle, 2010] or 'tilted' universes [Kashlinsky et al., 2010; Ma et al., 2010; Mersini-Houghton & Holman, 2009]. In this work we do not address any theoretical explanation in particular, but by using the peculiar velocity data to constrain the power spectrum in model independent band-powers we aim to provide results which will be useful to constrain a range of explanations for the high dipole.

Jaffe & Kaiser [1995], Kolatt et al. [1996], Zaroubi et al. [1997], Kolatt & Dekel [1997], Zaroubi et al. [2001] and Silberman et al. [2001] have used peculiar velocity surveys to infer the matter power spectrum directly at $z = 0$. Recently, Abate & Erdoğdu [2009] applied a similar formalism to constrain the modified gravity parameter γ, where the perturbation growth rate f_g can be approximated as $\Omega_m(z)^\gamma$. Ma et al. [2010] also used a similar formalism to fit for parameters of

the dipole moment and velocity dispersion parameter. In both cases, a fiducial ΛCDM power spectrum was assumed, and additional parameters of interest were allowed to vary. The key difference between those papers and this work is that here we treat the underlying power spectrum as a set of free parameters, as opposed to fitting extra parameters for additional effects beyond a fixed power spectrum. In this way, we obtain new constraints on the power spectrum which are independent of the fiducial cosmology.

2.2 Method

In this work we consider two distinct methods to relate peculiar velocity measurements to large scale structure: A maximum likelihood based approach to analyse a full peculiar velocity catalogue (the 'catalogue' method), and an alternative approach studying minimum-variance moments of the velocity field (the 'moments' method).

In the linear regime, the peculiar velocity field $\mathbf{v}(\mathbf{r})$ can be fully described as directly proportional to the gradient of the matter density perturbation field $\delta(\mathbf{r})$. The relationship is usually written in integral form, as

$$\mathbf{v}(\mathbf{r}) = \frac{f_g H_0}{4\pi} \int d^3\mathbf{r}' \delta(\mathbf{r}') \frac{(\mathbf{r}' - \mathbf{r})}{|\mathbf{r}' - \mathbf{r}|^3} \,, \tag{2.3}$$

where f_g is the growth rate of the density contrast, $\partial \ln \delta / \partial \ln a$, and a is the scale factor [Peebles, 1993].

2.2.1 Maximum Likelihood Catalogue Method

We now consider how to relate a catalogue of peculiar velocity measurements S_m to large scale structure, following the method as presented in Jaffe & Kaiser [1995]. The method is based on a likelihood framework, where the likelihood $\mathcal{L}$ is given by

$$\mathcal{L} = \frac{1}{2\pi^{N/2} \left|R_{mn}\right|^{1/2}} \exp\left(-\frac{1}{2} S_m R^{-1}_{mn} S_n\right) \tag{2.4}$$

where R_{mn} is the covariance matrix for the peculiar velocity measurements, for a catalogue of N galaxies. The covariance matrix is split into two components, a 'velocity' and an 'error' term:

$$R_{mn} = R^{(v)}_{mn} + R^{(e)}_{mn} \ . \tag{2.5}$$

$R^{(v)}_{mn}$ models the coherent large scale structure, and $R^{(e)}_{mn}$ is a noise component to account for nonlinear velocity dispersion σ_* (seen as the Fingers-of-God effect in redshift surveys) , and uncertainty in each peculiar velocity measurement σ_m. If we assume that the measurement errors are uncorrelated, $R^{(e)}_{mn}$ simply contributes these uncertainties to the diagonal of the covariance matrix, and is given by

$$R^{(e)}_{mn} = (\sigma^2_m + \sigma^2_*)\delta_{mn} \tag{2.6}$$

where δ_{mn} is the Kronecker delta. The large scale structure of interest enters via the 'velocity' component of the covariance matrix, and is given by

$$R^{(v)}_{mn}(k) = \int \frac{4\pi k^2 dk}{(2\pi)^3} P_v(k) f_{mn}(k) \tag{2.7}$$

where $P_v(k)$ is the velocity power spectrum, which is related to the matter power spectrum by

$$P_v(k) = \left(\frac{H_0 a}{k}\right)^2 f_g^2 P(k) \ . \tag{2.8}$$

Here a is the scale factor. The window function $f_{mn}(k)$ is given by

$$f_{mn}(k) = \hat{r}_{m,i}\hat{r}_{n,j} \int \frac{d^2\hat{k}}{4\pi} \hat{k}_i \hat{k}_j e^{ik\hat{\mathbf{k}}\cdot(\mathbf{r_m}-\mathbf{r_n})} \tag{2.9}$$

where r_m is the position of galaxy m, and $\hat{r}_m$ is a unit vector in the direction of galaxy m. The window function can be calculated analytically in terms of trigonometric functions, and depends on the positions of the galaxies in the catalogue. A derivation of f_{mn} is presented in Ma et al. [2010]. The general approach we take is to map out the likelihood in terms of parameters of the power spectrum. We next consider an analogous method to analyse moments of the velocity field, before considering parametrisation of the power spectrum any further, since

the parametrisation is common to both methods.

2.2.2 Minimum Variance Moments Method

In this work we directly compare results between the maximum likelihood catalogue method to an alternative method studying moments of the velocity field calculated by Watkins et al. [2009] and Feldman et al. [2010]. We can consider the velocity field as a Taylor expansion, given by:

$$v_i(\mathbf{r}) = U_i + U_{ij} r_j + U_{ijk} r_j r_k + \dots \tag{2.10}$$

where U_i is the dipole moment of the velocity field (often called the 'bulk flow'), and provides most information about the largest scale fluctuations. U_{ij} is the shear of the velocity field, sensitive to intermediate scales. U_{ijk} is the octupole moment, and is sensitive to scales less than the size of the survey. The relative sensitivity of each moment is shown in Figure 2.1. Since we can only measure the line of sight component of each peculiar velocity, each individual measurement must be weighted according to the component of the moment it is sensitive to. Watkins et al. [2009] and Feldman et al. [2010] developed new 'minimum variance' weights to estimate the velocity of the *volume* traced by the galaxies in the survey. These weights are designed to minimise the effects of small scale motions, to provide a better estimate of the large scale velocities. We do not reproduce the derivations of the weights here; the method is presented in Watkins et al. [2009] for the dipole and extended in Feldman et al. [2010] for the shear and octupole.

With this method, the data consists of the three components of the dipole vector, six independent components of the shear, and ten independent components of the octupole. We take a similar approach as with the catalogue method, splitting the covariance matrix into 'velocity' and 'error' terms. The 'velocity' term is now given by

$$R_{pq}^{(v)} = \frac{f_g^2}{2\pi^2} \int dk P(k) \mathcal{W}_{pq}^2(k) \tag{2.11}$$

where p and q index the 19 independent moments. The window function $\mathcal{W}_{pq}^2(k)$

is given by

$$\mathcal{W}^2_{pq}(k) = \sum_{n,m} w_{p,n} w_{q,m} f_{mn}(k) \,, \tag{2.12}$$

where $f_{mn}(k)$ is the window function from equation 2.9, and $w_{p,n}$ is the minimum variance weight for the contribution of galaxy n to moment p. $\mathcal{W}^2_{pq}(k)$ is sensitive to different scales for the dipole, shear and octupole, as plotted in Figure 2.1. We then construct a likelihood in exactly the same manner as the catalogue method, in terms of parameters of a power spectrum, which we now consider.

2.2.3 Power Spectrum Parametrisation

Ultimately, we wish to constrain parameters of the underlying matter power spectrum. There are many choices for ways to parametrise the power spectrum. A popular choice in many earlier works was the power spectrum shape parameter Γ, the matter density Ω_m and the power spectrum normalization at 8 h^{-1}Mpc, σ_8 [Jaffe & Kaiser, 1995; Kolatt & Dekel, 1995]. Silberman et al. [2001] opted for a band-power parametrisation, which is the approach we take here, in terms of band-powers, P_α, so the power spectrum is given by

$$P(k) = \begin{cases} P_\alpha & k_\alpha < k < k_{\alpha+1} \\ 0 & \text{otherwise.} \end{cases} \tag{2.13}$$

The velocity covariance matrix is then

$$R^{(v)}_{mn}(k) \approx \frac{(H)^2}{2\pi^2} f_g^2 \sum_\alpha P_\alpha \mathcal{K}_\alpha \tag{2.14}$$

where $\mathcal{K}$ is given by

$$\mathcal{K}_\alpha = \int_{k_\alpha}^{k_{\alpha+1}} dk f_{mn}(k) \tag{2.15}$$

This parametrisation is directly sensitive to the combination of $f_g^2 P_\alpha$. To directly constrain $P(k)$, we must either assume a fiducial growth rate, or marginalise over other measurements of the growth rate. For generality, we choose to treat the combination of $f_g^2 P_\alpha$ as a parameter.

We find that in the widest, single band parametrisation, flat band-powers can

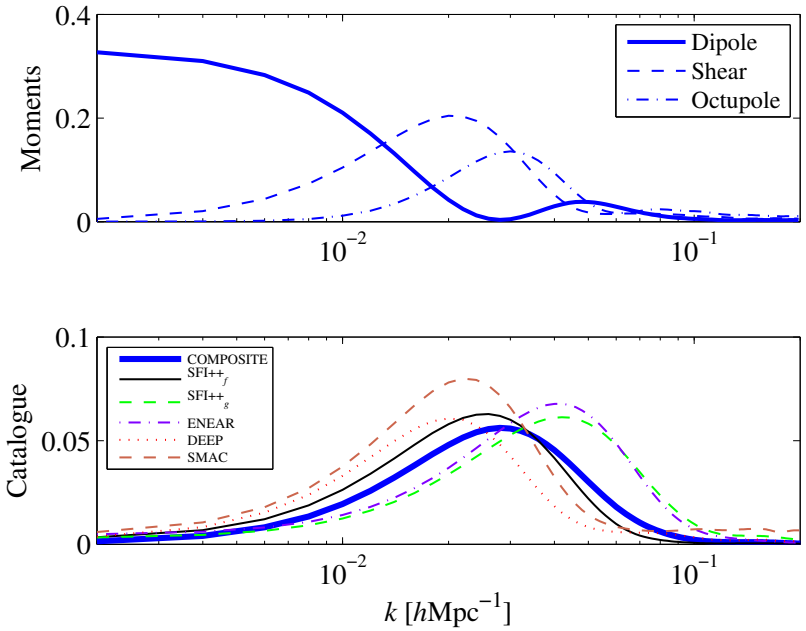

Figure 2.1: Comparing sensitivity to different scales for the moments and catalogue methods. For the moments panel, we plot the average of the diagonal of the covariance matrix for the dipole, shear and octupole terms, for COMPOSITE [Feldman et al., 2010]. The catalogues are described in the next section. Since the moments are designed to be orthogonal, the diagonal of the covariance matrix gives an indication of the scales at which the moments are most sensitive. For the catalogue panel, the diagonal of the covariance matrix is 1/3, so we plot the sum of the entire covariance matrix, normalised by the square of the number of galaxies in each catalogue, which illustrates the scales at which the window function is sensitive. The sub-catalogues which span the greatest distance, DEEP [Watkins et al., 2009] and SMAC [Hudson et al., 2004], are most sensitive to largest scales, while the shallowest catalogues, SFI++$_g$ [Masters et al., 2006; Springob et al., 2009a,b] and ENEAR [da Costa et al., 2000], are most sensitive to smaller scales.

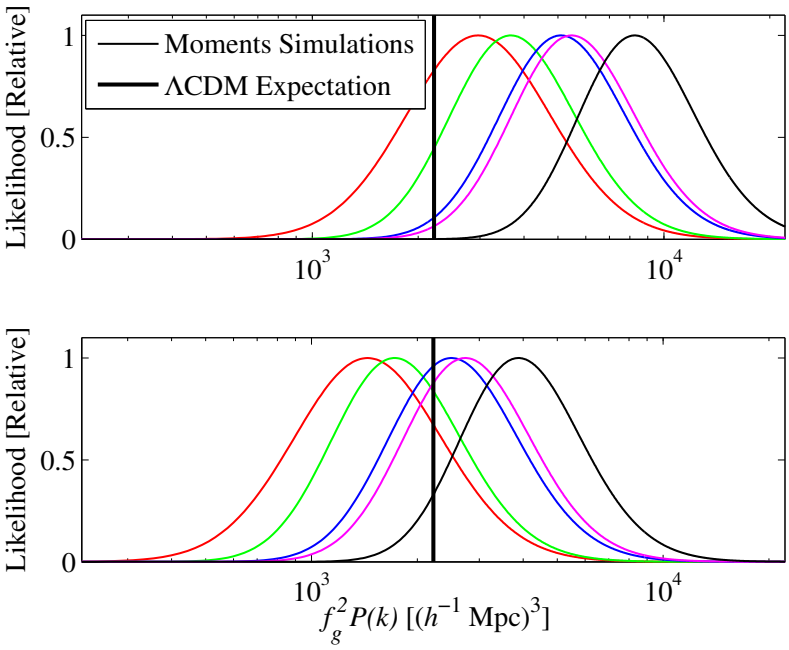

Figure 2.2: The effect of band shape – the results are for five different realisations of a ΛCDM simulation, each consisting of dipole, shear and octupole moments. In the upper panel, when using the constant amplitude of a single flat band-power to parametrise the power spectrum, we find a systematic excess compared to the average ΛCDM power spectrum in the same k range. However, when we use the amplitude of the ΛCDM power spectrum, A_α as a parameter, we find no systematic deviation from the $A_\alpha = 1$ expectation. The results with A_α as a parameter are then multiplied by the mean of the power spectrum in each band, P_α .

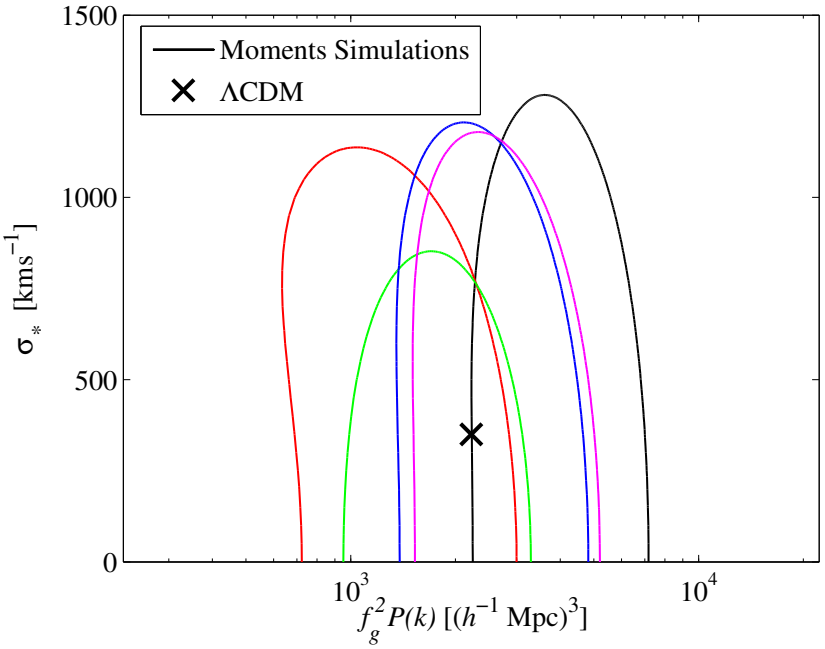

Figure 2.3: One standard deviation contours for one power spectrum band and the velocity dispersion σ_*, for the same moments plotted in Figure 2.2. The contours are fairly insensitive to the choice of σ_*. Since compressing the velocity field into moments is insensitive to small scale effects, these contours are consistent with $\sigma_* = 0$. The 1d likelihood distributions are for a fixed σ_* of 200 kms^{-1}

introduce an apparent artificial shift towards an excess of power, shown in the upper panel of Figure 2.2. We find that when we factor in a fiducial ΛCDM power spectrum into the window function, $P_{\rm fid}(k)$, and allow a constant amplitude of this power spectrum, A_α, to vary, we obtain an amplitude which is consistent with ΛCDM. The kernel in this case is

$$\mathcal{K}_\alpha = \int_{k_\alpha}^{k_{\alpha+1}} dk f_{mn}(k) P_{\rm fid}(k) \tag{2.16}$$

so our velocity covariance matrix is now

$$R_{mn}^{(v)} \approx \frac{(H)^2}{2\pi^2} f_g^2 \sum_\alpha A_\alpha \mathcal{K}_\alpha \tag{2.17}$$

where our parameter is now A_α, the amplitude of the fiducial power spectrum in each band. We thus expect $A_\alpha = 1$ in all bands for a ΛCDM velocity field. To more easily compare A_α to expectations, we multiply the results by the mean of the power spectrum in each band, $\langle P_\alpha \rangle$, given by

$$\langle P_\alpha \rangle = \frac{\int_{k_\alpha}^{k_{\alpha+1}} dk P_{\rm fid}(k)}{k_{\alpha+1} - k_\alpha} \, . \tag{2.18}$$

Although this parametrisation specifies the shape of the power spectrum within each band, we see in Section 3.2 in simulated catalogues that the method is fairly robust to the choice of fiducial power spectrum. We find that the catalogue method is sensitive to the velocity dispersion parameter, and thus treat it as a free parameter in the manner of Ma et al. [2010]. To directly compare between the catalogue and moments method, we also analyse the velocity moments with σ_* as a free parameter, although we find with results from velocity moments that marginalising over the velocity dispersion parameter has only a very small effect. We assume a fiducial value for the velocity dispersion of 350 km s^{-1}.

Chapter 3

Power Spectrum Measurements with the COMPOSITE Catalogue

3.1 Peculiar Velocity Data

We primarily study the COMPOSITE peculiar velocity catalogue, which consists of 4537 individual peculiar velocity measurements, and a characteristic depth of 33 h^{-1}Mpc, compiled by Feldman et al. [2010]. The COMPOSITE catalogue is composed of several sub-catalogues, which we also consider individually. The largest sub-catalogue is the SFI++ sample, which consists of 3456 Tully-Fisher measurements. We analyse the field galaxies and groups in the SFI++ sample separately, as SFI++$_f$ (2720 galaxies) and SFI++$_g$ (736 measurements) [Masters et al., 2006; Springob et al., 2009a,b]. We also study the combined DEEP catalogue, compiled by Watkins et al. [2009], which consists of 294 of the deepest peculiar velocity measurements and the ENEAR catalogue [da Costa et al., 2000]. The smallest catalogue we consider individually is the SMAC catalogue [Hudson et al., 2004], which is a sub-set of the DEEP catalogue.

We test our procedures on peculiar velocity catalogues generated from ΛCDM simulations. We analyse the set of 20 simulated Mark III catalogues[1] drawn from realisations of the Virgo simulation [Kolatt et al., 1996], consisting of 1300 entries

[1]downloaded from `http://www.mpa-garching.mpg.de/NumCos/CR/Download/index.html`

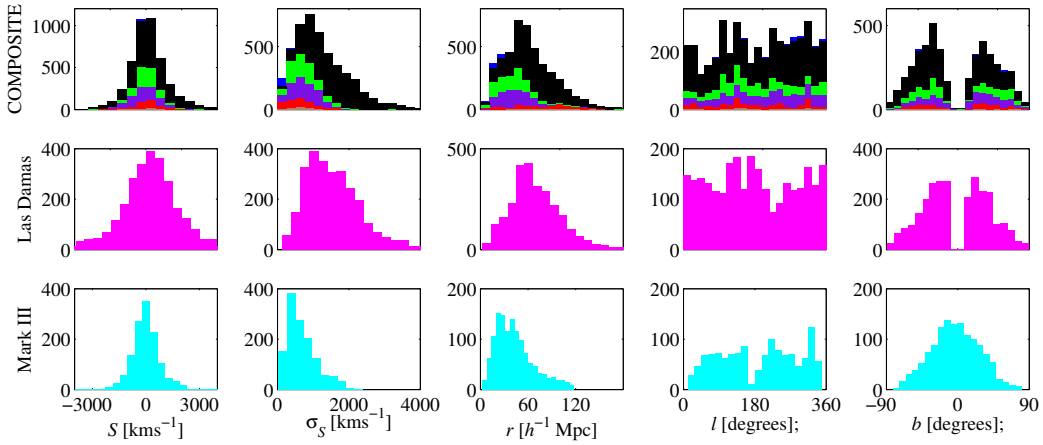

Figure 3.1: Histograms of the real surveys, and the Las Damas and Mark III simulated surveys, illustrating the distribution of line of sight peculiar velocities, S, uncertainty in S, σ_S, distance r, and coordinates l and b. The COMPOSITE survey is plotted as a stacked histogram and is comprised of the SFI++$_f$ (black), SFI++$_g$ (green), ENEAR (purple), DEEP (red), and SMAC (brown) surveys.

each (some of the catalogues consisted of slightly more than 1300 entries - these were trimmed to 1300 for consistency). We also study six simulated catalogues from the Las Damas simulation (McBride et al., in prep.), designed to resemble the SFI++$_f$ catalogue with 2720 entries. Histograms of the real and simulated surveys are shown in Figure 3.1.

We study the simulated data sets with both the catalogue and moments method. We analyse the real data with the catalogue method for the combined COMPOSITE set, and the five sub-catalogues. We find that the sub-catalogues are too small to reliably study the moments alone, so we present results here with the moments method only for the COMPOSITE catalogue.

3.2 Results

3.2.1 Simulated Data

We begin by testing our method on peculiar velocity catalogues generated from ΛCDM simulations. We start the analysis with the simplest parametrisation: one band-power. We choose a window function range of $k = 0.002$ to 0.196 h^{-1}Mpc,

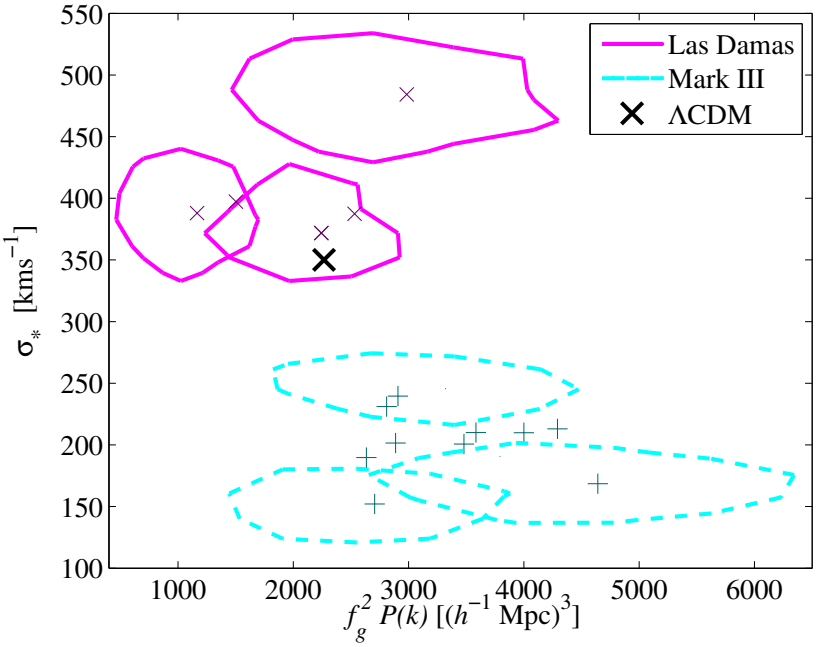

Figure 3.2: Constraints on the velocity dispersion parameter σ_* and one band-power, in the range $k = 0.002$ to $0.196\ h^{-1}$Mpc, for *simulated* peculiar velocity surveys from the Las Damas and Mark III simulations. The markers represent the peak of the likelihood for each catalogue. The contours are 1 standard deviation uncertainty about the peak likelihood, which we have only plotted for three catalogues for each simluation set, to prevent the plot from becoming overcrowded. Similarly, we only plot results for 10 of the Mark III catalogues. These uncertainty ranges are typical for the points plotted here.

and also include the velocity dispersion as a free parameter. Results are shown in Figure 3.2.

We find that for this band-power parametrisation, the velocity dispersion is uncorrelated with the power spectrum amplitude. The velocity dispersion is slightly higher than the ΛCDM expectation for the Las Damas mocks, although it is lower in the Mark III mocks. In both sets of mocks, we note a small systematic shift from the ΛCDM expectation. As this shift is in opposite directions for the Mark III and Las Damas mocks, it seems reasonable to conclude that this may be due to the many particularities of generating a mock catalogue from an underlying power spectrum, as opposed to a systematic shift introduced by our

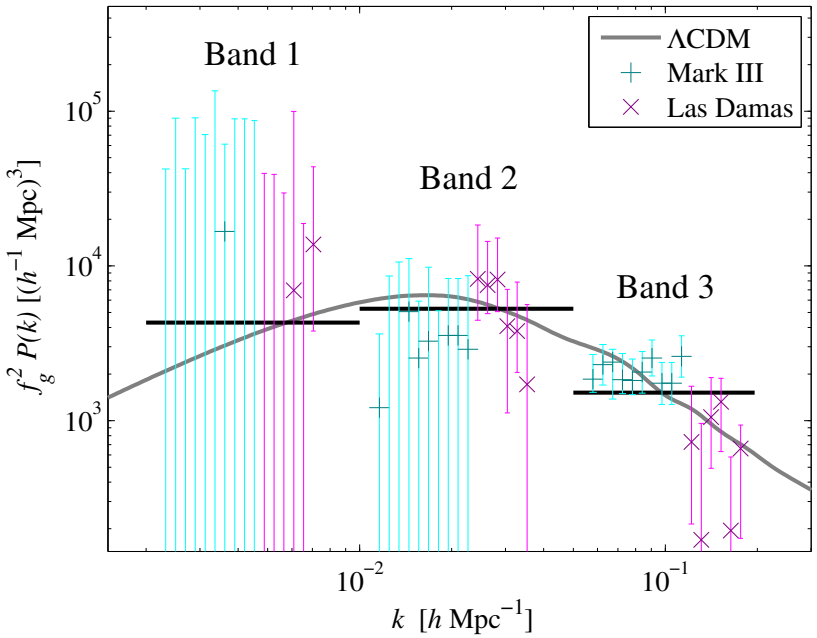

Figure 3.3: Results from the Mark III and Las Damas mocks in three band-powers. The velocity dispersion was varied as a free parameter, and marginalized over in these results. The grey curve is the ΛCDM power spectrum. The horizontal black lines span the k ranges of the band-powers, and indicate the average value of the power spectrum across this range. The results should be compared directly to these. The markers are the marginalized results for each band-power, for each of the Mark III and Las Damas simulated surveys. The k location within each band is arbitrary; each point should be fully considered equally at the centre of the band, spanning the full width.

method. In other words, the Mark III and Las Damas mocks taken together surround the ΛCDM expectation well. We next consider a parametrisation with three band-powers, spanning the same k range with bands evenly spaced in $\log k$. The results are shown in Figure 3.3.

We will refer to the bands from the largest scales to the smallest scales as bands 1 to 3. We find that the uncertainty in band 1 is larger in the simulated data with the catalogue method than the moments method (not plotted). The uncertainty in band 1 is particularly important for understanding the high dipole moment, and will be discussed further in Section 3.3. Both sets of catalogues are much more sensitive in band 3 than with the moments method; we thus decide

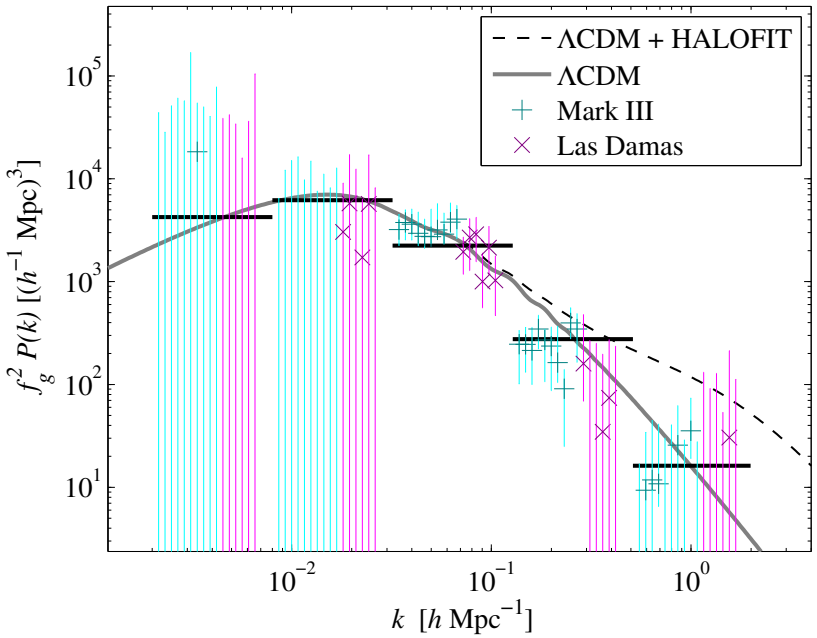

Figure 3.4: As Figure 3.3, but with two additional bands added at smaller scales. The smallest scale band is at scales for which nonlinear effects are significant. The data appears to favour the linear power spectrum, which may be due to the additional variance of the velocity dispersion parameter.

to extend that band-power parametrisation by adding two more bands (4 and 5) at smaller scales. Results are shown in Figure 3.4.

We find that band 5 is anti-correlated with the velocity dispersion parameter. This is not surprising, given the $\sim 5\ h^{-1}$Mpc scales spanned by this band. We see a difference at over 1σ from the nonlinear Halofit [Smith et al., 2003] corrections to the galaxy power spectra. We repeat the results in Figure 3.4 assuming a fiducial Halofit corrected power spectrum to factor into the window function. The results are shown in Figure 3.5. We see in the smallest two bands that the data still favour the linear power spectrum.

We consider the χ^2 statistic, given by

$$\chi^2 = \sum_\alpha \frac{\left(P_\alpha - \bar{P}_\alpha\right)^2}{\sigma^2_{P_\alpha}}\ , \tag{3.1}$$

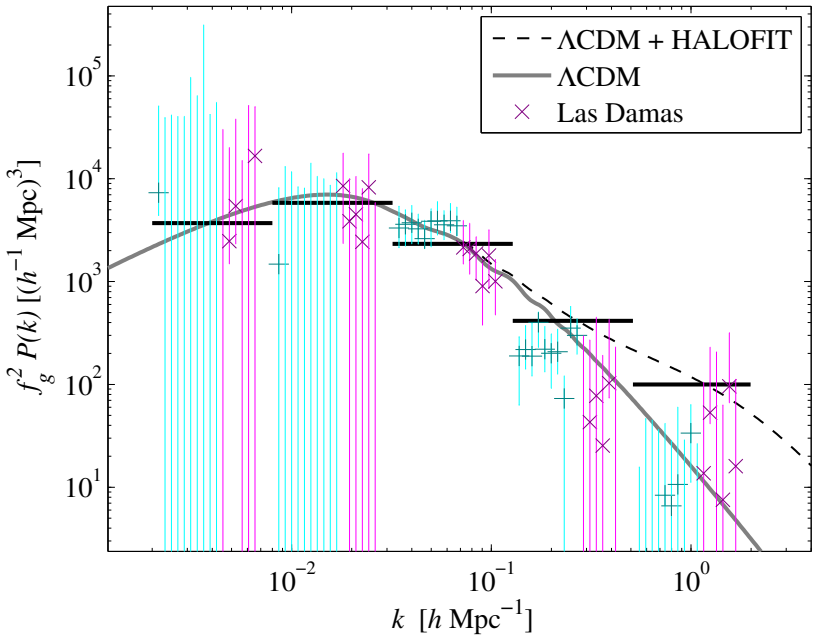

Figure 3.5: As Figure 3.4, but with a fiducial power spectrum corrected with Halofit. The black bars now represent the mean value of the Halofit fiducial power spectrum which was factored into the window function. The data still favour the linear power spectrum, indicating that the method is robust to the choice of fiducial power spectrum.

where P_α is the measured band-power in band α with uncertainty σ_{P_α}, and $\bar{P}_\alpha$ is the fiducial value of the band (which we do not estimate from the data). With the HALOFIT fiducial power spectrum, we find an average χ^2 of 13.8 for the simulated SFI++ catalogues, and an average $\chi^2 = 48.7$ for the simulated MIII catalogues. For the linear fiducial power spectrum, we find an average $\chi^2 = 6.3$ for the simulated SFI++ catalogues, and an average $\chi^2 = 4.5$ for the simulated MIII catalogues – an average $\chi^2 = 5.2$ amongst all the simulated catalogues in the 5 band parametrisation.

The data are a substantially better fit to the fiducial linear matter power spectrum, which may be due to the additional variance added in at small scales by the velocity dispersion parameter, σ_*. With the total peculiar velocity covariance matrix defined as the sum of the 'velocity' and 'error' covariance matrices as in equation 2.5, velocity dispersion added in to the 'error' term of the covariance matrix has a similar effect to additional power added into the 'velocity' term of the covariance matrix. Although the peculiar velocity catalogues are – in principle – sensitive to density fluctuations on the scales of band 5, we must be cautious in interpreting results at these scales, since we are assuming with equation 2.8 that there is a linear relationship between the velocity power spectrum and the matter power spectrum. Since the matter distribution is non-linear at these scales, a fuller treatment of power spectrum estimation at these scales should include non-linear corrections to equation 2.8. Nevertheless, it would appear that the combination of a linear power spectrum and a single non-linear velocity dispersion parameter appears to be a good description of the clustering in the simulated catalogues.

3.2.2 Real Data

We now consider results from real peculiar velocity surveys. With the catalogue method, we find there is sufficient signal to analyse the constituent surveys individually - with the moments method, we only present results for the COMPOSITE catalogue analysed as a whole. We start with the one band-power and velocity dispersion parametrisation, with just the dipole moment, plotted in Figure 3.6, with the velocity dispersion marginalized (the marginalization only has

a very small effect when analysing the velocity moments). With just the dipole moment, we find a large excess of power compared to the fiducial value. We then repeat the analysis, including also the shear and octupole moments, shown in Figure 3.7. We now find good agreement with the fiducial model, which is mostly due to the low shear of the velocity field. We then repeat the analysis with the full composite catalogue. We plot these results as contours in Figure 3.8, which also includes the contour for COMPOSITE with dipole, shear, and octupole moments, for comparison.

Although we note a small excess, the ΛCDM value is within the 1σ uncertainty range of the moments result. We find that the results for the velocity dispersion agree well with similar results from Ma et al. [2010]. We find a smaller uncertainty in the band-power with the catalogue method than the moments method, and a much improved constraint on the velocity dispersion parameter. We next consider a three band parametrisation, shown in Figure 3.9. By comparison with the window functions plotted in Figure 2.1, we see that band 1 is dominated by the dipole moment, and band 2 is dominated by the shear and octupole. We can see that the good agreement with ΛCDM in Figure 3.7 is due to the combination of the high dipole and low shear, which we see in the three band power spectrum as a high band 1 and low band 2.

With the moments method, band 3 is merely an upper limit - it is well constrained with the catalogue method. The low shear of the velocity field caused band 2 to be lower than the ΛCDM expectation. When we now analyse the full catalogue, the band agrees extremely well with the ΛCDM expectation. We observe an excess of power in band 1, although the lower bound is not constrained here. These results are discussed further in Section 3.3. We next extend the parametrisation with two smaller bands, as before with the simulated catalogues. The results are plotted in Figure 3.10, and presented for COMPOSITE in Table 3.1. We find good agreement with ΛCDM in bands 3 and 4. We find that bands 1 and 2 are anti-correlated.

We can see in Figure 3.10 that the scatter in the data is fairly small compared to the uncertainties. In the COMPOSITE survey, all five bands are within the 1-σ error bars. As such, we find a fairly low χ^2 for all the surveys, shown in Table 3.2. This suggests that the uncertainties presented here may be overestimated.

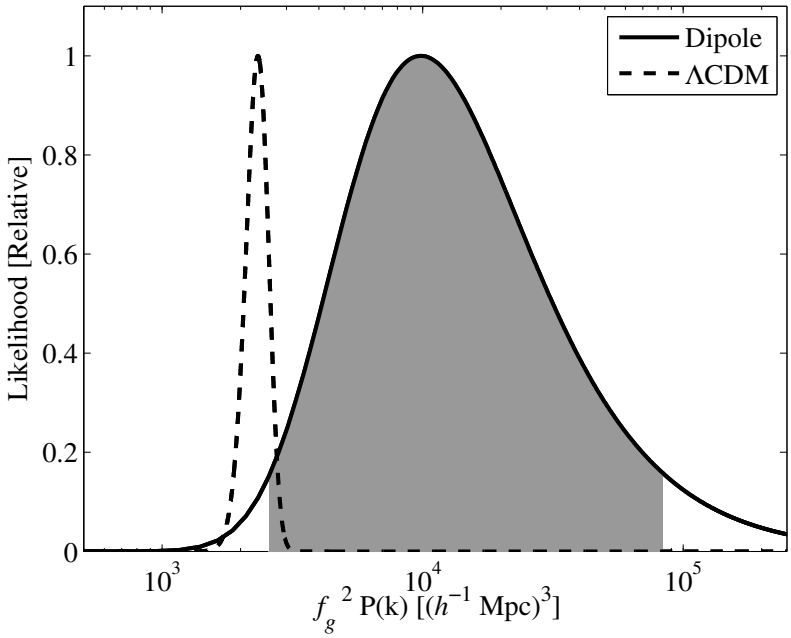

Figure 3.6: Likelihood results for the real COMPOSITE catalogue, including only the dipole. The fiducial ΛCDM value is illustrated with a dashed line, with an arbitrary ten percent standard deviation.

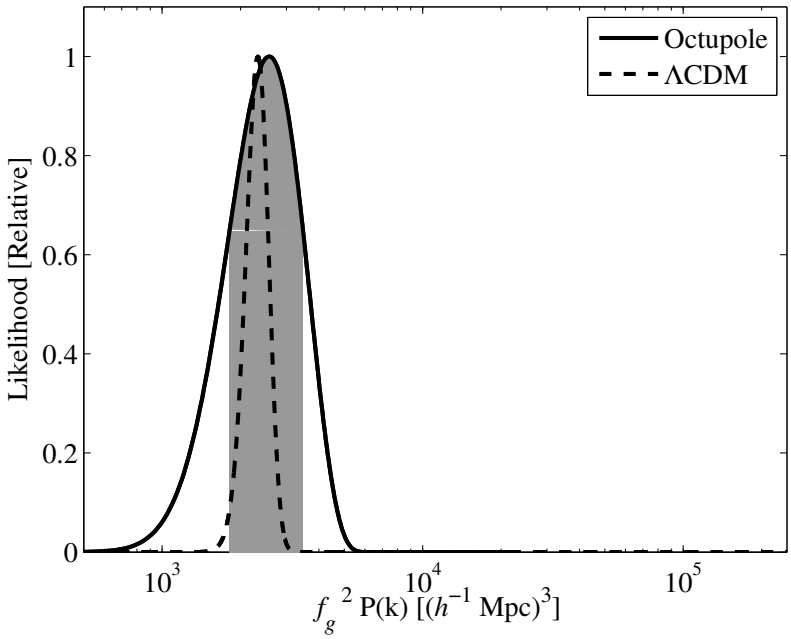

Figure 3.7: As figure 3.6, but now also including the shear and octupole moments.

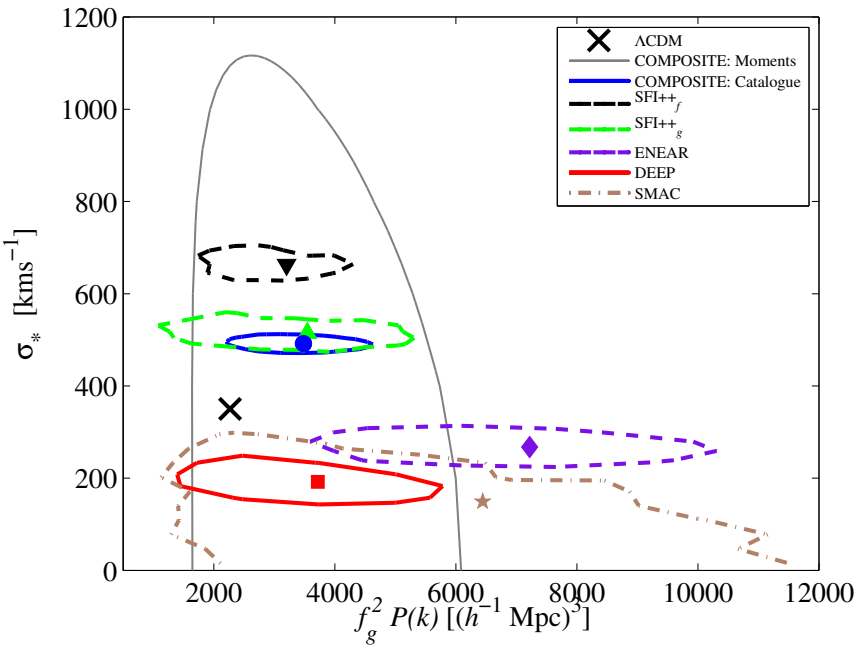

Figure 3.8: 1 standard deviation contours from the real data, parametrised in terms of the velocity dispersion σ_* and one band-power, in the range $k = 0.002$ to 0.196 h^{-1}Mpc. In all the catalogues, there is a slight excess in the $f_g^2 P(k)$ measurement, although within the 1σ level for most.

	$f_g^2 P(k)$ $[(h^{-1}\text{Mpc})^3]$	
Band	ΛCDM	COMPOSITE
1	4.2×10^3	$1.9^{+6.2}_{-1.9} \times 10^4$
2	6.2×10^3	$2.5^{+9.9}_{-2.5} \times 10^3$
3	2.2×10^3	$3.2^{+1.4}_{-1.1} \times 10^3$
4	2.8×10^2	$3.0^{+1.5}_{-1.0} \times 10^2$
5	1.6×10^1	$0.5^{+5.7}_{-0.5} \times 10^1$

Table 3.1: Results for the COMPOSITE catalogue five-band parametrisation, as plotted in Figure 3.10. Although the high dipole velocity leads to an excess of power by over a factor of 4 in band 1, the uncertainty includes the ΛCDM model within the 1σ uncertainty level.

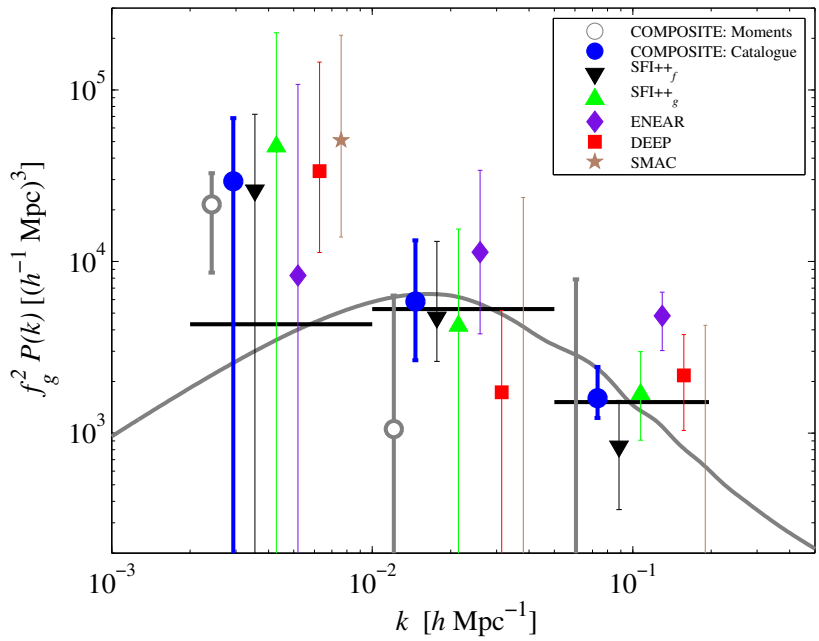

Figure 3.9: As Figure 3.3, but now for the real peculiar velocity catalogues. As before, the k position of each point within the bin is arbitrary, and each point should be fully considered at the centre of each band. The points have been ordered in each band from left to right by the number of galaxies in each catalogue. We also plot results from the moments analysis of the COMPOSITE catalogue.

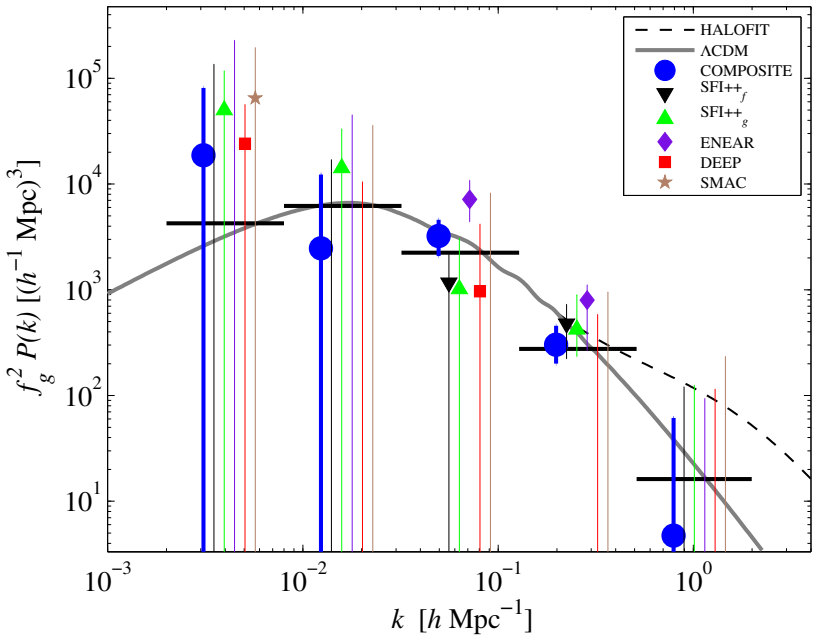

Figure 3.10: As Figure 3.4, now for real data. In band 1 we see a slight excess of power, although the uncertainty includes the ΛCDM model at the 1σ level. As with the simulated catalogues, band 5 favours the linear clustering power spectrum over the nonlinear model (although not as clearly).

Survey	χ^2
COMPOSITE	1.3
SFI++$_f$	2.2
SFI++$_g$	1.8
ENEAR	4.0
DEEP	3.2
SMAC	1.2

Table 3.2: χ^2 results for the 5-band parametrisation for the real surveys. For all the surveys, the χ^2 is less than the expected $\chi^2 \approx 5$ for the 5 bands we are fitting.

We find in the simulated catalogues χ^2 per degree of freedom very close to 1, which is suggestive that the overestimated uncertainties may be due to uncertainties in the distance indicators in the real catalogues, as opposed to the power spectrum estimation method. The difficulties of luminosity distance indicator measurements are well known, and can depend on the complicated astrophysics of the observed galaxies. In light of previous issues with high bulk flows in peculiar velocity data due to systematic errors, the low χ^2 per degree of freedom may be due to over-cautious inclusion of estimates of systematic uncertainties in the luminosity distance errors, which would yield a low χ^2 per degree of freedom when these uncertainties are treated as entirely statistical.

Comparison to Silberman et al. [2001]

We also test our methodology by reproducing the results of Silberman et al. [2001], to which our method is similar. We change our bands as follows, to match the bands used in their work: For $k \leq 0.02$ hMpc^{-1} we use a ΛCDM band, which we do not vary. In the range $0.02 < k \leq 0.07$ and $0.07 < k \leq 0.2$ hMpc^{-1} we use two independent flat bands of constant amplitude. For $k > 0.02$ hMpc^{-1} we use a power law band, $A_\alpha k^n$ The spectral slope n is set to -0.95 for the simulated Mark III catalogues, and to -1.4 for the real SFI++$_f$ catalogue, and the free parameter A_α is varied. The results are shown in Figure 3.11. We reproduce the slight decrement at $k \sim 0.1$ hMpc^{-1} as noted by Silberman et al. [2001], which we also observe in the SFI++$_f$ catalogue in band 3 of our 5 band parametrisation

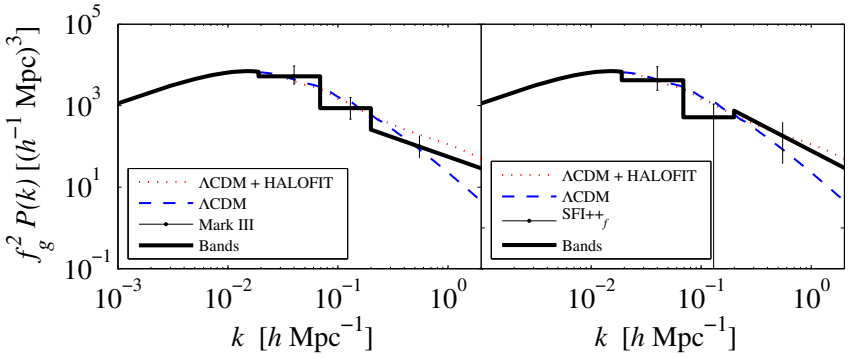

Figure 3.11: Analyzing a simulated Mark III catalogue and the genuine SFI++$_f$ catalogue with the parametrisation of Silberman et al. [2001]. The results we find here agree well with the results in Figure 7 of of Silberman et al. [2001].

in Figure 3.10.

3.2.3 Fitting a Velocity Dipole

In the three band model, we find that the uncertainty in band 1 is larger with the catalogue method than with the moments method. We see these results in the simulated catalogues, but it is particularly important to understand the result in the COMPOSITE catalogue since it is closely related to the high velocity dipole. As can be seen in Figure 2.1, the catalogue method window function is most similar to the window function of the shear moment, and (relatively) not as sensitive to the scales probed by band 1. To try and understand these results, we use our maximum likelihood method to estimate the dipole, to compare to the minimum variance dipole of Feldman et al. [2010]. Instead of varying the power spectrum, we fix the power spectrum at the fiducial ΛCDM value and minimise parameters of the dipole, as analysed by Ma et al. [2010]. We find that it is not possible to simultaneously constrain the three band-power spectrum and a velocity dipole. Following Ma et al. [2010], we model the dipole **U** by subtracting the line of sight component of the dipole to each galaxy in the catalogue from it's

line of sight peculiar velocity, S_n, to obtain a 'tilted' velocity, p_n

$$p_n = S_n - \hat{r}_n \cdot U \ . \tag{3.2}$$

We parametrise the dipole bulk flow as $\mathbf{U} = \{U_r, U_l, U_b\}$, where U_r is the magnitude of the bulk flow (in kms^{-1}), and U_l and U_b are the direction of the flow in degrees (galactic coordinates). We also include the velocity dispersion σ_* as a free parameter, which we marginalise over to find the dipole bulk flow. We find a dipole of magnitude $U_r = 380^{+99}_{-132}$ km s^{-1} in the direction $U_l = 295^{+18}_{-18}$ and $U_b = 14 \pm 18$ degrees. The direction of the dipole is shown in Figure 3.12. This is slightly slower and with a larger uncertainty than the dipole moment found by Feldman et al. [2010] of $U_r = 416 \pm 78$ km s^{-1} in the direction $U_l = 282 \pm 11$ and $U_b = 6 \pm 6$ degrees, and is related to the larger uncertainty we find in band 1 with the catalogue method than the moments method. A comparison of measurements of the dipole is shown in Table 3.3.

Results from many different surveys and analysis methods appear to agree on the *direction* of the velocity dipole, at around $l = 280$ and $b = 10$ degrees, within an uncertainty radius of about 15 degrees. However, there is less consensus as to the magnitude of the dipole. The magnitude of the dipole (and the corresponding uncertainty) can depend on the depth of the survey, the treatment of outliers, and the weighting of galaxies. Even so, we can very conservatively state that the magnitude of the velocity dipole out to 100 h^{-1} Mpc is a factor of several times higher than the ΛCDM expectation. However, one of the most important results that we emphasise here is that the dipole is a very incomplete representation of the velocity field. When we analyse the dipole alone, as shown in Figure 3.6 we indeed find evidence for a high power spectrum, which appears to be in tension with ΛCDM. However, when as we tend towards a more complete description of the velocity field, with additionally the shear and octupole moments, and then the full velocity catalogue, we find that the tension with ΛCDM decreases, to the extent that in Figure 3.10 we find good agreement with ΛCDM across a wide range of scales.

	U_r [kms^{-1}]	U_l [degrees]	U_b [degrees]
Watkins et al. [2009]	407 ± 81	287 ± 9	8 ± 6
Feldman et al. [2010]	416 ± 78	282 ± 11	6 ± 6
Ma et al. [2010]	340 ± 130	$285.1^{+23.9}_{-19.5}$	$9.1^{+18.5}_{-17.8}$
Nusser & Davis [2011] (SFI++, 40 h^{-1} Mpc)	333 ± 38	276 ± 3	14 ± 3
(SFI++, 100 h^{-1} Mpc)	257 ± 44	279 ± 6	10 ± 6
This work	380^{+99}_{-132}	295± 18	14 ±18

Table 3.3: Comparison of dipole measurements within 100 h^{-1}Mpc. This work, Watkins et al. [2009], Feldman et al. [2010] and Ma et al. [2010] all study the COMPOSITE catalogue, whereas Nusser & Davis [2011] study the SFI++ catalogue, which comprises the majority of COMPOSITE. The direction of the flow from different works agree well, although there is considerable variation in the magnitude of the flow. The magnitude of the flow can depend strongly on the depth of the survey, how galaxies at different depths are weighted, and the sensitivity of the method the fiducial power spectrum.

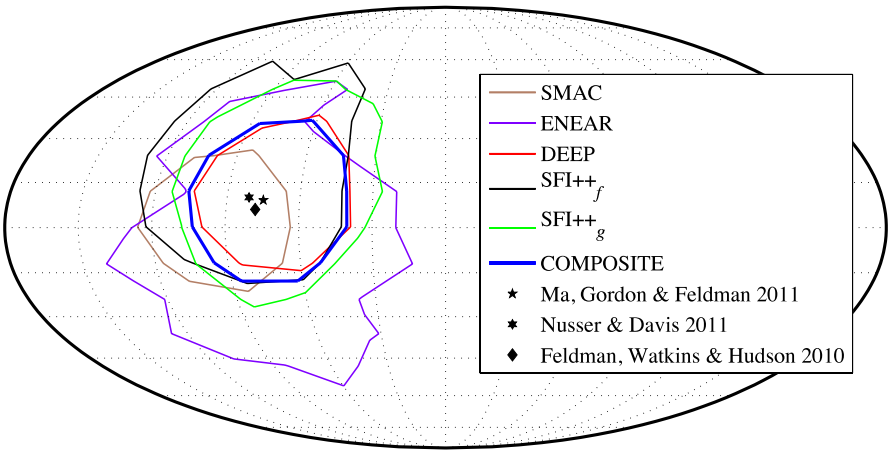

Figure 3.12: The direction of the best-fitting velocity dipole in the catalogues, (in a Mollweide projection of the sky in galactic coordinates). The contours represent 1 standard deviation levels on the dipole direction angles U_l and U_b found in the peculiar velocity catalogues. The direction agrees with other results from Feldman et al. [2010], Ma et al. [2010] and Nusser & Davis [2011].

3.3 Discussion & Conclusions

In terms of understanding the high dipole moment, the main difference between the two methods we have considered here is that the catalogue method finds an excess of power in band 1 with an uncertainty which includes the ΛCDM model at the 1σ level, while the moments method finds an excess of power with an uncertainty which excludes the ΛCDM model at over the 1σ level. This is the issue we now consider. The power spectrum at these scales is closely linked to the magnitude of the dipole moment, where we similarly find a larger uncertainty with the catalogue method than the minimum variance moments result. The key to the different results are the minimum variance weights, which are designed to be sensitive to the largest scales, at the expense of small scale information. Indeed, of the sub-catalogues we analyse with the catalogue method, band 1 is best constrained by the DEEP and SMAC samples, which are the deepest of the sub-catalogues considered here. While both DEEP and SMAC are included within COMPOSITE, we find that the additional, shallower galaxies are effectively acting as noise as far as constraints on band 1 are concerned. Essentially, the minimum variance weights achieve this effect to a maximal extent: preferentially weighting the deeper galaxies with the cleanest measurement of the velocity moments, at the expense of small scale information.

On smaller scales, we also find a difference between the two methods in band 2. We find that the catalogue method agrees extremely well with the ΛCDM model, while the moments method underestimates the power. This is due to the low shear of the velocity field, which provides most sensitivity at the scales of band 2. When we analyse the full velocity catalogue, the small scale motions not modelled by the moments appear to combine to provide a constraint which again agrees extremely well with ΛCDM. In much the same way as the one band parametrisation of the moments analysis illustrated the difference of including only the dipole, or additionally the shear and octupole, the result in band 2 highlights the effect of considering only moments of the velocity field, or the full information available to us.

In conclusion, we find that inferring the underlying power spectrum from peculiar velocity catalogues suggests that including more detail in the velocity field

improves the agreement with the ΛCDM model. Specifically, we observe good agreement with ΛCDM on scales of $k > 0.01\ h\mathrm{Mpc}^{-1}$, although the agreement with ΛCDM in band 1 from the catalogue method is only due to the larger uncertainty than the moments method. While the high dipole moment alone may appear anomalous, when we consider the full peculiar velocity measurements, we find a power spectrum which agrees well with the ΛCDM model.

Chapter 4

Fisher Forecasts for Galaxy Redshift Surveys

The previous chapters have concerned the analysis of current peculiar velocity data to measure the power spectrum. In the final chapter of this thesis, we will consider forecasts for future peculiar velocity surveys, and particularly how they compare with forecasts for galaxy redshift surveys. It is forecasts for galaxy redshift surveys that we now turn our attention to. In this chapter, we will consider forecasts for several upcoming galaxy redshift surveys. First, we will consider simple forecasts on the Hubble parameter, angular diameter distance, and growth rate, with fitting functions for the uncertainty on the distance indicators, and a numerical derivative Fisher matrix for growth rate uncertainty. We will then consider a full, numerical derivative Fisher matrix approach to forecast uncertainties on the underlying cosmological parameters, and compare to an alternative approach for forecasting uncertainties with redshift space distortion measurements. We will use the Fisher matrix formalism to address practical survey considerations of target selection optimisation and the effect of misidentified redshifts. In the next chapter, we will then consider extending forecasts for the standard cosmological model with additional parameters for dark matter and dark energy.

Galaxy redshift surveys are an established probe of dark energy and dark matter. By measuring the Hubble parameter and angular diameter distance via radial and tangential Baryon Acoustic Oscillations (BAOs), and simultaneously

measuring growth of structure via Redshift Space Distortions (RSDs), galaxy redshift surveys are a particularly powerful test of dark energy and alternative models. In this section we review previous galaxy redshift surveys, and the details for several upcoming surveys. As first pointed out in Peebles & Yu [1970], BAOs arise from acoustic waves in the primordial CMB plasma before matter-radiation decoupling. Sound waves corresponding to a characteristic scale around 150 Mpc — the size of the acoustic horizon at last scattering — imprinted density perturbations which can now be observed today in the distribution of galaxies. In contrast to the CMB, where this acoustic peak can only be measured in the tangential direction (constraining the angular diameter distance), measuring BAOs in the 3d distribution of galaxies additionally allows for the Hubble parameter to be measured from the radial BAOs.

The first surveys large enough to detect BAOs were the 2dFGRS and SDSS surveys [Percival et al., 2001, 2007a, 2010]. BAOs have also been detected at $z = 0.35$ in the SDSS Large Red Galaxies (LRG) sample [Eisenstein et al., 2005]. More recently, BAOs have been detected in the WiggleZ survey [Blake et al., 2011] and the BOSS survey [Anderson et al., 2012]. The growth rate of cosmic structure was first measured by Peacock et al. [2001], and has since been measured in the 2SLAQ [Ross et al., 2007], VVDS [Guzzo et al., 2008], WiggleZ [Blake et al., 2010], 2QZ+2SLAQ [da Ângela et al., 2008], LUQAS [Viel et al., 2004] and SDSS [Reid et al., 2012] surveys.

Many upcoming galaxy redshift surveys are planned within the next 10 years. In this thesis, we consider forecasts for the FAST-SOUND survey with the FMOS instrument on the Subaru telescope [Kimura et al., 2010], the Euclid mission [Laureijs et al., 2011], and the WEAVE survey [Balcells et al., 2010], although the method is general to any galaxy redshift survey.

FAST-SOUND[1] is an infra-red galaxy redshift survey with the FMOS instrument on the Subaru telescope. With a wavelength coverage of 0.9 to 1.8 μm, FMOS is sensitive to H_α emission lines in a redshift range of $0.8 < z < 1.7$. As of 2012, the first stage of the fast sound survey is currently being undertaken, consisting of a 30 deg^2 survey with around 10,000 measured redshifts, to measure

[1]FAST: FMOS "Ankoku Shindou Tansa" (Fmos "Dark Oscillation Survey", in Japanese) - SOUND: Subaru Observations Understanding Nature of Dark energy

the growth rate of cosmic structure at $z \sim 1.5$. Although the FAST-SOUND survey is substantially smaller than other contemporary dark energy surveys such as HETDEX [Hill et al., 2008] or the (photometric) DES survey [The Dark Energy Survey Collaboration, 2005], FAST-SOUND occupies a unique redshift range, which is well placed between the DES and HETDEX surveys. The growth rate measurement from the Lyman-α forest measurement form the LUQAS survey [Viel et al., 2004] is at a similar redshift to FAST-SOUND, although the RSD approach of FAST-SOUND is different and complementary to the LUQAS result.

WEAVE is a much larger proposed survey on the William Herschel Telescope, planned to start in 2017, for a five year survey. The survey model we consider here assumes a measurement of several million galaxy redshifts, over 10,000 deg^2. Euclid is a proposed space-based mission, combining weak lensing and spectroscopic redshift measurements, due to start in 2019, with a mission duration between five and seven years. We also compare results to the proposed BigBOSS survey [Schlegel et al., 2011], which may start around 2019. The survey would cover 24,000 deg^2, and measure the redshifts of 24 million galaxies.

For the Fisher matrix approach we take to forecasting uncertainties, a galaxy redshift survey is described entirely by the central redshift, the volume of space probed by the survey, the density of galaxies, and the bias of the galaxies. In practice, the volume and density of the survey are typically specified by the area (of the sky), and the total number of redshifts. The volume of the survey for a given area is calculated as presented in Hogg [1999], with code from Bassett et al. [2009].

The Euclid and WEAVE surveys will span a significant redshift range. In these cases, we treat the survey as a series of independent surveys, within redshift bins of width $\Delta z = 0.1$. Tables 4.1 and 4.2 detail the specifications of the Euclid and WEAVE surveys. The Euclid model assumes a constant galaxy density of $1 \times 10^{-3}\ h^{-3}\mathrm{Mpc}^3$ and a linear bias of 1.7. The survey model assumes 15 redshift bins of width $\Delta z = 0.1$ from $z = 0.5$ to $z = 2.0$. The maximum k scale was given by Wang et al. [2010], and is cut off at a maximum $k = 0.2h$ Mpc^{-1}.

Uncertainty in the angular diameter distance was forecast for the WEAVE survey with the fitting function of Blake et al. [2006] with code implemented by Bassett et al. [2009]. The uncertainty does not depend strongly on the bias of

Central Redshift	Volume (h^{-3}Gpc^3)	$k_{\max}(h\text{Mpc}^{-1})$
0.571	1.64	0.146
0.673	1.91	0.156
0.775	2.15	0.166
0.877	2.36	0.189
0.979	2.53	0.20
1.081	2.67	‘’
1.183	2.79	↓
1.285	2.88	
1.387	2.96	
1.489	3.02	
1.591	3.07	
1.693	3.12	
1.795	3.13	
1.897	3.15	
1.999	3.16	
Total volume	43.68	
Total galaxies	43.68 million	

Table 4.1: Details of the Euclid survey model. A constant galaxy bias of 1.7 and density of 1×10^{-3} h^3Mpc^{-3} was assumed.

Redshift	Volume (h^{-3}Gpc^3)	Density ($\times 10^{-3}$ h^3Mpc^{-3})	Galaxies (Millions)	Variable Bias	$k_{\max}$ (hMpc^{-1})
0.5 to 0.6	0.91	0.78	0.71	0.93	0.15
0.6 to 0.7	1.06	0.70	0.74	0.99	0.16
0.7 to 0.8	1.20	0.64	0.77	1.05	0.17
0.8 to 0.9	1.31	0.59	0.77	1.11	0.18
0.9 to 1	1.40	0.55	0.78	1.17	0.19
1 to 1.1	1.48	0.51	0.76	1.23	0.20
1.1 to 1.2	1.55	0.48	0.74	1.29	‘’
1.2 to 1.3	1.60	0.44	0.71	1.35	↓
2.2 to 2.3	1.75	0.22	0.38	1.95	
2.3 to 2.4	1.74	0.20	0.34	2.01	
2.4 to 2.5	1.73	0.18	0.31	2.07	
2.5 to 2.6	1.72	0.16	0.28	2.13	
2.6 to 2.7	1.71	0.15	0.26	2.19	
2.7 to 2.8	1.70	0.14	0.24	2.25	
2.8 to 2.9	1.69	0.13	0.22	2.31	
2.9 to 3	1.67	0.12	0.20	2.37	
3 to 3.1	1.66	0.11	0.19	2.43	
3.1 to 3.2	1.64	0.11	0.18	2.49	
Total	27.15	-	8.03	-	-

Table 4.2: Details of the WEAVE survey model. The galaxy density includes a 20% loss. Results were also forecast with a fixed bias of 1.7.

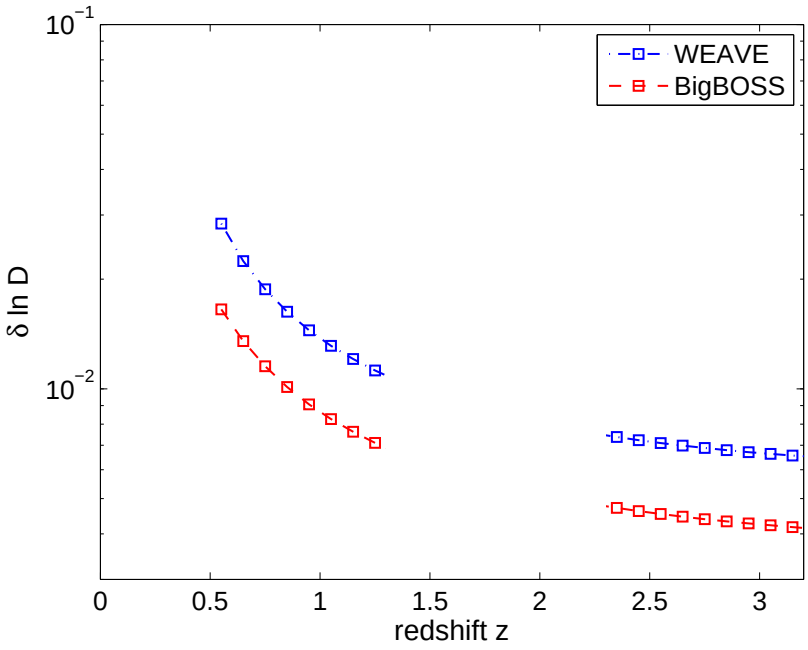

Figure 4.1: Forecast uncertainty in the angular diameter distance for WEAVE and BigBOSS. The redshift range is determined by the possible emission lines visible to the ground based, optical and near infra-red surveys. The 0.5 to 1.3 redshift range is measured with H_α emission lines, and the 2.2 to 3.2 redshift range is measured with OII emission lines. Due to the absence of suitable emission lines, the redshift range 1.3 to 2.2 is inaccessible to optical surveys; infra-red instruments such as FMOS are required to survey galaxies in this redshift range.

the sample. The results are shown in Figure 4.1.

4.0.1 Fisher Forecasts

Fisher matrices are widely used in cosmology to forecast uncertainties in parameters Θ of an underlying model of an observable X given an uncertainty in a measurement of X, σ. Bassett et al. [2011]; Coe [2009]; Dodelson [2003] provide an introduction to Fisher matrices for cosmology. The Fisher matrix provides the lowest possible intrinsic statistical uncertainty, thus results from Fisher forecasts are optimistic when compared to real results. The Fisher matrix F_{ab} is defined as the Hessian matrix of the log-likelihood, as in equation 4.1, and is the inverse

of the covariance matrix.

$$F_{ab} = -\left\langle \frac{\partial^2 \ln \mathcal{L}}{\partial \Theta_a \partial \Theta_b} \right\rangle \ . \tag{4.1}$$

We will assume that the likelihood for our model X (which depends on parameters Θ) given data d with measurement uncertainty σ can be described by a Gaussian distribution. If we also assume that the measurement uncertainties σ are uncorrelated, we can write the likelihood as

$$\mathcal{L}(X(\Theta)|d) \propto \prod_i \exp\left(\frac{(X_i - d_i)^2}{2\sigma_i^2}\right) \tag{4.2}$$

so the log-likelihood is given by

$$\ln \mathcal{L}(X(\Theta)|d) \propto \sum_i \frac{1}{\sigma_i^2} (X_i - d_i)^2 \ . \tag{4.3}$$

If we assume that the measurement uncertainty σ is independent of the parameters of the model, and substitute this expression for the log-likelihood into equation 4.1 we find that the Fisher matrix is given by

$$F_{ab} = \sum_i \frac{1}{\sigma_i^2} \frac{\partial X_i}{\partial \Theta_a} \frac{\partial X_i}{\partial \Theta_b} \, . \tag{4.4}$$

The measurement uncertainty σ must be estimated if we wish to use a Fisher matrix to forecast uncertainties for future measurements. For the galaxy surveys we consider here, this is determined by the 'effective volume', $V_{\rm eff}$. Working with the Fisher matrix is particularly useful since it allows forecasted constraints from different surveys A and B to be easily combined to provide combined forecasted uncertainties from both surveys, so that $F_{ij}^{\rm Total} = F_{ij}^{A} + F_{ij}^{B}$. Parameters can be fixed by simply removing the parameter's row and column from the Fisher matrix. By inverting the Fisher matrix to calculate the covariance matrix, the correlated parameter uncertainties are naturally marginalised in the covariance matrix.

4.1 Redshift Space Distortion Fisher Matrix

For most of the Fisher forecasts presented here, we will consider the galaxy power spectrum as our observable. However, we will first consider a new Fisher matrix, based on treating the redshift space distortion compression parameter β as an observable. This approach has the advantage that the derivatives can all be calculated analytically. The method provides a good estimate of the uncertainty on the modified gravity parameter γ, although tends to underestimate the uncertainty on Ω_m, since other densities cannot be included in this formalism as free parameters. We will use the empirical fitting formula for σ_β, calibrated by Guzzo et al. [2008] to Monte-Carlo simulations of measurements of β from galaxy surveys,

$$\frac{\sigma_\beta}{\beta} = \frac{50}{V^{1/2} n^{0.44}} \,. \tag{4.5}$$

V is the volume of the survey in $h^{-3}\mathrm{Mpc}^3$, and n is the density of galaxies in $h^3\mathrm{Mpc}^{-3}$. The uncertainty is essentially proportional to the square root of the total number of galaxies. The power of 0.44 in the density of galaxies is simply a parametric fit to results from simulated data by Guzzo et al. [2008], and introduces a slight departure on the proportionality of the uncertainty to simply the square root of the total number of galaxies in the survey.

We use the Peebles approximation for β, in terms of Ω_m, γ and bias as in

$$\beta = \frac{\Omega_m^\gamma}{b} \,. \tag{4.6}$$

Using equation 4.4, the Fisher matrix is then given by

$$F = \frac{1}{\sigma_\beta^2} \begin{bmatrix} \left(\frac{\partial\beta}{\partial\gamma}\right)^2 & \frac{\partial\beta}{\partial\gamma}\frac{\partial\beta}{\partial\Omega_m} & \frac{\partial\beta}{\partial\gamma}\frac{\partial\beta}{\partial b} \\ \frac{\partial\beta}{\partial\gamma}\frac{\partial\beta}{\partial\Omega_m} & \left(\frac{\partial\beta}{\partial\Omega_m}\right)^2 & \frac{\partial\beta}{\partial\Omega_m}\frac{\partial\beta}{\partial b} \\ \frac{\partial\beta}{\partial\gamma}\frac{\partial\beta}{\partial b} & \frac{\partial\beta}{\partial\Omega_m}\frac{\partial\beta}{\partial b} & \left(\frac{\partial\beta}{\partial b}\right)^2 \end{bmatrix} \tag{4.7}$$

The derivatives can be calculated directly from equation 4.6, and are given by

$$\frac{\partial\beta}{\partial\gamma} = \beta \ln\left(\Omega_m\right) \tag{4.8}$$

$$\frac{\partial \beta}{\partial \Omega_m} = \left(\frac{\gamma}{b}\right) (\Omega_m)^{\gamma-1} \tag{4.9}$$

$$\frac{\partial \beta}{\partial b} = -\frac{\Omega_m^{\gamma}}{b^2} \,. \tag{4.10}$$

We thus have all the ingredients to calculate error ellipses on γ and Ω_m as a function of survey volume, redshift, galaxy density, and bias. In Figure 4.2, Fisher ellipses are plotted for the redshift space distortion Fisher matrix. Since we only consider the compression parameter as the observable (as opposed to the full power spectrum), we have added priors to Ω_m and b. We next compare this Fisher matrix method to a full, power spectrum based formalism. In Figure 4.3, results from both methods are compared. Both methods agree well on uncertainty on γ, although the redshift space distortion only method significantly underestimates the uncertainty on Ω_m. This is because this method can only treat γ, bias and Ω_m as free parameters. Other parameters which are correlated with Ω_m would increase the uncertainty in the marginalised Fisher ellipse. This method is interesting to test the relationship between the empirical fitting function for uncertainties in β (equation 4.5) and the corresponding uncertainties on γ. Although the method appears to successfully forecast uncertainties on γ, we will not consider it further, due to the limitations in forecasting uncertainties on other parameters. In the following forecasts we will consider the full two dimensional redshift space galaxy power spectrum as our observable, which offers much more flexibility to include other parameters.

4.2 Power Spectrum Fisher Forecasts

We now consider Fisher forecasts treating the full power spectrum as an observable. Tegmark [1997] showed that for a galaxy redshift survey, the Fisher matrix is given by:

$$F_{ij} = \int_{\vec{k}_{\rm min}}^{\vec{k}_{\rm max}} \frac{d^3\vec{k}}{2(2\pi)^3} \left(\frac{\partial \ln P(\vec{k})}{\partial \Theta_i}\right) \left(\frac{\partial \ln P(\vec{k})}{\partial \Theta_j}\right) V_{\rm eff}(\vec{k}) \tag{4.11}$$

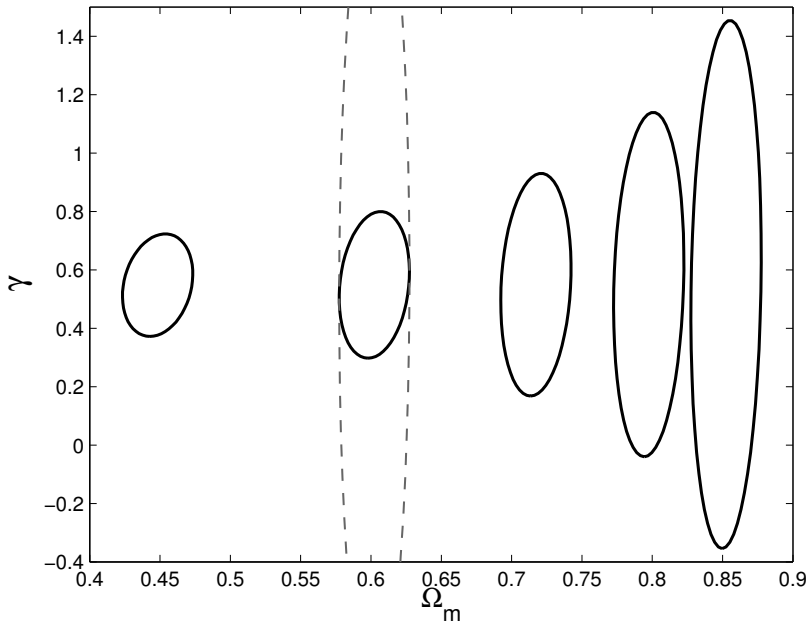

Figure 4.2: Forecasts for constraints on $\Omega_m(z)$ and γ from the redshift space distortion Fisher matrix. Each ellipse corresponds to 100,000 redshifts, distributed in a 1.0 h^{-3}Gpc^3 survey, with a galaxy density of 10^{-4} h^3 Mpc^{-3}. The mean redshift of each ellipse (from left to right) is 0.3, 0.6, 0.9, 1.2, and 1.5. 10% priors have been added to Ω_m and b; these should be possible to achieve from fitting to the full power spectrum. To illustrate the effect of bias, the second ellipse has also been plotted (dashed) with just a 50% prior on bias.

The 'effective volume', $V_{\rm eff}$, essentially provides a weighting for the uncertainty in each $P(k)$, and (assuming constant galaxy density) is given by

$$V_{\rm eff}(k) = V_0 \left(\frac{nP(k)}{1 + nP(k)} \right)^2 \tag{4.12}$$

V_o is the volume of the survey and n is the galaxy density. The biased, redshift space galaxy power spectrum is

$$P(k,\mu) = b^2 \left(\frac{1}{1 + (k\mu\sigma_v)^2/2} \right) \left(1 + \frac{f_g}{b}\mu^2 \right)^2 P(k) \,, \tag{4.13}$$

where μ is the cosine of k modes parallel and perpendicular to the line of sight. The b^2 term accounts for the linear galaxy bias, and the σ_v term introduces small scale velocity dispersion. The f term models the large scale growth. The Fisher matrix can now be written in terms of μ and the magnitude of $\vec{k}$

$$F_{ij} = \int_{-1}^{1} \int_{k_{\rm min}}^{k_{\rm max}} \frac{2\pi dk d\mu}{2(2\pi)^3} \left(\frac{\partial \ln P(k,\mu)}{\partial \Theta_i} \right) \left(\frac{\partial \ln P(k,\mu)}{\partial \Theta_j} \right) V_{\rm eff}(k) \,. \tag{4.14}$$

The fiducial parameter set used is shown in table 4.3. As can be seen in Figure 6.4, there is a very large uncertainty on the power spectrum at large scales. As such, the results are insensitive to k_{min}, which we set to zero. k_{max} was set according to values in Wang et al. [2010]. In Figure 4.3, we compare this Fisher matrix to the redshift space distortion based approach, and also compare to the similar Fisher matrix from Simpson & Peacock [2010]. We find that the power spectrum Fisher matrix combined with the Planck Fisher matrix agrees well with the Fisher matrix from Simpson & Peacock [2010] (which is for the same parameters for the galaxy redshift survey, and combined with forecast Planck priors).

4.3 Growth Rate Forecasts

In this section we use the method of White et al. [2009] to forecast uncertainties on the growth rate. The method assumes a redshift space power spectrum given

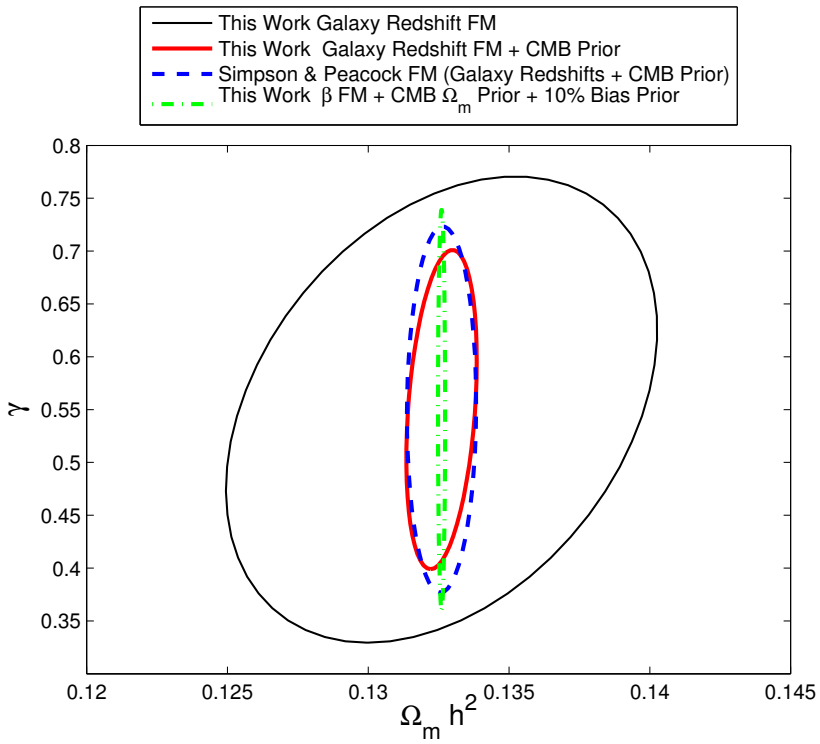

Figure 4.3: A comparison of three different Fisher matrices. The dashed blue ellipse is from the $z = 0.5$ Fisher matrix from Simpson & Peacock [2010]. The Fisher matrix which treats the RSD parameter β as an observable (green, dot-dashed ellipse) underestimates the uncertainty in $\Omega_m h^2$ because the method only includes γ and bias as additional free parameters.

Parameter	Fiducial Value
w	-1
Ω_k	0
$\Omega_m h^2$	0.13
$\Omega_b h^2$	0.02
n_s	0.963
$\ln(P)$	$\ln(2.3\mathrm{E}-9)$
γ	0.55
b (bias)	1.4

Table 4.3: Fiducial Parameters

by

$$P(k,\mu) = (b + f\mu^2)^2 P(k) e^{-k^2\sigma_v^2\mu^2} \tag{4.15}$$

with bias, b, growth rate, f, and velocity dispersion σ_v. The key idea is that the uncertainty in the fundamental cosmological parameters which specify the 1D matter power spectrum $P(k)$ (e.g. w, Ω_m, Ω_Λ) will be small, and driven by priors from the CMB, when compared to the galaxy biasing parameters b, f, and σ_v. By treating only b, f, and σ_v as free parameters, the derivatives are simple to calculate from equation 4.15, and are given by

$$\frac{\partial \ln P(k)}{\partial b} = \frac{2}{b + f\mu^2} \tag{4.16}$$

$$\frac{\partial \ln P(k)}{\partial f} = \frac{2\mu^2}{b + f\mu^2} \tag{4.17}$$

$$\frac{\partial \ln P(k)}{\partial \sigma_v^2} = -k^2\mu^2 \,. \tag{4.18}$$

These derivates can then be combined to calculate the Fisher matrix. Marginalised results for the growth rate uncertainty are plotted in Figure 4.4 for the WEAVE survey, compared to the BigBOSS survey. Figure 4.5 illustrates the growth rate forecast for Euclid, compared to current measurements, and theoretical models.

In this next section we use the Fisher matrix methods presented here to quantify practical survey design concerns. We start by considering the optimum red-

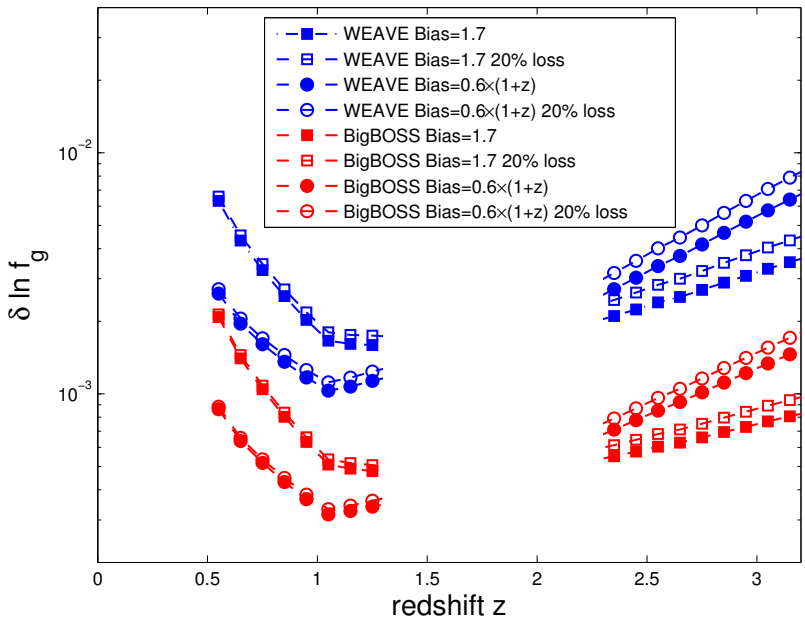

Figure 4.4: The uncertainty in the growth rate for WEAVE (in blue) and BigBOSS (in red), for several different survey assumptions. The square markers are for a fixed bias of 1.7, and the round markers are for a redshift dependent bias. Filled markers are under the assumption of no redshift loss, and open markers are for a (more realistic) assumption of a 20% loss.

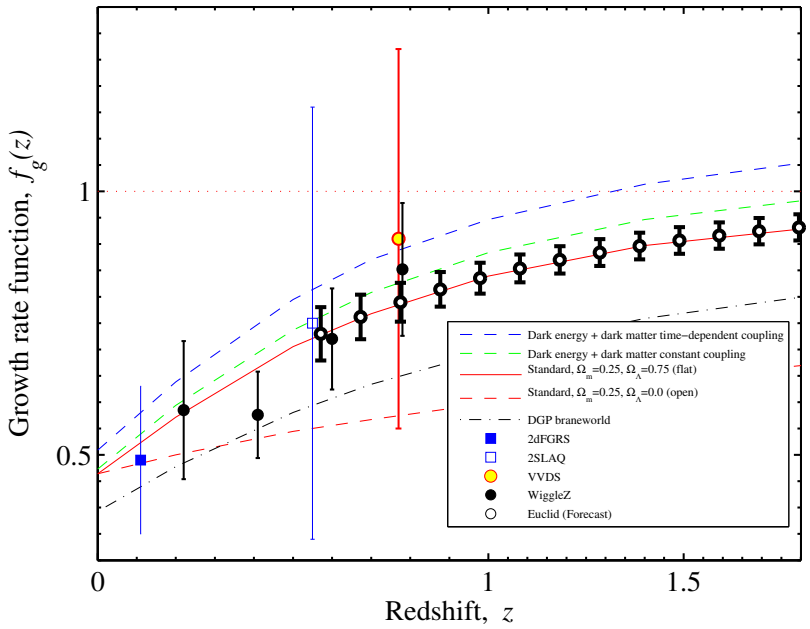

Figure 4.5: The forecast growth rate measurements for Euclid, compared to current measurements and theoretical models. Several growth rate models are plotted (based on Guzzo et al. [2008]) for ΛCDM (solid red line), an Open-CDM model (dashed red line), the DGP model of Dvali et al. [2000] (black, dot-dashed line), and coupled dark matter dark energy models with constant coupling (blue dashed line) and time-dependent coupling (green dashed line). Current RSD measurements of the growth rate are plotted, including 2dFGRS from Peacock et al. [2001], 2SLAQ from Ross et al. [2007], VVDS from Guzzo et al. [2008], WiggleZ Blake et al. [2010], 2QZ+2SLAQ. Forecast measurements for Euclid are plotted in solid, open circles.

shift distribution of targets for a survey with the FMOS instrument.

4.4 FMOS Survey Figure of Merit Optimisation

In this section, we consider the optimal redshift distribution of 200,000 targets for a redshift survey with FMOS. The instrument has two bands: J and H – measuring H_α flux in these bands corresponds to two redshift ranges of $0.7 < z < 1.0$ and $1.3 < z < 1.7$. The question we wish to address is to find the best distribution of targets between the two redshift bins. We find that the best distribution can result in a factor of two increase in the survey Figure of Merit (FoM), but depends slightly on which combination of parameters are most interesting.

A simple way to quantify the success of a survey is the Figure of Merit (FoM) recommended by the Dark Energy Task Force: the inverse of the area of the w_o w_a 2σ error ellipse. Simpson & Peacock [2010] recommend $w_{\rm pivot}$ γ as more natural parameters to consider for the FoM, where $w_{\rm pivot}$ is the value of w at the redshift where w_o is uncorrelated with w_a.

To optimise the FMOS survey, two separate Fisher matrices were calculated with mean redshifts centred on the high and low z bins, respectively. A galaxy density of 10^{-4} h^3 Mpc^{-3} was assumed for both bins, and, following Simpson & Peacock [2010], a bias of $0.6 \times (1 + z)$ was assumed. The total volume was set to $2h^{-3}$Gpc^3, shared between both surveys, to yield a total of 200,000 targets. The Fisher matrices were summed and combined with the Planck Fisher matrix from Mukherjee et al. [2008]. The FoM for various combinations of parameters was then calculated from the final Fisher matrix. This process was then repeated for a range of volume distributions, from all the survey volume in the low redshift bin, to all the survey volume in the high redshift bin. The results are shown in Figure 4.6.

We can see that by having a mixture of targets between high and low redshift bins, we achieve around twice as high a FoM than including all targets in one redshift bin. The best mixture appears to be with around 60% of targets in the high redshift bin. Precisely the best configuration depends on which parameters are of most interest. For the genuine FMOS survey, we are likely to select H band

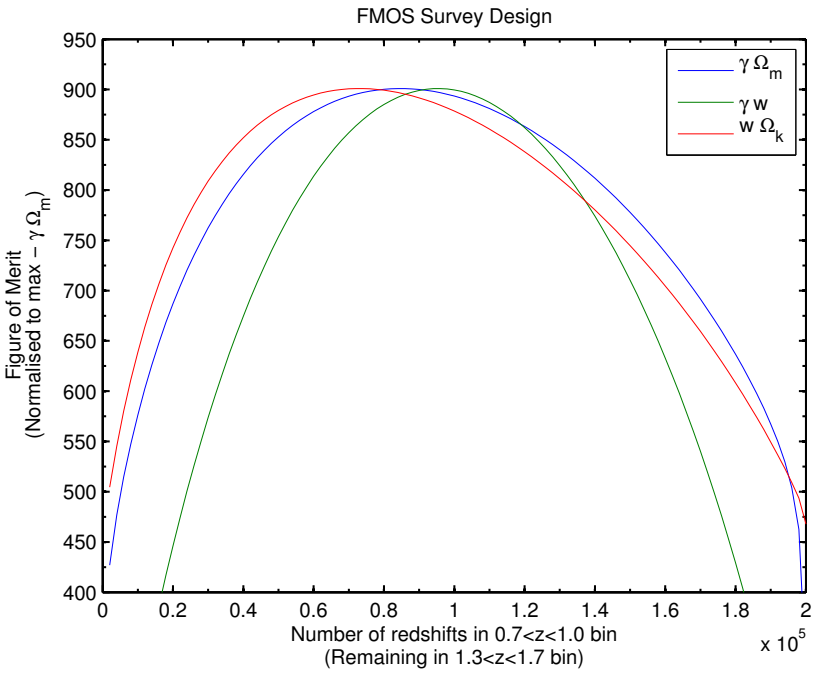

Figure 4.6: FoM for various combinations of parameters. As the most important feature is the relative FoM, the three functions have been normalised.

targets as much as possible, to make best use of the unique infrared range of the instrument. However, this analysis illustrates the potential to optimise surveys for parameter measurement based on target redshift distribution.

4.5 Redshift Contamination

In this section we address the issue of misidentified emission lines on the power spectrum for the Euclid mission. It is expected that a fraction F of the classified H_α emission line redshifts will in fact be other emission lines, incorrectly identified as H_α. Here, we assume that these incorrectly identified redshifts will behave as additional random points within the correctly identified population, so the net effect will be that the additional misidentified fraction will act as white noise in the power spectrum. We model this scale independent noise as

$$P(k)_{\text{contaminated}} = (1 - F)^2 P(k) \tag{4.19}$$

In reality, this effect may be slightly more subtle; if a subset of other emission lines are systematically misidentified as H_α, it would have the effect of incorrectly mapping a population of galaxies at one redshift onto the population of another. That is, within the fraction of misidentified galaxies, there may be (small, randomly sampled) clusters of populations from different redshifts. We do not consider these additional effects in these forecasts.

We use equation 4.19 and the Fisher matrix approach previously described to estimate the effect of this contamination on the w_0-w_a Figure of merit. The effect of this contamination fraction on the w_0-w_a Figure of merit can be calculated by comparing results from uncontaminated Fisher forecasts to results with a particular contaminating fraction. To calculate the total Fisher matrix for each Euclid survey, individual Fisher matrices were calculated for each redshift bin, and then summed. This was then repeated for each contamination fraction. The decrease in Figure of merit is shown in Figure 4.7 as a function of the contamination fraction. As can be seen in the figure, the figure of merit decreases linearly with increasing contamination fraction. For a 20% contamination fraction, the Figure of merit is reduced to 67%. A 40% contamination reduces the Figure of

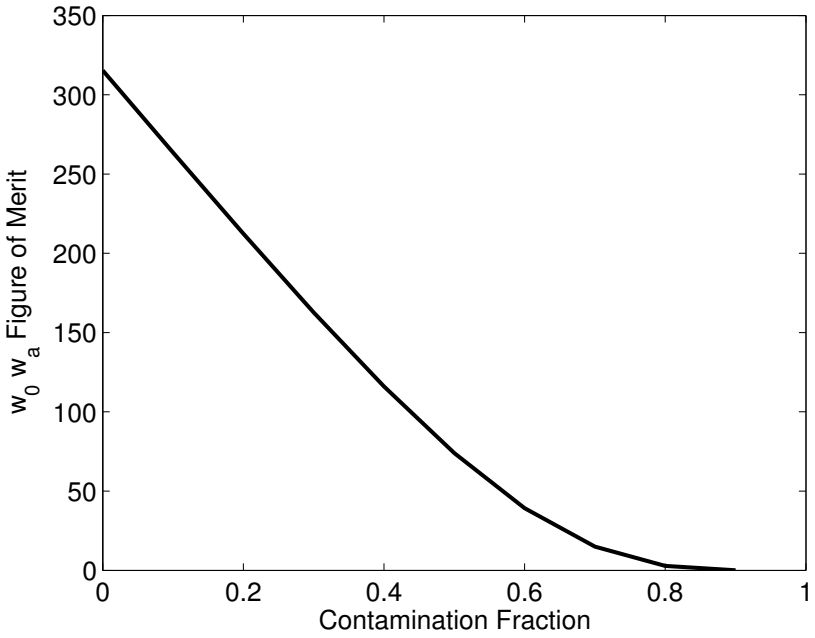

Figure 4.7: The *wo-wa* Figure of merit as a function of contamination fraction.

merit to 37%. γ-Ω_Λ and γ-w Figures of merit have a similar dependence.

4.6 Discussion & Conclusions

In this chapter, we have presented several methods to forecast possible results with future galaxy redshift surveys, and quantify survey design characteristics such as target distribution and the effect of misidentified redshifts. The methods presented here can be used to start from basic survey specifications, such as the total number of spectroscopic targets, the galaxy bias of the targets, the fraction of the sky covered, and redshift range, and forecast uncertainty in the growth rate, Hubble parameter, angular diameter distance, and underlying cosmological parameters. Of the different approaches presented here, the numerical derivative, power spectrum approach is the most flexible, and is most sensitive to effects such as galaxy bias and redshift contamination (which are both treated in a similar manner). This method also has the advantage that it is most readily extended to other cosmological parameters, which we will consider in the next chapter.

Chapter 5

Forecasts for Extended Cosmological Models

In this chapter, we use the power spectrum Fisher matrix formalism presented in the previous chapter to consider the potential to constrain extended dark matter and dark energy models with the next generation of galaxy redshift surveys. Although current galaxy surveys have placed strong constraints on the density of cold dark matter, Ω_c, the nature of the dark matter is still uncertain. The next generation of cosmological surveys may be sufficiently large to allow the nature of the dark matter to be probed in more detail. In section 5.1 we present results on forecast constraints on axion dark matter. In section 5.2 we present preliminary results on testing the assumptions of General Relativity with a parameterised modified gravity model.

5.1 Axion Dark Matter Forecasts

In this section we consider the potential to identify traces of axion dark matter with some of the cosmological probes of the upcoming decade. The axion was first proposed to account for CP-violation, although the mass of the axion must be very finely tuned to account for primordial matter-antimatter asymmetry. More recently, ultra-light axions have been considered as potential dark matter candidates, where the mass of the axion determines whether it behaves as hot or

cold dark matter (for example, Marsh [2011] and Marsh & Ferreira [2010]).

In the axion models we consider here, the axion density initially behaves as a cosmological constant, then at a redshift z_{osc} begins to oscillate about it's potential and transitions to dark-matter like behaviour. z_{osc} depends on the mass of the axion, and for the range of masses we consider here, always occurs between decoupling and dark energy dominance. There are two main effects that the axion has on our cosmology: At $z > z_{osc}$, increasing the fraction of CDM in axions affects the background expansion, by effectively removing the matter contained in the CDM. Once the axion has started oscillating, it suppresses structure formation in a similar manner to neutrino free streaming. This imprints a step in the matter power spectrum at a characteristic scale k_m, (which depends on the mass of the axion), and also affects the growth rate as measured by redshift space distortions.

We consider here an ultra-light scalar field axion, which can act as matter, radiation, and a cosmological constant, and causes steps in the matter power spectrum as the axion transitions between different states. We consider the axion as parameterised by a mass, m_a, and the fraction of Ω_c constituted by axions, f_{ax}. Current measurements already rule out $f_{ax} \gtrsim 5\%$. We assume a fiducial value of $f_{ax} = 1\%$. We find that the forecasts are unable to constrain m_a, so we do not treat this a free parameter, although the forecasts are run for a range of fiducial masses.

The galaxy redshift survey power spectrum Fisher matrix approach from the previous chapter is used to forecast uncertainties on f_{ax}, with the Euclid survey model, as detailed in Table 4.1. These results are combined with weak lensing forecasts[1], and forecasts for an all sky CMB survey, based on the Planck mission. The CMB forecasts are made with the pre-existing package "FisherCodes" [Das, 2011]. We set the survey specifications for a Planck-style mission based on Albrecht et al. [2006]. TT, TE and EE spectra were used, to $\ell_{\rm max} = 2000$, with $f_{\rm sky} = 0.8$. Three channels at 100, 143, 217 GHz were used, with beam full-width half-maximum set to 9.5', 7.1' and 5.0'. The temperature noise per pixel was set to 2.5, 2.2 and 4.8, and the polarisation noise per pixel was set to 4, 4.2 and 9.8 $\times 10^6$ $\Delta_T/T_{\rm CMB}$. In Figure 5.1 we compare the results from FisherCodes with these settings to other Planck Fisher matrices from Mukherjee et al. [2008] and

[1] with Fisher matrices and code by Maxime Trebitsch

Albrecht et al. [2006], for a standard ΛCDM cosmology. A small prior was required to regularise the matrix from Mukherjee et al. [2008] (which was calculated from a monte-carlo model of the Planck survey), this was also added to the other matrices so they can be directly compared. The forecasts agree well for w, Ω_k, $\Omega_m h^2$ and $\Omega_b h^2$, although our forecast for n_s has a smaller uncertainty than the other two forecasts. This may be due to the slightly different survey models used by all three forecasts. Albrecht et al. [2006] use the same polarisation channels as we use here, although they extend the ℓ scales for polarisation to 2500, and cut off all channels below $\ell = 30$. Mukherjee et al. [2008] use the same ℓ range as here, although only include polarisation from the 143 GHz channel.

We first consider a cosmology with massive neutrinos and a fraction of CDM in axions. We assume a fiducial model with a constant dark energy equation of state $w = -1$, baryon density $\Omega_b h^2 = 0.02258$, dark matter density $\Omega_c h^2 = 0.1109$, spectral tilt $n_s = 0.963$, scalar amplitude $A_s = 2.3 \times 10^{-9}$, neutrino mass $m_\nu = 0.055$ eV, the effective number of massive neutrinos $N_{\rm eff} = 3.04$ and fraction of dark matter in axions $f_{ax} = 0.01$. Following Albrecht et al. [2006], we also include the optical depth to reionization $\tau = 0.166$ and helium fraction $Y_{He} = 0.24$ as free parameters in the CMB Fisher matrix. Similarly, galaxy bias $b = 1.7$ and non-linear velocity dispersion $\sigma_v = 350$ kms^{-1} were included as free parameters in the galaxy redshift survey Fisher matrix. These parameters were marginalized over before the matrices were combined. CMB, galaxy redshift survey and weak lensing Fisher matrices were calculated for this fiducial cosmology for $m_a = 10^{-29}, 10^{-30}, 10^{-31}$ and 10^{-32} eV. As an example, Fisher ellipses for the $m_a = 10^{-30}$ eV case are plotted in Figure 5.2 for axion and neutrino parameters.

Increasing the fraction of CDM in axions (f_{ax}) is directly related to the size of the step in the power spectrum, and consequently directly related to how well f_{ax} can be measured. As for the neutrinos, increasing $N_{\rm eff}$ effectively adds in more radiation density at high redshift, which affects matter-radiation equality. In a similar manner to axions, the neutrino mass m_ν affects the free streaming scale of the neutrinos, below which growth of structure is suppressed.

With the different sets of forecasts over a range of axion mass, we can compare how the fully marginalised uncertainty on our parameters varies with axion mass.

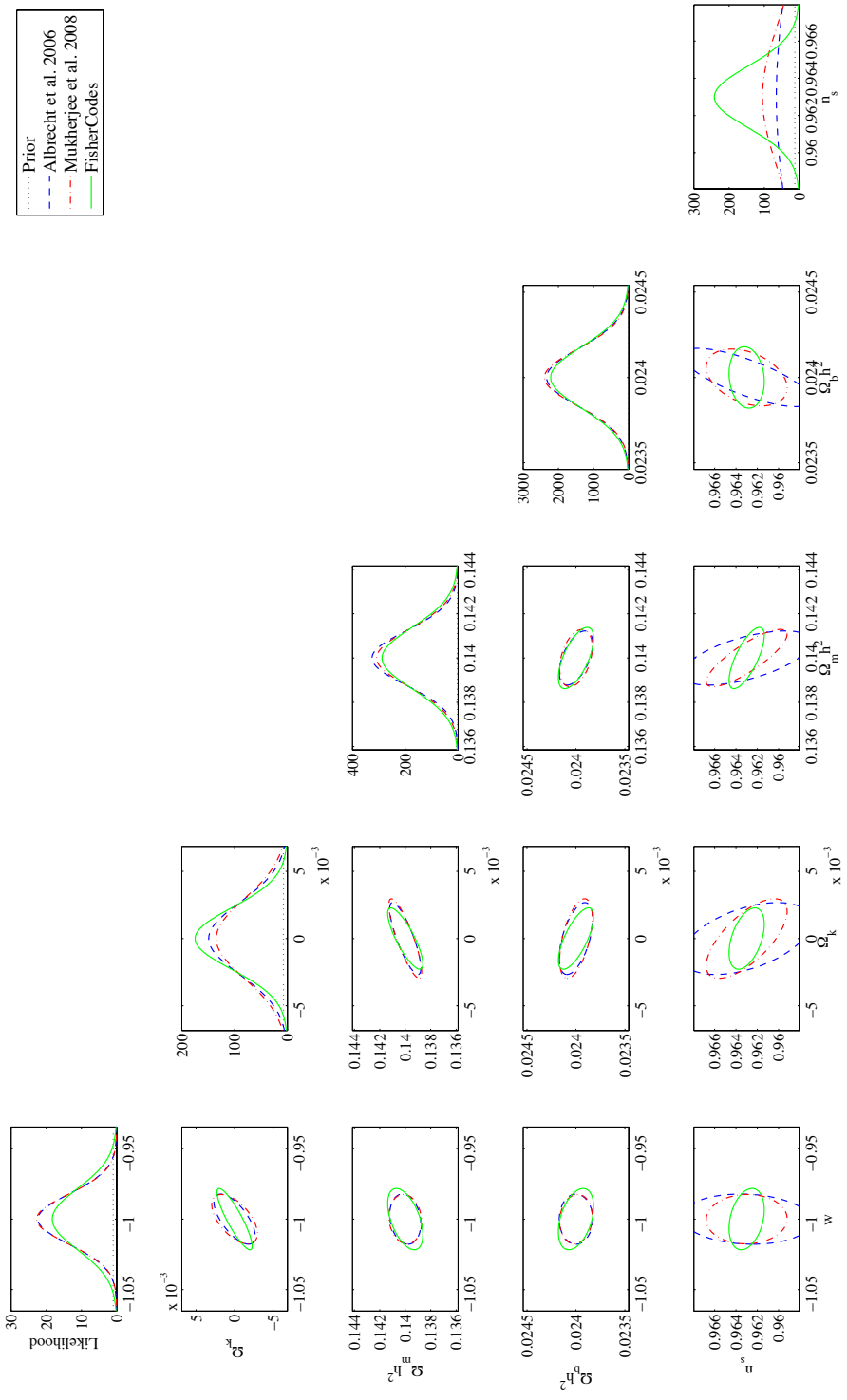

Figure 5.1: Comparing results with FisherCodes for a standard cosmology to other matrices from Mukherjee et al. [2008] and Albrecht et al. [2006]. Our forecast for n_s is the most optimistic, although all three survey models use slightly different survey settings.

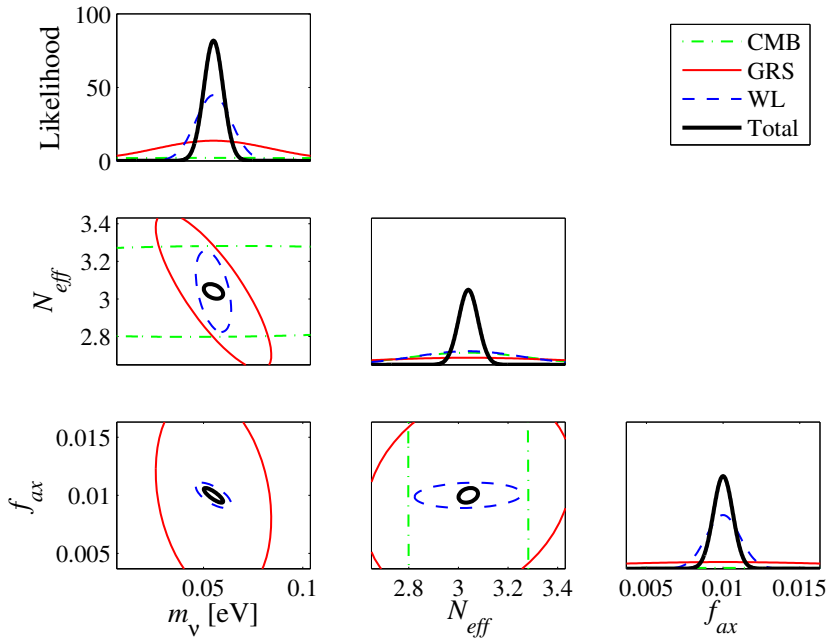

Figure 5.2: One standard deviation Fisher ellipses for m_ν, $N_{\rm eff}$ and f_{ax}. The full combined set of parameters also includes w, $\Omega_b h^2$, $\Omega_c h^2$, n_s and A_s, which have been marginalized over in this plot. Here the weak lensing forecast (blue dashed line) provides the best constraints. These forecasts are for an axion mass of $m_a = 10^{-30}\,\mathrm{eV}$.

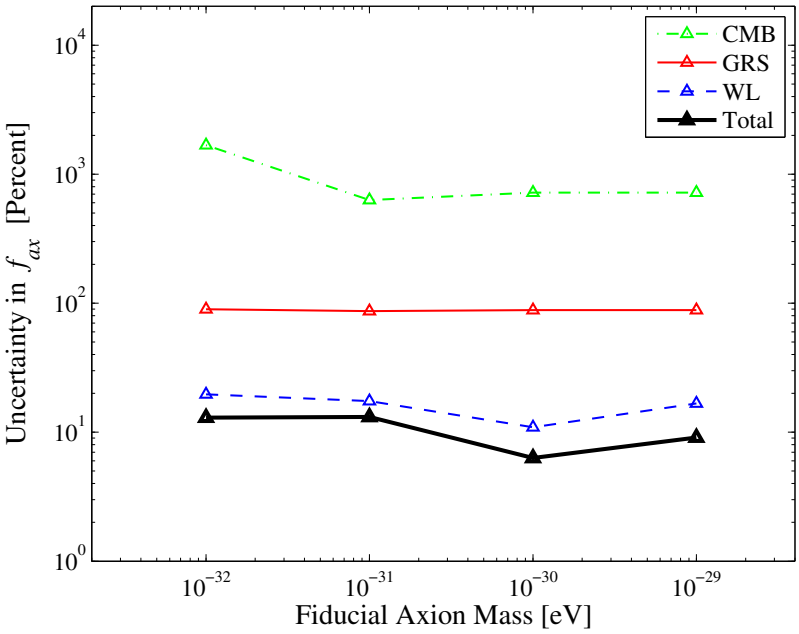

Figure 5.3: Marginalized uncertainty in f_{ax} for our three observables, evaluated for four different fiducial axion masses, for the cosmology ΛCDM+$f_{ax}+m_\nu$. The uncertainty from the galaxy redshift and weak lensing surveys does not change appreciably across the range of axion mass, whereas the uncertainty from the CMB survey decreases for higher axion masses.

We can see in Figure 5.3 that the uncertainty in f_{ax} from the galaxy redshift survey does not change appreciably with axion mass.

The improvement in the CMB measurement of f_{ax} is shown again in Figure 5.4 for the range of fiducial m_a, where we show the Fisher ellipse with $\Omega_c h^2$.These results illustrate the positive correlation between f_{ax} and $\Omega_c h^2$.

In Figure 5.5 we show the effect of having redshift information on the constraints from a galaxy survey. Although a measurement of the power spectrum at a single redshift cannot distinguish $f_{ax} = 0.01$ from $f_{ax} = 0$ at 1σ, this becomes possible when all z bins are combined, where the improvement is due to the combined constraining power of the 15 independent redshift bins, on both f_{ax}, and also on the other (marginalised) parameters.

Figure 5.6 shows the expected positive correlation between constraints on f_{ax} and constraints on n_s from the galaxy redshift survey. The constraints on $\Omega_b h^2$

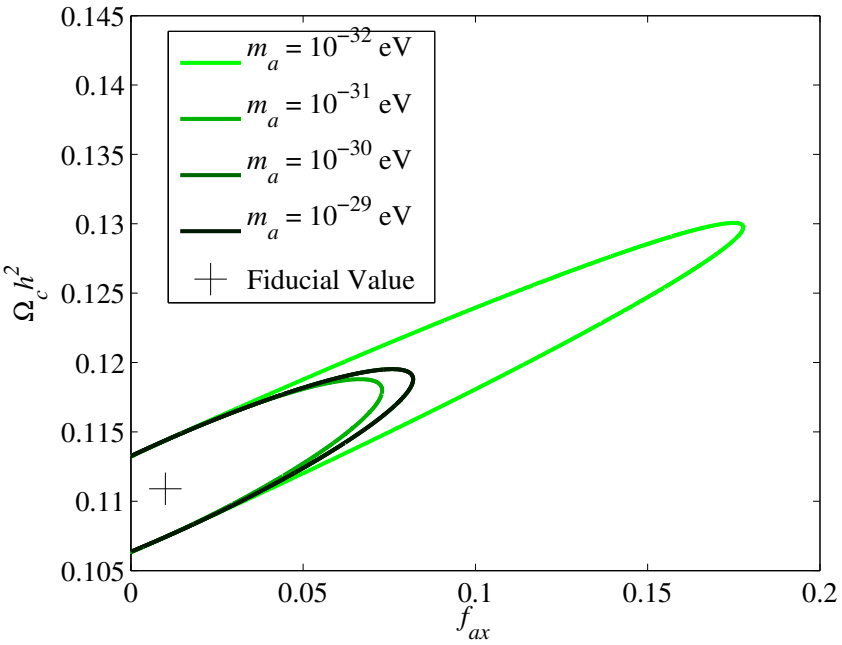

Figure 5.4: Fisher ellipses for our forecast CMB survey for parameters $\Omega_c h^2$ and f_{ax} for a range of axion mass. Note that if we fix f_{ax}, we obtain the same uncertainty on $\Omega_c h^2$ for all the different masses. Only three ellipses are visible, since we obtain the same ellipse for the $m_a = 10^{-30}$ and $m_a = 10^{-29}$ eV masses.

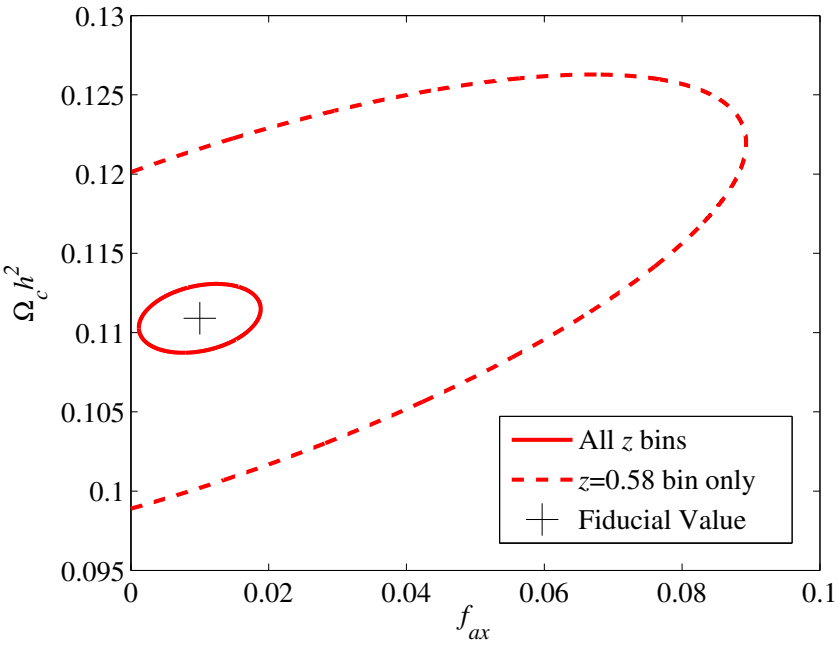

Figure 5.5: Forecasts on $\Omega_c h^2$ and f_{ax}, for the galaxy redshift survey. With one redshift bin of the survey (dashed line), the survey cannot discriminate between a cosmology with or without axions, and can only rule out $f_{ax} \lesssim 10\%$. When constraints from all 15 redshift bins are combined, detecting $f_{ax} > 0$ is just possible to 1σ. The constraints are the same for all axion masses.

and f_{ax} in Figure 5.7 show a negative correlation in the galaxy redshift survey, and small positive correlation in the weak lensing survey.

For comparison, we also considered a cosmology as before, but with massless neutrinos. The constraints on f_{ax} from all observables, along with the mass dependence, was approximately the same as without neutrinos. We finally consider an axion-free cosmology, with massive neutrinos. The Fisher ellipse for $N_{\rm eff}$ and m_ν is shown in Figure 5.8 for our different observables. Figure 5.9 illustrates the full set of uncertainties from an axion forecast.

5.2 Parametrised Modified Gravity Forecasts

In the previous section, we considered measuring neutrino and axion constituents of dark matter. In this section, we focus on dark energy, and modified gravity alternatives. We present preliminary forecast results for the Parametrised-Post-Friedman (PPF) model of Baker et al. [2011]. The model is inspired by the Parametrised-Post-Newtonian (PPN) treatment on solar scales, and uses a parametrisation of the linearly perturbed gravitational field equations.

The idea is that in General Relativity, the gravitational potential of the time-like portion of the perturbed metric, Ψ, is equal to the gravitational potential of the space-like portion of the perturbed metric, Φ, so that $\Phi - \Psi = 0$. In the PPN model, and the cosmological PPF model we consider here, the difference in the two potentials is not forced to be zero, and the difference is parametrised by $\Phi - \Psi = \zeta\Phi$, where the gravitational slip ζ is zero in General Relativity. By allowing ζ to vary with redshift, the parametrisation is a test of General Relativity at cosmological scales. The parametrisation specifies the gravitational slip and effective Newton's constant at redshift 0, 1 and 2. We thus have six additional parameters to consider, with fiducial values for General Relativity given by $\zeta_0 = 0$, $\zeta_1 = 0$, $\zeta_2 = 0$, and $G_0 = 1$, $G_1 = 1$, $G_2 = 1$. Baker et al. [2011], Zuntz et al. [2011] and Baker [2011] have developed an analysis and extended CAMB to propagate non-standard values of ζ and $G_{\rm eff}$ to power spectrum and growth rate predictions. We combine these numerical power spectrum and growth rate calculations with the galaxy redshift survey Fisher matrix code developed previously to forecast uncertainty measurements in ζ and $G_{\rm eff}$.

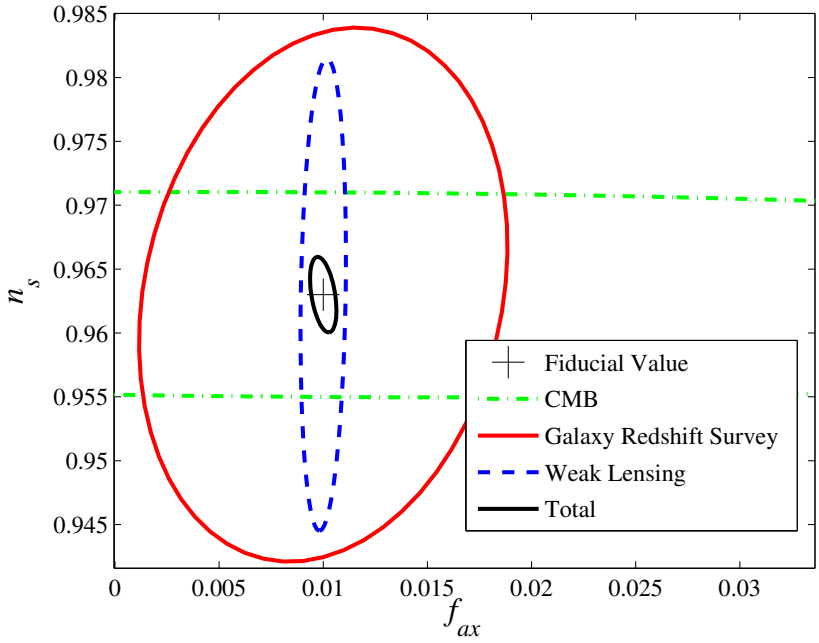

Figure 5.6: Constraints on n_s and f_{ax}, for $m_a = 10^{-30}\,\mathrm{eV}$, showing the expected positive correlation from galaxy redshift surveys. At this level of constraint, no correlation is visible in the CMB.

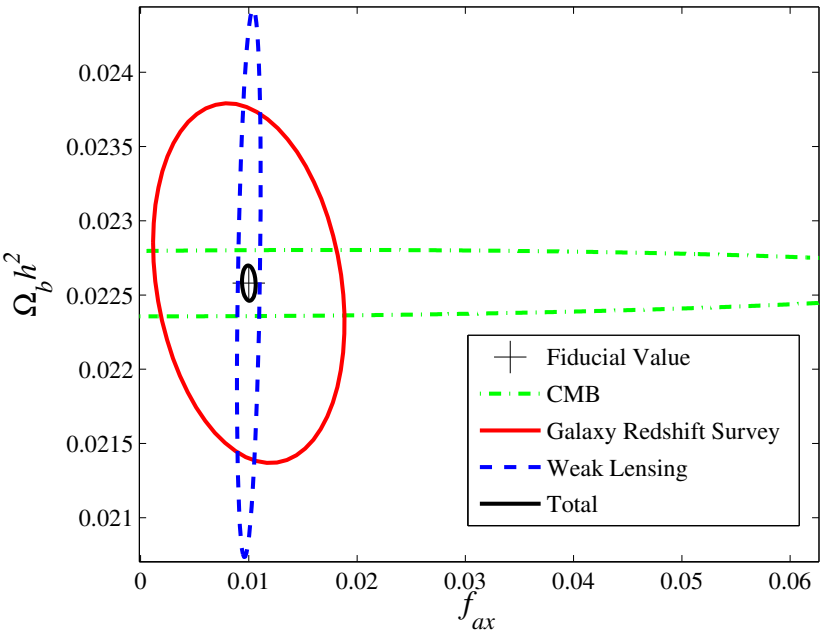

Figure 5.7: Constraints on $\Omega_b h^2$ and f_{ax}, for $m_a = 10^{-30}\,\mathrm{eV}$. We note a negative correlation from galaxy redshift surveys, whereas at this level of constraint, no correlation is visible in the CMB.

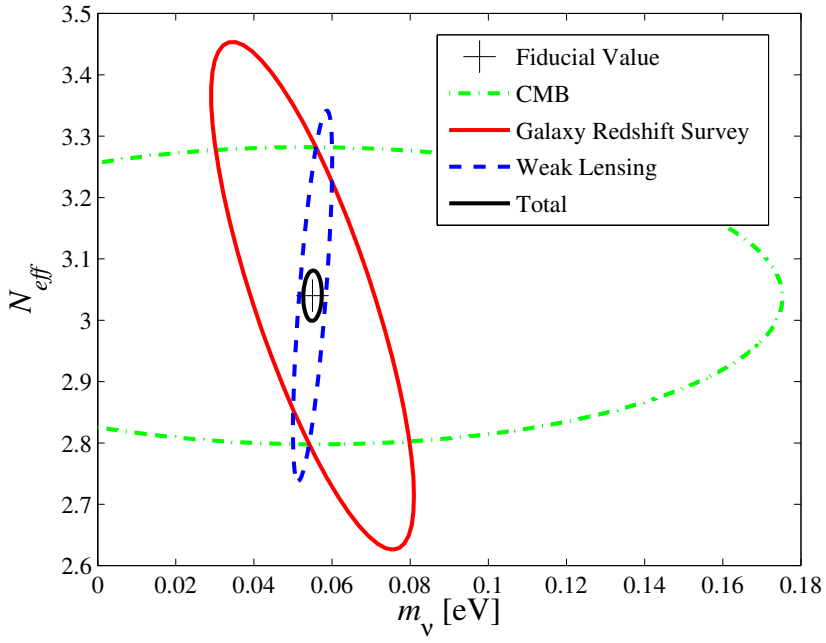

Figure 5.8: Constraints on $N_{\rm eff}$ and m_ν for the axion-free cosmology.

The model is specifically designed to parameterise a wide range of dark energy models by specifying the values of the modified gravity parameters at low redshift. As such, the model should not affect cosmology at higher redshift, such as the physics of the last scattering surface. Given the redshift range of the model, CMB lensing may be a promising observable to measure these parameters, although we do not consider this observable here. More generally, since the model takes a perturbative approach to the parametrisation, the parameters are best measured by measuring anisotropies.

In Figure 5.10, current growth rate measurements are plotted with models for different ζ and $G_{\rm eff}$. The non-fiducial models we have plotted here are already ruled out by current measurements; we have chosen to plot wide parameter values to illustrate the effects. Figure 5.11 illustrates the full set of Fisher ellipses for the Euclid survey model. The ellipses have been colour coded according to their correlation coefficient, with blue uncorrelated and red correlated (or anti-correlated). We note that at each redshift, ζ is highly correlated with the corresponding G, although the correlation is less obvious for the $z = 0$ parameter, due to the redshift

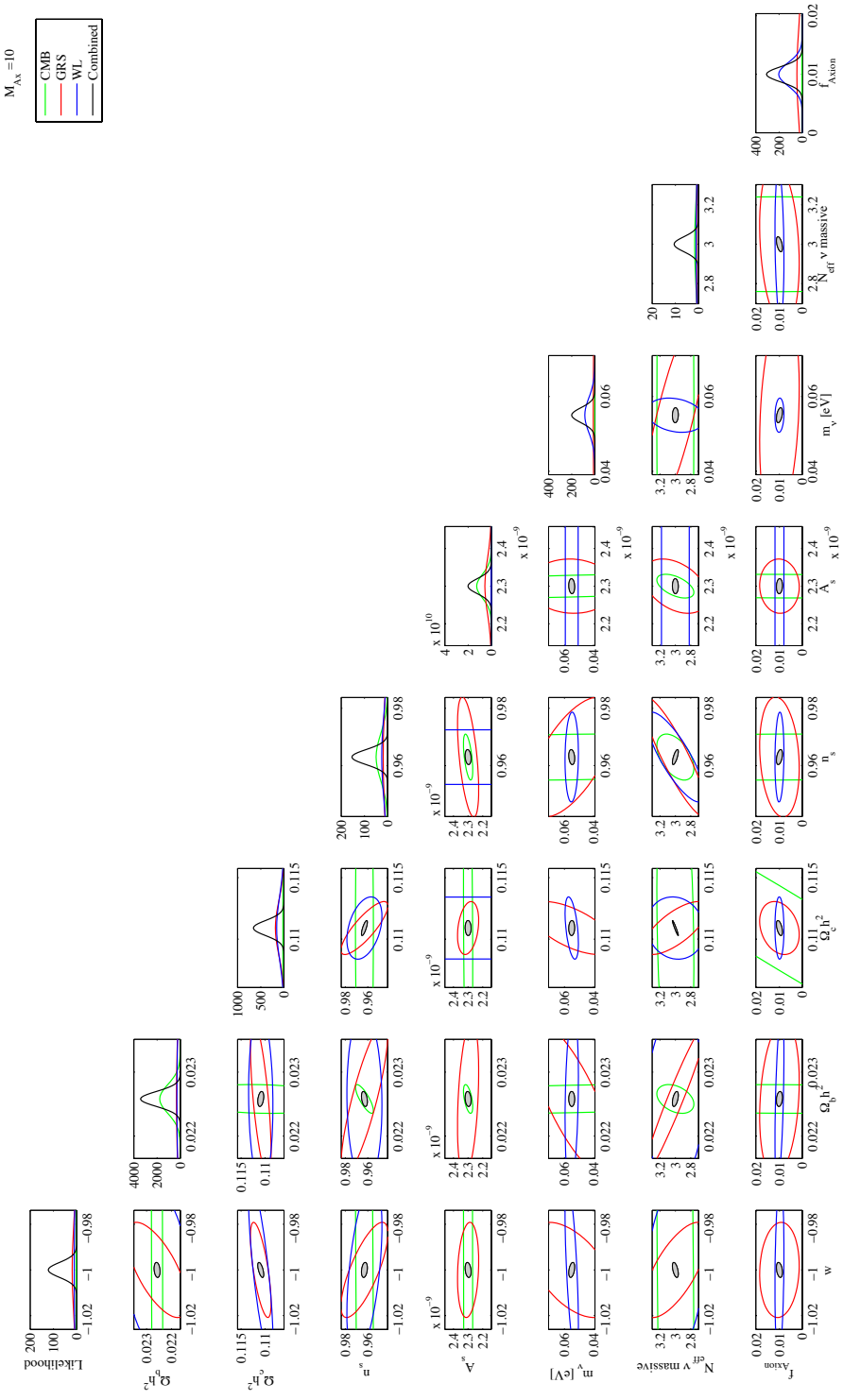

Figure 5.9: The full set of uncertainties for all the combined parameters in the lightest axion mass forecast set.

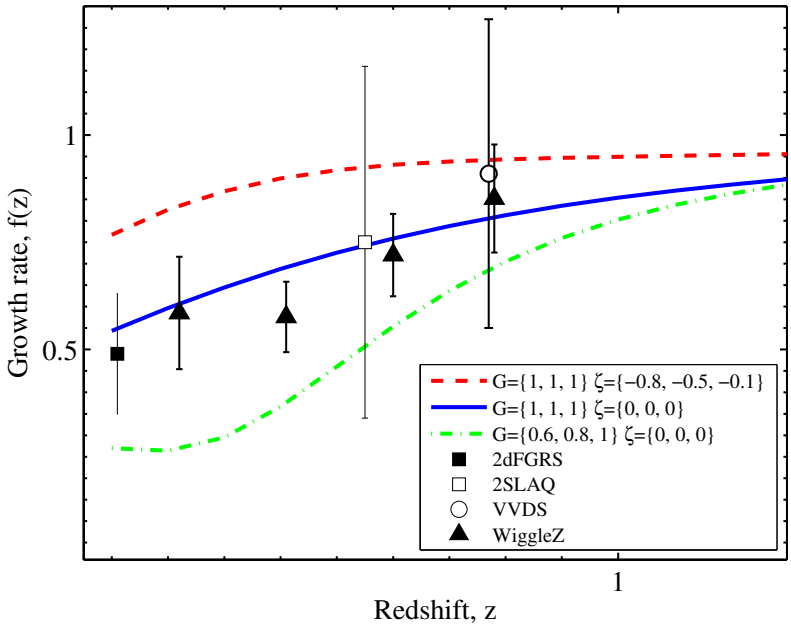

Figure 5.10: Growth rate models for various modified gravity models, plotted with current measurements.

range of the survey. Neighbouring G uncertainties are also correlated.

5.3 Discussion & Conclusions

In this chapter, we have considered using galaxy redshift surveys to precisely measure the constituents of dark matter, and test the assumptions of General Relativity at cosmological scales. For the particular case of the axion dark matter model we consider here, we find that the uncertainty on the fraction of dark matter in axions is insensitive to choice of fiducial axion mass, and, consequently, it is unlikely that is will be possible to measure the mass of any fiducial axion with upcoming cosmological surveys. However, we find that any of the three observables individually could discriminate between a non-zero axion fraction, and the combined surveys could measure f_{ax} at the percent level.

More generally, these forecasts illustrate the potential for a detailed study of the nature of dark matter with upcoming cosmological surveys, and the improve-

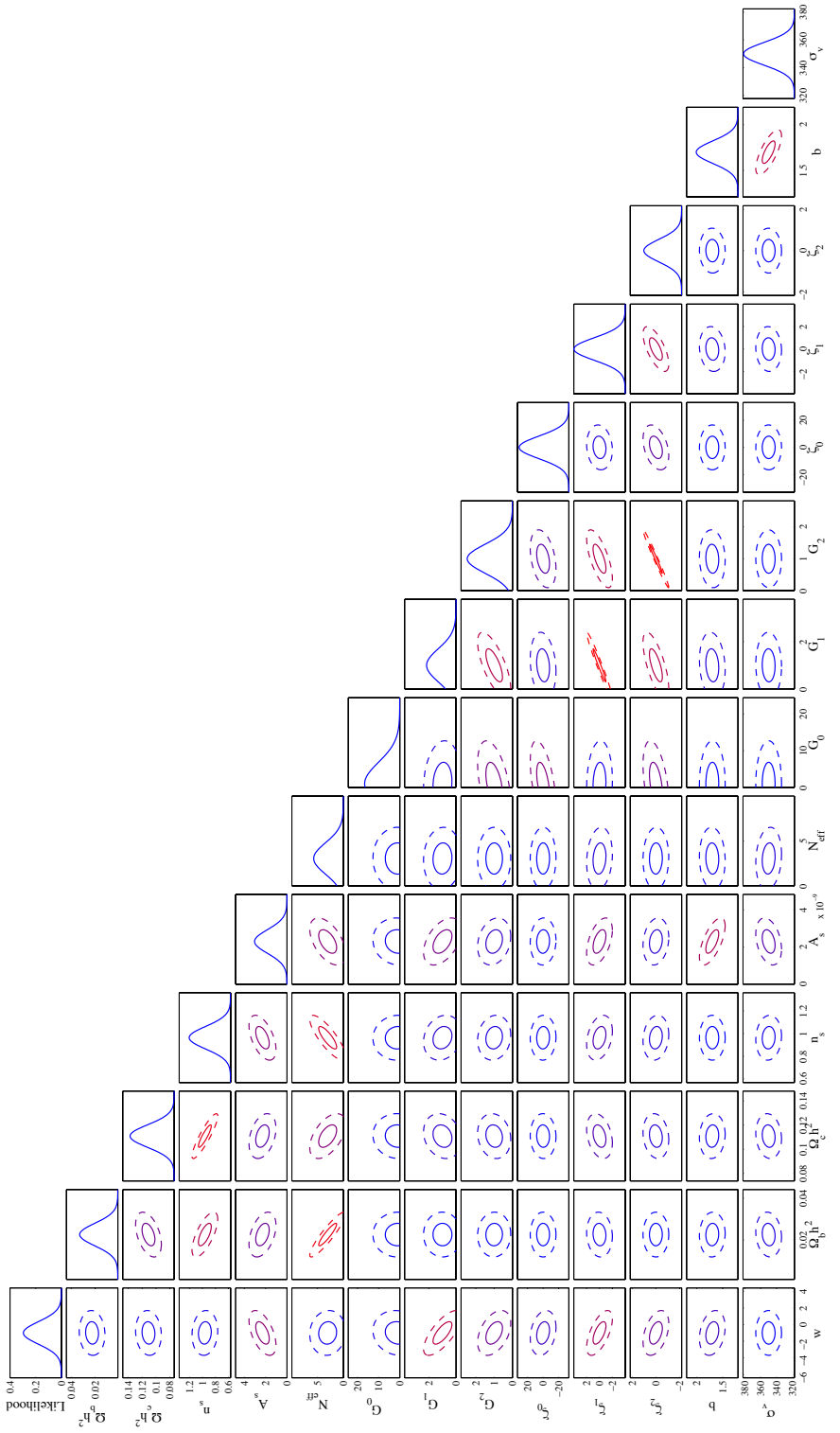

Figure 5.11: Fisher ellipses for the modified gravity forecast, for standard cosmological parameters, and six additional modified gravity parameters. Ellipses at the 1σ uncertainty level are plotted with a solid line, and are plotted with a dashed line at the 2σ level.

ment in parameter uncertainties from combined measurements. For example, in Figure 5.2, the combined uncertainty in $N_{\rm eff}$ if much smaller than than the individual uncertainties. This is because $N_{\rm eff}$ is not only highly correlated with most other parameters, but the correlation directions are different for different observables. Thus when individual Fisher matrices are combined, the combined uncertainty is significantly smaller than we might expect had we combined the marginalised uncertainty from each observable. The preliminary forecasts for the PPF model presented here include only results for a galaxy redshift survey. It is likely that these uncertainties will be significantly reduced when combined with other cosmological observables, such as weak lensing, although this remains the subject of further work.

Chapter 6

Comparing Peculiar Velocity & Redshift Forecasts

6.1 Introduction

In this chapter, we consider forecasts for future peculiar velocity surveys. By comparing with forecasts for a galaxy redshift survey, we aim to address the question: for a fixed survey, how do constraints on the power spectrum compare between a peculiar velocity survey and a redshift survey; does the additional information gained from a measurement of the peculiar velocity present a good investment of observing time? In what regimes are both methods most beneficial? We use a Fisher matrix-based approach for both types of survey.

6.2 Peculiar Velocity Fisher Matrix

As with a galaxy redshift survey, the peculiar velocity Fisher matrix is given by derivatives of the log-likelihood, weighted by the effective volume. We use the expression for the Fisher matrix from Burkey & Taylor [2004]

$$F_{ij} = \int dk \frac{\partial \ln P_{v(k)}}{\partial \Theta_i} \frac{\partial \ln P_{v(k)}}{\partial \Theta_j} V_{\text{eff}}(k) \,. \tag{6.1}$$

As before, the peculiar velocity power spectrum is related to the matter power spectrum by

$$P_v(k) = \frac{P(k)}{k^2}(aH_0 f)^2 \,, \tag{6.2}$$

and the effective volume is given by

$$V_{\rm eff}(k) = f_{\rm sky} \int dr^3 \left(\frac{n_v(r) P_v(k)}{1 + n_v(r) P_v(k)} \right)^2 : \tag{6.3}$$

where $f_{\rm sky}$ is the fraction of the sky covered by the survey. The key difference to the redshift survey Fisher matrix is that here the density is not constant across the survey volume, and is weighted by the peculiar velocity measurement uncertainty. We set the density of galaxies to be radially symmetric, with a density profile given by

$$n_g(r) \propto \exp\left(\left(\frac{r}{r_*} \right)^2 \right) \,, \tag{6.4}$$

normalised to provide the correct total number of galaxies N_g. The galaxy density is related to the 'velocity density' $n_v(r)$ by

$$n_v(r) = n_g(r) \sigma_{DI}^2 H_0^2 r^2 \,, \tag{6.5}$$

where σ_{DI} is the fractional uncertainty in the distance indicator, e.g. around 0.05 for supernovae distances, and 0.2 for Tully-Fisher measurements. Following Burkey & Taylor [2004], we use an extra exponential factor to increase the distance uncertainty at large r, so the distance uncertainty is given by s

$$\sigma_{DI} = 0.2 H_0 r \exp\left(\frac{r}{r_m} \right) \tag{6.6}$$

where r_m is a scale which characterises where the distance uncertainty increases rapidly, which we choose to be 135 h^{-1}Mpc.

The Fisher matrix can be used to forecast uncertainties in underlying parameters, and can also be used to forecast uncertainties in power spectrum bandpowers, by treating the amplitude as a parameter. For example, in the peculiar

velocity power spectrum analysis in chapters 2 and 3, the amplitude A of a fiducial power spectrum over a band range was used as a parameter, so that the power spectrum was given by $P(k) = AP_{\rm fid}(k)$. The derivative in terms of A can then be calculated analytically

$$\frac{\partial \ln AP_{\rm fid}(k)}{\partial A} = \frac{1}{A}\,. \tag{6.7}$$

Since the fiducial value of A (the value at which the Fisher matrix is evaluated) is 1, the Fisher matrix for the uncertainty in the band-powers (labeled by an index i) is given simply by integrating the effective volume

$$F_{ij} = \delta_{ij} \int_{k_i}^{k_{i+1}} dk V_{\rm eff}(k) \tag{6.8}$$

where δ_{ij} is the Kronecker delta function. The assumption here is that the uncertainties in each band-power are uncorrelated, although this is also assumed in the Feldman et al. [1994] method, as used by Tegmark [1997]. We test the band-power forecasts by reproducing the uncertainty from the band-power measurement of the COMPOSITE catalogue. We assume a characteristic depth of 33 h^{-1}Mpc, 4500 galaxies, $f_{\rm sky} = 0.8$, and a measurement uncertainty factor of 0.2. The steps in the process are illustrated in Figure 6.1. We start in the upper panel with the galaxy density as a function of radius. In the second panel, the distance uncertainty is plotted on the same scale as a function of distance. The effective volume is plotted in the third panel, and plotted in the fourth panel weighted by the volume in k space at each mode. In the fifth panel, the COMPOSITE band power uncertainties are plotted with the Fisher matrix uncertainties, so they can be easily compared to the k scales of the effective volume plots. A larger version of this plot is shown in Figure 6.2.

6.3 Comparison to Galaxy Redshift Surveys

In order to compare band power measurements with velocity surveys to redshift surveys, we use an analogous approach to forecast band-power uncertainties for a redshift survey. We use equation 8 from Seo & Eisenstein [2003] to forecast the

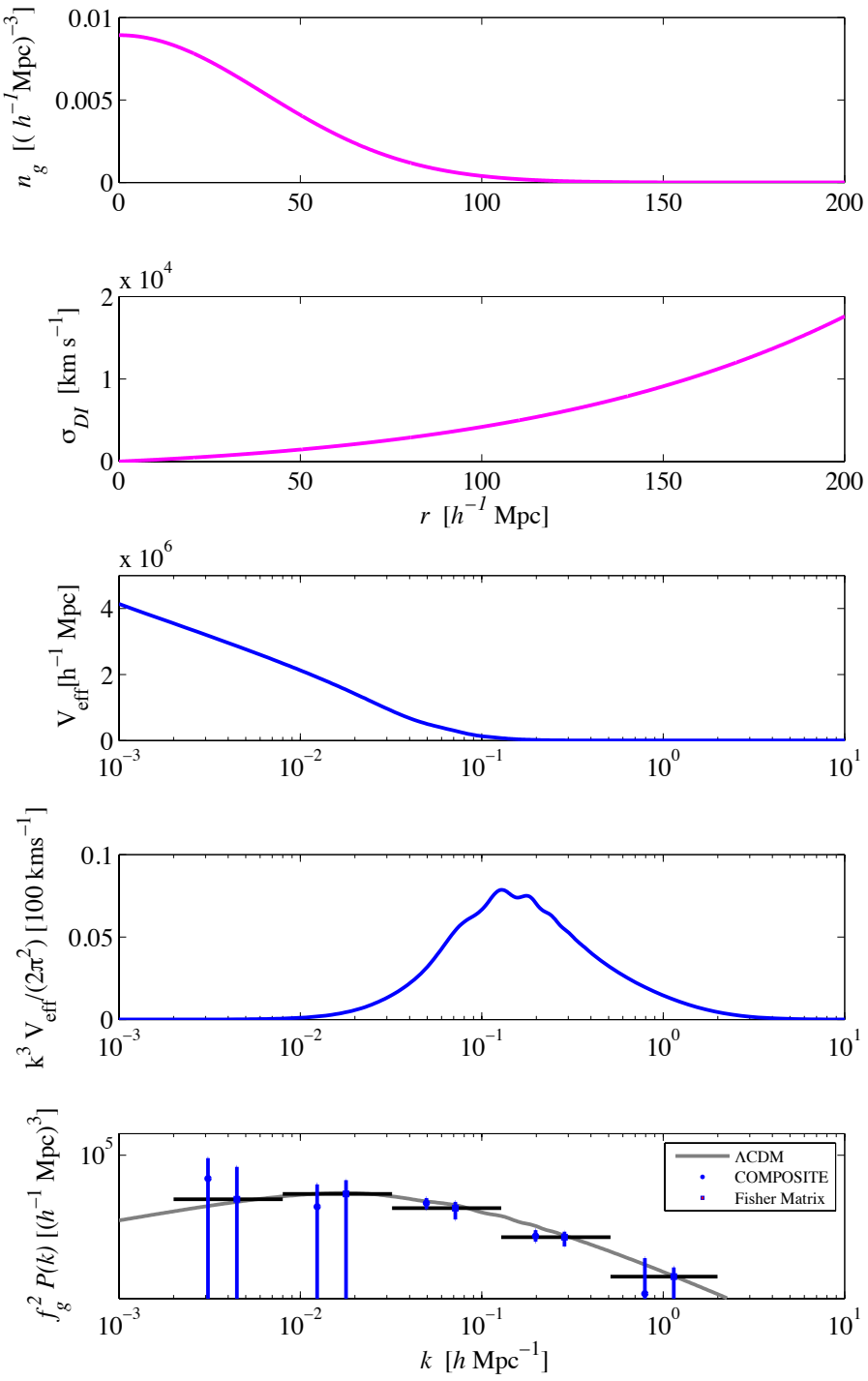

Figure 6.1: Details of the functions to calculate the uncertainty in the COMPOSITE survey with a Fisher matrix approach. A smaller version of Figure 6.2 is included in the lower panel so that the power spectrum can be directly compared to the effective volume terms.

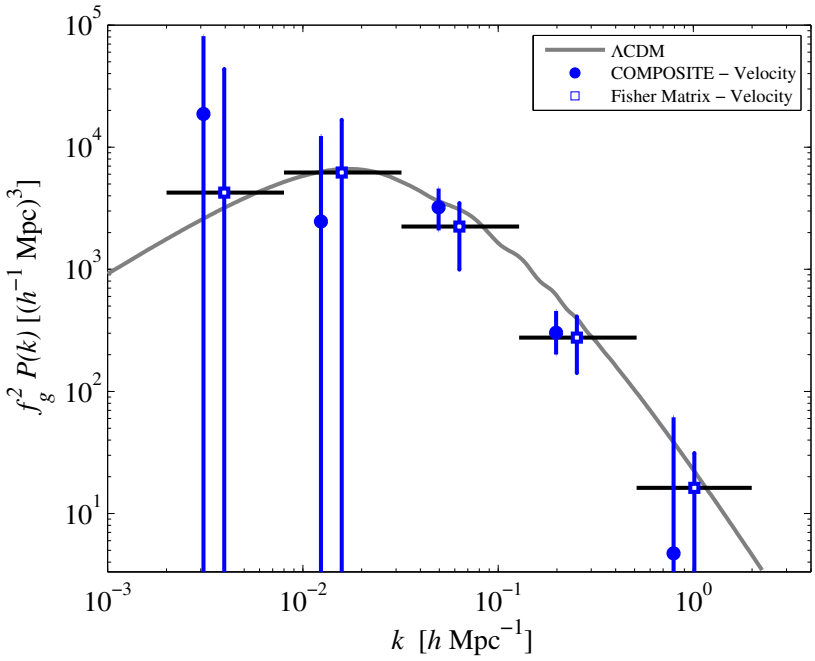

Figure 6.2: Comparing the MCMC analysis of the real COMPOSITE data to a Fisher forecast of a model of the COMPOSITE survey.

band-power uncertainty for bands evenly spaced in $\ln k$ of width $\Delta \ln k$, which, like the peculiar velocity forecast, also has an inverse square weighting on the effective volume.

$$\sigma_{P(k)} = P(k) \frac{2\pi}{\sqrt{\Delta \ln k \, k^3 V_{\rm eff}}} \tag{6.9}$$

We verify this expression by reproducing band-power uncertainties from the LRG power spectrum of Tegmark et al. [2006]. To calculate the effective volume we use a mean redshift of $z = 0.35$, a volume of $0.72h^{-3}$ Gpc, 46,748 galaxies, and a bias of 3.5. The forecast uncertainties are compared to the genuine uncertainties in Figure 6.3. The Fisher matrix error bars are slightly smaller than the genuine measurements, which may be due to the redshift distribution of the genuine LRG sample. In the Fisher matrix calculation, we have assumed a constant galaxy density throughout the survey volume, whereas in the genuine survey the density of the LRGs peaks towards the high redshift end of the survey volume, and were selected to have an optimum density distribution to minimise power spectrum uncertainty at all scales.

The forecast points are evaluated at the k value of the LRG points, and the $P(k)$ value of the fiducial power spectrum at each k. To compare the results more easily, the forecast uncertainties are plotted at the measured LRG values, with the k value slightly shifted. Evaluating the uncertainties at the measured LRG $P(k)$ values produces similar results. In Figure 6.4 the uncertainty is illustrated for three different redshift bins for the Euclid survey model.

We can now directly compare power spectrum uncertainties for a hypothetical peculiar velocity survey to the same constraints we would have obtained with only the redshifts of the survey. We start with the model used to reproduce with uncertainties in the COMPOSITE catalogue in Figure 6.2. We use the same density of galaxies and equation 6.9 to forecast the power spectrum uncertainty had we analysed the power spectrum of the redshifts of the galaxies. Since peculiar velocity measurements yield the matter power spectrum up to a factor of the growth rate squared, and redshift measurements yield the matter power spectrum up to a factor of the linear galaxy bias, we are assuming for the purpose of the comparison that these two factors are both known, so that the results can be

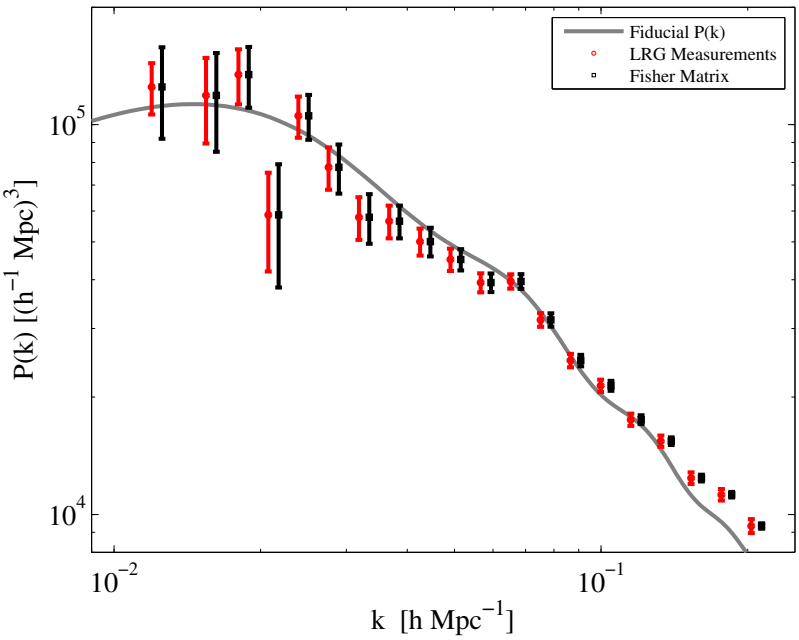

Figure 6.3: Comparing Fisher forecast uncertainties for the LRG survey to the genuine measurements from Tegmark et al. [2006].

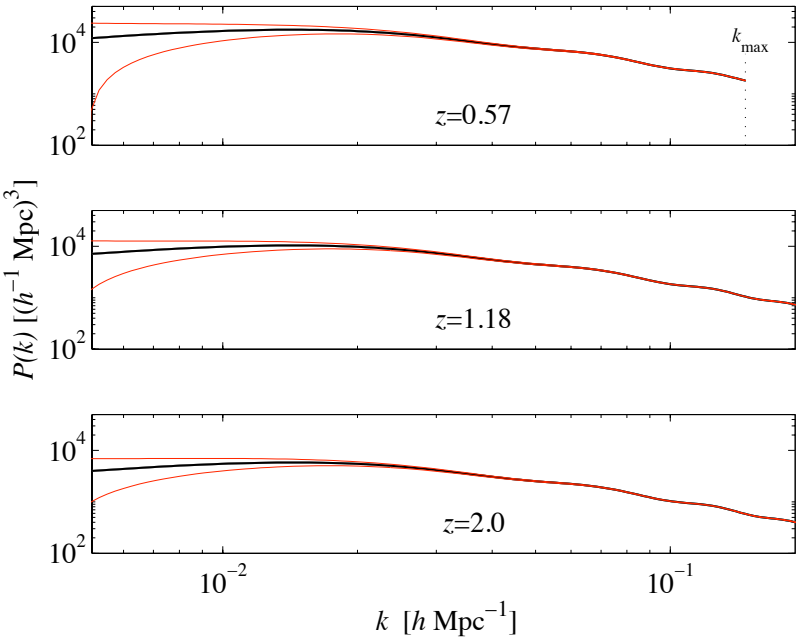

Figure 6.4: Power spectrum forecasts for the Euclid survey, in three different redshift bands.

directly compared. In practice, this amounts in to in both cases assuming that the power spectrum normalisation is known. The two results are compared in Figure 6.5.

We find that for $k > 0.5\,h^{-1}$ Mpc, the redshift survey yields significantly improved constraints than the peculiar velocity survey. However, at large scales, the upper bound on the power spectrum increases less with the velocity survey than the redshift survey. This suggests that the power spectrum measurements from the COMPOSITE survey presented in this thesis could be significantly improved by also including position information in the likelihood expression, as opposed to treating the galaxies as a random distribution of point particles tracing the velocity field. The question we now consider is: is there a regime in which a peculiar velocity survey offers significant improvements over a redshift survey. In Figure 6.6 we consider a hypothetical survey of 10^5 galaxies, and $f_{\rm sky} = 0.8$. We assume a distance uncertainty of 5%, corresponding to distances from supernovae 1A, and we have not included the additional exponential factor in the distance un-

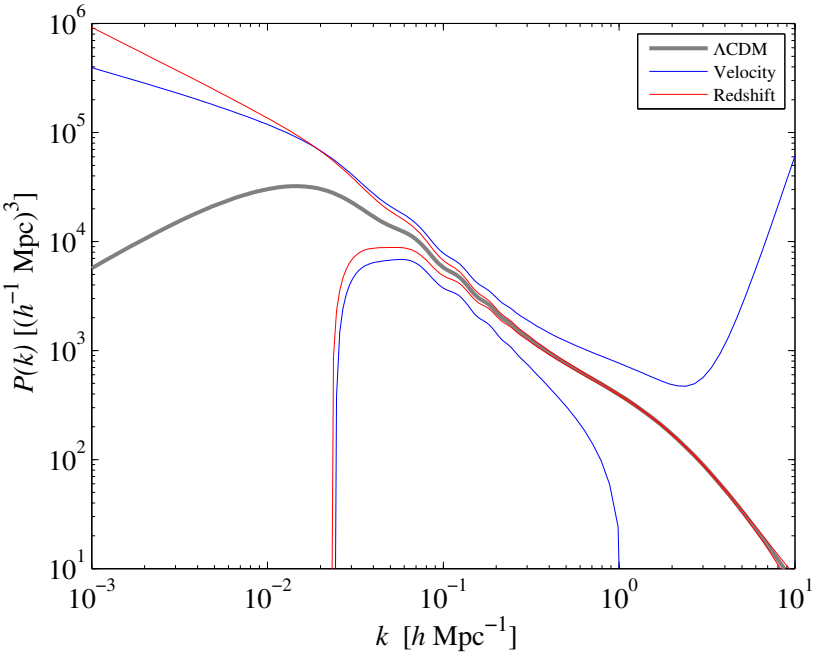

Figure 6.5: Comparing power spectrum uncertainties for a COMPOSITE-style peculiar velocity survey. We assume a band-width evenly spaced in $log - k$, of $\Delta \ln k = 1.39$, corresponding to the width used in the real power spectrum analysis.

certainty. In the three different panels are plotted power spectrum uncertainties for three different surveys, with only different r_*.

We see that the velocity survey only provides much better large scale constraints on the power spectrum for a survey depth of several hundred h^{-1} Mpc. Increasing the uncertainty on the distance indicator increases the uncertainty in the velocity survey measured power spectrum, and has no effect on the redshift measured power spectrum.

In Figure 6.7, we compare the regimes where both types of survey are most successful, in terms of the survey parameters of the depth R, number of galaxies N_g, and fractional distance uncertainty σ_{DI}. There is no need to vary the area of the survey $f_{\rm sky}$, since both redshift and velocity surveys have the same dependence, and different values of $f_{\rm sky}$ would have no effect on the relative comparison. In each subplot are contours indicating the difference in effective volume between the peculiar velocity survey and the redshift survey. Where this difference is positive the contours are plotted in blue - this indicates the range of survey parameters for which the additional peculiar velocity measurements provide a better measurement of the power spectrum at the indicated k scale than the redshift measurements alone. The red contours indicate the equivalent region for the redshift survey. The contours are drawn around 0.9, 0.1 and 0.01 of the peak value in each case. The three different rows of subplots correspond to three different values of σ_{DI}.

For all distance uncertainties and k scales, the peculiar velocity survey is most advantageous than the redshift survey for a low number of galaxies, or a high survey depth. The area of parameter space where a peculiar velocity survey presents most benefit decreases as the uncertainty on the distance measurements increases, as is most easily seen in the $k = 0.2\ h\ \mathrm{Mpc}^{-1}$ case.

6.4 Combining Surveys

We can forecast the results from a combined analysis of the redshift and peculiar velocity data simply by adding the two Fisher matrices, $F_{\rm GRS} + F_{\rm PV}$. We can also forecast the uncertainty from additionally including the cross correlation between the surveys by constructing the super matrix, consisting of the individual survey

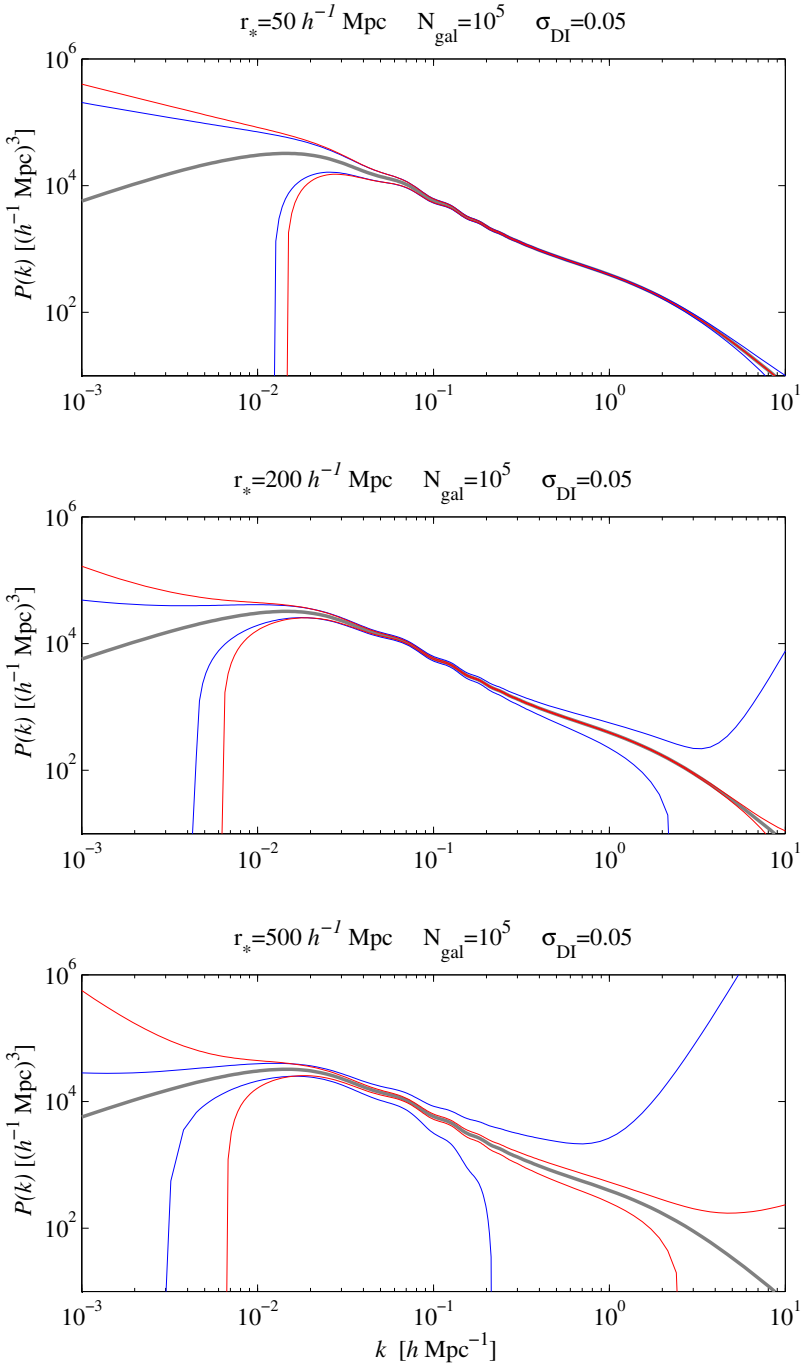

Figure 6.6: Illustrating the effect of increasing survey depth, for a fixed number of galaxies. As in Figure 6.5 the red outline is for the redshift survey, and the blue outline is for the peculiar velocity survey.

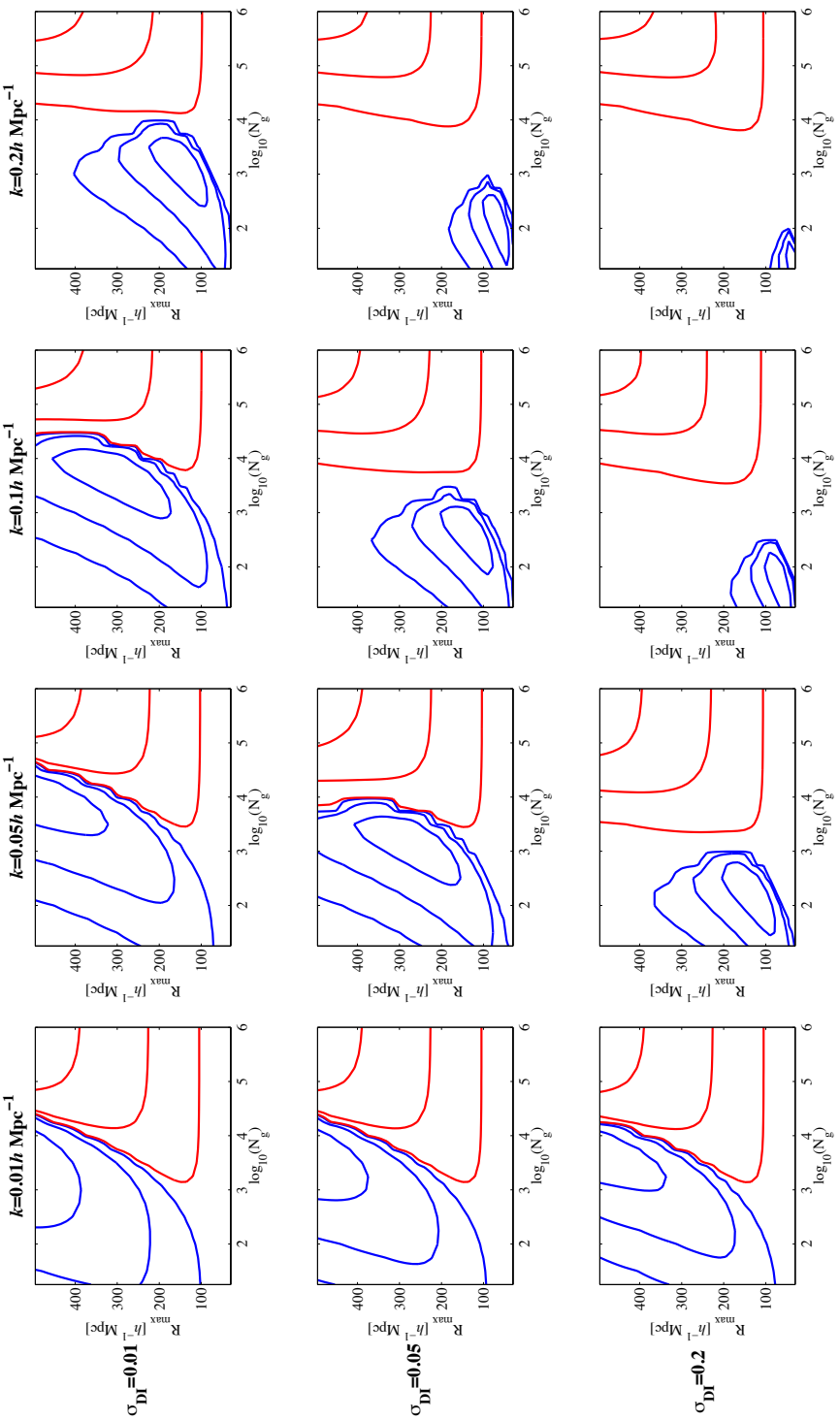

Figure 6.7: Comparing redshift (red contours) and velocity (blue contours) surveys over a range of survey size, depth, and distance uncertainty, for a range of k scales.

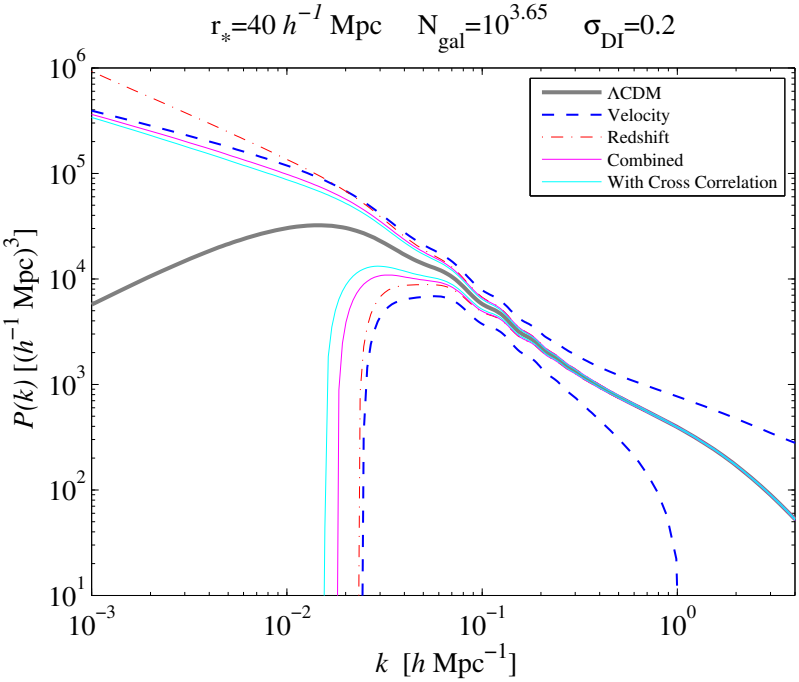

Figure 6.8: Illustrating the possibility of combining the velocity and redshift measurements, and also the cross correlation.

Fisher matrices, and the cross correlation Fisher matrix, given by

$$F_{cross,ij} = \delta_{ij}\sqrt{V_{\rm eff}^{\rm GRS}}\sqrt{V_{\rm eff}^{\rm PV}} \tag{6.10}$$

where δ_{ij} is the Kronecker delta function. The super matrix is then given by

$$\begin{pmatrix} F_{\rm GRS} & F_{\rm cross} \\ F_{\rm cross} & F_{\rm PV} \end{pmatrix}$$

Results for the combined and cross correlation are shown in Figure 6.8. Although we note an improvement with the combined surveys, and the addition of the cross correlation information, the uncertainty is driven by the redshift information. That is, the additional observing time to obtain luminosity distances, and the additional analysis to include the velocity and cross correlation information only results in a small improvement in the uncertainty in the power spectrum over the comparatively easier redshift-only approach.

6.5 Discussion & Conclusions

We find that peculiar velocity surveys will only be directly competitive with galaxy redshift surveys for a very deep peculiar velocity survey, to measure large scale fluctuations in the power spectrum. For peculiar velocity surveys less than several hundred h^{-1} Mpc deep, the (significant) additional observing effort in obtaining a luminosity distance indicator does not result in a greatly improved power spectrum measurement over a comparatively simpler redshift-only survey. Also, not including position information in the power spectrum likelihood can lead to much larger uncertainties at high k. Since very deep distance indicators are essential, supernovae surveys are likely to be most useful, as opposed to Tully-Fisher or fundamental plane surveys.

Nevertheless, peculiar velocity surveys still offer the unique advantage that the power spectrum measurements are independent of galaxy bias. The two survey methods offer independent and complimentary measurements of the power spectrum: from a redshift survey we obtain $b^2P(k)$, and from a velocity survey we obtain $f_g^2P(k)$. Thus by measuring and comparing both, we can learn about scale dependance of bias and growth.

Chapter 7

Conclusions & Future Prospects

In this thesis, we have considered the question: what can power spectrum measurements from galaxy surveys tell us about dark matter, dark energy, and our cosmological model? We have found in Chapters 2 and 3 that despite a high dipole moment, the power spectrum of the COMPOSITE peculiar velocity catalogue is in good agreement with the ΛCDM model across a wide range of scales. However, we find a large uncertainty in the band-power measurements, which agrees with the Fisher forecasts in Chapter 6, where we also note that for all but the very largest scales, galaxy redshift measurements present the most promising method for measuring the power spectrum. In Chapters 4 and 5 we have presented forecasts for future galaxy redshift surveys for a range of cosmological parameters. We have shown that it should be possible to begin to probe the constituents of dark matter with the next generation of redshift surveys. Surveys such as Euclid and BigBOSS present the prospect of a practically cosmic variance limited catalogue of galaxy redshifts out to $z \approx 2$ within the foreseeable future.

As a probe of the power spectrum, we see in Figure 6.7 the additional observing effort of obtaining a peculiar velocity measurement is only advantageous for surveys of less than around 10^4 galaxies, and is typically most useful for smaller-still surveys of a few hundred or a few thousand galaxies. With the advent of high multiplexed, fibre-fed spectrographs such as the SDSS spectrograph [Uomoto et al., 1999], the 2dF instrument [Lewis et al., 2002] and FMOS [Kimura et al., 2010], it has become much easier to obtain the redshifts of tens of thousands of galaxies, so it would appear that the future of cosmology with galaxy surveys is

with redshift measurements only, as opposed to peculiar velocity measurements.

As such, it is likely that it will become increasingly important to understand the nature of galaxy bias, since the link between the observed survey and the underlying dark universe depends entirely on this parameter. For the forecasts we have presented here, we have considered only a linear, redshift dependent bias, which is constant at all scales. In reality, the bias may well be scale dependent. Any interesting results from power spectrum measurements would be completely degenerate with a change in the bias. With the increasing survey size of current and planned surveys, the use of higher order statistics such as the three point correlation function will become increasingly important (and robust) to test the assumptions of galaxy bias, for example McBride et al. [2011]; Verde et al. [2002]. Perhaps the most promising prospect for future redshift surveys is a combined analysis with weak lensing, to produce bias independent results, as in Reyes et al. [2010].

Although purely in terms of power spectrum measurements, peculiar velocities are not competitive with redshifts, velocity measurements are still a complementary and independent cosmological probe, and there are many possibilities for improvement in future surveys. Another important distinction between the two surveys is that redshift surveys are typically motivated with power spectrum measurements as the primary science goal, whereas the luminosity distances from which we derive peculiar velocities are often as the result of surveys with other primary science goals, which makes the power spectrum results possible at no additional observing cost. Such surveys typically concern galaxy evolution, although there are several particularly interesting prospects for future peculiar velocity measurements.

Further observations and cross calibrations are continuously improving distance indicators such as Tully-Fisher (for example Davis et al. [2011]; McGaugh [2012]) and Fundamental plane measurements [Barbera et al., 2008; Hyde & Bernardi, 2009]. Senevirathne [2010] suggests that future gravitational wave detectors may be able to use 'standard sirens' of coalescing compact objects to obtain distance measurements of $\sim$100 objects with $\sigma_{DI} = 1\%$. As described in Nusser et al. [2012], very precise astrometry from the Gaia mission will allow peculiar velocities to be measured in the tangential direction. It is clear

that over the coming years there will be many new and varied peculiar velocity measurements, which in principle could yield valuable and complementary power spectrum measurements.

As illustrated in Figure 5.9, the future of measuring cosmological parameters lies in combined analysis of independent observables. Breaking degeneracies in parameter uncertainties with independent observations substantially reduces the volume of the correlated parameter space which describes the ΛCDM model. Cosmological constraints from power spectrum measurements in galaxy surveys have already substantially contributed to our picture of the ΛCDM model, and are well placed to make an impact in the next generation of cosmological surveys.

References

Abate A., Erdoğdu P., 2009, MNRAS, 400, 1541 15

Abate A., Feldman H. A., 2012, MNRAS, 419, 3482 14

Albrecht A., Bernstein G., Cahn R., Freedman W. L., Hewitt J., Hu W., Huth J., Kamionkowski M., Kolb E. W., Knox L., Mather J. C., Staggs S., Suntzeff N. B., 2006, ArXiv Astrophysics e-prints 52, 53

Anderson L., Aubourg E., Bailey S., Bizyaev D., Blanton M., Bolton A. S., Brinkmann J., Brownstein J. R., Burden A., Cuesta A. J., da Costa L. N. A., Dawson K. S., de Putter R., Eisenstein D. J., Gunn J. E., Guo H., Hamilton J.-C., Harding P., Ho S., Honscheid K., Kazin E., Kirkby D., Kneib J.-P., Labatie A., Loomis C., Lupton R. H., Malanushenko E., Malanushenko V., Mandelbaum R., Manera M., Maraston C., McBride C. K., Mehta K. T., Mena O., Montesano F., Muna D., Nichol R. C., Nuza S. E., Olmstead M. D., Oravetz D., Padmanabhan N., Palanque-Delabrouille N., Pan K., Parejko J., Paris I., Percival W. J., Petitjean P., Prada F., Reid B., Roe N. A., Ross A. J., Ross N. P., Samushia L., Sanchez A. G., Schneider D. J. S. D. P., Scoccola C. G., Seo H.-J., Sheldon E. S., Simmons A., Skibba R. A., Strauss M. A., Swanson M. E. C., Thomas D., Tinker J. L., Tojeiro R., Vargas Magana M., Verde L., Wagner C., Wake D. A., Weaver B. A., Weinberg D. H., White M., Xu X., Yeche C., Zehavi I., Zhao G.-B., 2012, ArXiv e-prints 37

Ayaita Y., Weber M., Wetterich C., 2009, ArXiv e-prints 15

Baker T., 2011, ArXiv e-prints ii, 59

Baker T., Ferreira P. G., Skordis C., Zuntz J., 2011, Phys. Rev. D, 84, 124018 57, 59

Balcells M., Benn C. R., Carter D., Dalton G. B., Trager S. C., Feltzing S., Verheijen M. A. W., Jarvis M., Percival W., Abrams D. C., Agocs T., Brown A. G. A., Cano D., Evans C., Helmi A., Lewis I. J., McLure R., Peletier R. F., Pérez-Fournon I., Sharples R. M., Tosh I. A. J., Trujillo I., Walton N., Westhall K. B., 2010, in Society of Photo-Optical Instrumentation Engineers (SPIE) Conference Series, Vol. 7735, Society of Photo-Optical Instrumentation Engineers (SPIE) Conference Series 38

Barbera F. L., Busarello G., Merluzzi P., de la Rosa I. G., Coppola G., Haines C. P., 2008, The Astrophysical Journal, 689, 913 75

Bassett B. A., Fantaye Y., Hlozek R., Kotze J., 2009, ArXiv e-prints ii, 38

—, 2011, International Journal of Modern Physics D, 20, 2559 41

Blake C., Brough S., Colless M., Couch W., Croom S., Davis T., Drinkwater M. J., Forster K., Glazebrook K., Jelliffe B., Jurek R. J., Li I.-h., Madore B., Martin C., Pimbblet K., Poole G. B., Pracy M., Sharp R., Wisnioski E., Woods D., Wyder T., 2010, Monthly Notices of the Royal Astronomical Society, 406, 803 7, 38, 47

Blake C., Brough S., Colless M., Couch W., Croom S., Davis T., Drinkwater M. J., Forster K., Glazebrook K., Jelliffe B., Jurek R. J., Li I.-H., Madore B., Martin C., Pimbblet K., Poole G. B., Pracy M., Sharp R., Wisnioski E., Woods D., Wyder T., 2010, MNRAS, 406, 803 14

Blake C., Kazin E. A., Beutler F., Davis T. M., Parkinson D., Brough S., Colless M., Contreras C., Couch W., Croom S., Croton D., Drinkwater M. J., Forster K., Gilbank D., Gladders M., Glazebrook K., Jelliffe B., Jurek R. J., Li I.-H., Madore B., Martin D. C., Pimbblet K., Poole G. B., Pracy M., Sharp R., Wisnioski E., Woods D., Wyder T. K., Yee H. K. C., 2011, MNRAS, 418, 1707 37

Blake C., Parkinson D., Bassett B., Glazebrook K., Kunz M., Nichol R. C., 2006, MNRAS, 365, 255 38

Burkey D., Taylor A. N., 2004, MNRAS, 347, 255 64, 65

Clifton T., Ferreira P. G., Padilla A., Skordis C., 2012, Phys. Rep., 513, 1 5

Coe D., 2009, ArXiv e-prints 41

Cole S., Percival W. J., Peacock J. A., Norberg P., Baugh C. M., Frenk C. S., Baldry I., Bland-Hawthorn J., Bridges T., Cannon R., Colless M., Collins C., Couch W., Cross N. J. G., Dalton G., Eke V. R., De Propris R., Driver S. P., Efstathiou G., Ellis R. S., Glazebrook K., Jackson C., Jenkins A., Lahav O., Lewis I., Lumsden S., Maddox S., Madgwick D., Peterson B. A., Sutherland W., Taylor K., 2005, MNRAS, 362, 505 3, 14

Coles P. P., Lucchin F., 1995, Cosmology: The Origin and Evolution of Cosmic Structure. John Wiley & Sons 5

da Ângela J., Shanks T., Croom S. M., Weilbacher P., Brunner R. J., Couch W. J., Miller L., Myers A. D., Nichol R. C., Pimbblet K. A., de Propris R., Richards G. T., Ross N. P., Schneider D. P., Wake D., 2008, MNRAS, 383, 565 7, 38

da Costa L. N., Bernardi M., Alonso M. V., Wegner G., Willmer C. N. A., Pellegrini P. S., Maia M. A. G., Zaroubi S., 2000, ApJL, 537, L81 18, 22

Das S., 2011, Fishercodes ii, 52

Davis T. A., Bureau M., Young L. M., Alatalo K., Blitz L., Cappellari M., Scott N., Bois M., Bournaud F., Davies R. L., de Zeeuw P. T., Emsellem E., Khochfar S., Krajnović D., Kuntschner H., Lablanche P.-Y., McDermid R. M., Morganti R., Naab T., Oosterloo T., Sarzi M., Serra P., Weijmans A.-M., 2011, MNRAS, 414, 968 75

Dekel A., Rees M. J., 1994, APJL, 422, L1 14

Dodelson S., 2003, Modern Cosmology. Academic Press 1, 41

Dressler A., Lynden-Bell D., Burstein D., Davies R. L., Faber S. M., Terlevich R., Wegner G., 1987, ApJ, 313, 42 13, 14

Dvali G., Gabadadze G., Porrati M., 2000, Physics Letters B, 485, 208 6, 47

Efstathiou G., Sutherland W. J., Maddox S. J., 1990, Nature, 348, 705 3

Eisenstein D. J., Zehavi I., Hogg D. W., Scoccimarro R., Blanton M. R., Nichol R. C., Scranton R., Seo H.-J., Tegmark M., Zheng Z., Anderson S. F., Annis J., Bahcall N., Brinkmann J., Burles S., Castander F. J., Connolly A., Csabai I., Doi M., Fukugita M., Frieman J. A., Glazebrook K., Gunn J. E., Hendry J. S., Hennessy G., Ivezić Z., Kent S., Knapp G. R., Lin H., Loh Y.-S., Lupton R. H., Margon B., McKay T. A., Meiksin A., Munn J. A., Pope A., Richmond M. W., Schlegel D., Schneider D. P., Shimasaku K., Stoughton C., Strauss M. A., SubbaRao M., Szalay A. S., Szapudi I., Tucker D. L., Yanny B., York D. G., 2005, ApJ, 633, 560 37

Etherington I. M. H., 1933, Philosophical Magazine, 15, 761 3

Faber S. M., Jackson R. E., 1976, APJ, 204, 668 14

Feldman H. A., Kaiser N., Peacock J. A., 1994, ApJ, 426, 23 65

Feldman H. A., Watkins R., Hudson M. J., 2010, MNRAS, 407, 2328 ii, 14, 16, 17, 18, 22, 33, 34, 35

Gong Y., 2008, PRD, 78, 123010 5

Guth A. H., 1981, PRD, 23, 347 3

Guzzo L., Pierleoni M., Meneux B., Branchini E., Le Fèvre O., Marinoni C., Garilli B., Blaizot J., De Lucia G., Pollo A., et al., 2008, Nature, 451, 541 7, 38, 41, 42, 47

Hill G. J., Gebhardt K., Komatsu E., Drory N., MacQueen P. J., Adams J., Blanc G. A., Koehler R., Rafal M., Roth M. M., Kelz A., Gronwall C., Ciardullo R., Schneider D. P., 2008, in Astronomical Society of the Pacific Conference Series, Vol. 399, Panoramic Views of Galaxy Formation and Evolution, Kodama T., Yamada T., Aoki K., eds., p. 115 38

Hlozek R., Dunkley J., Addison G., Appel J. W., Bond J. R., Sofia Carvalho C., Das S., Devlin M. J., Dünner R., Essinger-Hileman T., Fowler J. W., Gallardo P., Hajian A., Halpern M., Hasselfield M., Hilton M., Hincks A. D., Hughes J. P., Irwin K. D., Klein J., Kosowsky A., Marriage T. A., Marsden D., Menanteau F., Moodley K., Niemack M. D., Nolta M. R., Page L. A., Parker L., Partridge B., Rojas F., Sehgal N., Sherwin B., Sievers J., Spergel D. N., Staggs S. T., Swetz D. S., Switzer E. R., Thornton R., Wollack E., 2012, ApJ, 749, 90 15

Hogg D. W., 1999, ArXiv Astrophysics e-prints 38

Hubble E., 1929, Proc Natl Acad Sci U S A., 15, 168 1

Hudson M. J., Ebeling H., 1997, ApJ, 479, 621 13

Hudson M. J., Smith R. J., Lucey J. R., Branchini E., 2004, MNRAS, 352, 61 14, 15, 18, 22

Huterer D., Turner M. S., 2001, PRD, 64, 123527 3

Hyde J. B., Bernardi M., 2009, MNRAS, 396, 1171 75

Jaffe A. H., Kaiser N., 1995, ApJ, 455, 26 14, 15, 16, 17

Kaiser N., 1987, MNRAS, 227, 1 8

Kashlinsky A., Atrio-Barandela F., Ebeling H., Edge A., Kocevski D., 2010, ApJL, 712, L81 14, 15

Khoury J., Wyman M., 2009, PRD, 80, 064023 15

Kimura M., Maihara T., Iwamuro F., Akiyama M., Tamura N., Dalton G. B., Takato N., Tait P., Ohta K., Eto S., Mochida D., Elms B., Kawate K., Kurakami T., Moritani Y., Noumaru J., Ohshima N., Sumiyoshi M., Yabe K., Brzeski J., Farrell T., Frost G., Gillingham P. R., Haynes R., Moore A. M., Muller R., Smedley S., Smith G., Bonfield D. G., Brooks C. B., Holmes A. R., Lake E. C., Lee H., Lewis I. J., Froud T. R., Tosh I. A., Woodhouse G. F., Blackburn C., Dipper N., Murray G., Sharples R., Robertson D. J., 2010, ArXiv e-prints 38, 74

Kofman L. A., Gnedin N. Y., Bahcall N. A., 1993, ApJ, 413, 1 3

Kolatt T., Dekel A., 1995, ArXiv Astrophysics e-prints 17

—, 1997, ApJ, 479, 592 15

Kolatt T., Dekel A., Ganon G., Willick J. A., 1996, ApJ, 458, 419 15, 22

Landy S. D., Szalay A. S., 1993, ApJ, 412, 64 8

Larson D., Dunkley J., Hinshaw G., Komatsu E., Nolta M. R., Bennett C. L., Gold B., Halpern M., Hill R. S., Jarosik N., Kogut A., Limon M., Meyer S. S., Odegard N., Page L., Smith K. M., Spergel D. N., Tucker G. S., Weiland J. L., Wollack E., Wright E. L., 2011, ApJs, 192, 16 2, 15

Lauer T. R., Postman M., 1994, ApJ, 425, 418 13

Laureijs R., Amiaux J., Arduini S., Augueres J. ., Brinchmann J., Cole R., Cropper M., Dabin C., Duvet L., Ealet A., et al., 2011, ArXiv e-prints 38

Lewis A., Challinor A., Lasenby A., 2000, APJ, 538, 473 ii, 9

Lewis I. J., Cannon R. D., Taylor K., Glazebrook K., Bailey J. A., Baldry I. K., Barton J. R., Bridges T. J., Dalton G. B., Farrell T. J., Gray P. M., Lankshear A., McCowage C., Parry I. R., Sharples R. M., Shortridge K., Smith G. A., Stevenson J., Straede J. O., Waller L. G., Whittard J. D., Wilcox J. K., Willis K. C., 2002, MNRAS, 333, 279 74

Liddle A., 2003, An Introduction to Modern Cosmology. Wiley 1

Linder E. V., Huterer D., 2005, PRD, 72, 043509 3

Ma Y.-Z., Gordon C., Feldman H. A., 2010, ArXiv e-prints 14, 15, 16, 21, 28, 33, 35

Macaulay E., Feldman H., Ferreira P. G., Hudson M. J., Watkins R., 2011, MNRAS, 414, 621 ii

Macaulay E., Feldman H. A., Ferreira P. G., Jaffe A. H., Agarwal S., Hudson M. J., Watkins R., 2012, MNRAS, 425, 1709 ii

Marsh D. J. E., 2011, PRD, 83, 123526 51

Marsh D. J. E., Ferreira P. G., 2010, PRD, 82, 103528 51

Marsh D. J. E., Macaulay E., Trebitsch M., Ferreira P. G., 2012, PRD, 85, 103514 ii

Masters K. L., Springob C. M., Haynes M. P., Giovanelli R., 2006, ApJ, 653, 861 18, 22

McBride C. K., Connolly A. J., Gardner J. P., Scranton R., Scoccimarro R., Berlind A. A., Marn F., Schneider D. P., 2011, The Astrophysical Journal, 739, 85 74

McGaugh S. S., 2012, AJ, 143, 40 75

Mersini-Houghton L., Holman R., 2009, JCAP, 2, 6 15

Mukherjee P., Kunz M., Parkinson D., Wang Y., 2008, PRD, 78, 083529 48, 52, 53

Nusser A., Branchini E., Davis M., 2012, ArXiv e-prints 75

Nusser A., Davis M., 2011, ApJ, 736, 93 14, 35

Nusser A., Dekel A., 1993, ApJ, 405, 437 14

Palle D., 2010, European Physical Journal C, 69, 581 15

Peacock J. A., Cole S., Norberg P., Baugh C. M., Bland-Hawthorn J., Bridges T., Cannon R. D., Colless M., Collins C., Couch W., Dalton G., Deeley K., De Propris R., Driver S. P., Efstathiou G., Ellis R. S., Frenk C. S., Glazebrook K., Jackson C., Lahav O., Lewis I., Lumsden S., Maddox S., Percival W. J., Peterson B. A., Price I., Sutherland W., Taylor K., 2001, Nature, 410, 169 3, 7, 37, 47

Peebles P. J. E., 1993, Principles of Physical Cosmology. Princeton University Press 1, 15

Peebles P. J. E., Yu J. T., 1970, ApJ, 162, 815 37

Percival W. J., Baugh C. M., Bland-Hawthorn J., Bridges T., Cannon R., Cole S., Colless M., Collins C., Couch W., Dalton G., De Propris R., Driver S. P., Efstathiou G., Ellis R. S., Frenk C. S., Glazebrook K., Jackson C., Lahav O., Lewis I., Lumsden S., Maddox S., Moody S., Norberg P., Peacock J. A., Peterson B. A., Sutherland W., Taylor K., 2001, MNRAS, 327, 1297 3, 37

Percival W. J., Cole S., Eisenstein D. J., Nichol R. C., Peacock J. A., Pope A. C., Szalay A. S., 2007a, MNRAS, 381, 1053 3, 37

Percival W. J., Nichol R. C., Eisenstein D. J., Frieman J. A., Fukugita M., Loveday J., Pope A. C., Schneider D. P., Szalay A. S., Tegmark M., Vogeley M. S., Weinberg D. H., Zehavi I., Bahcall N. A., Brinkmann J., Connolly A. J., Meiksin A., 2007b, ApJ, 657, 645 3

Percival W. J., Reid B. A., Eisenstein D. J., Bahcall N. A., Budavari T., Frieman J. A., Fukugita M., Gunn J. E., Ivezić Ž., Knapp G. R., Kron R. G., Loveday J., Lupton R. H., McKay T. A., Meiksin A., Nichol R. C., Pope A. C., Schlegel D. J., Schneider D. P., Spergel D. N., Stoughton C., Strauss M. A., Szalay A. S., Tegmark M., Vogeley M. S., Weinberg D. H., York D. G., Zehavi I., 2010, MNRAS, 401, 2148 37

Perlmutter S., Aldering G., Goldhaber G., Knop R. A., Nugent P., Castro P. G., Deustua S., Fabbro S., Goobar A., Groom D. E., Hook I. M., Kim A. G., Kim M. Y., Lee J. C., Nunes N. J., Pain R., Pennypacker C. R., Quimby R., Lidman C., Ellis R. S., Irwin M., McMahon R. G., Ruiz-Lapuente P., Walton N., Schaefer B., Boyle B. J., Filippenko A. V., Matheson T., Fruchter A. S., Panagia N., Newberg H. J. M., Couch W. J., The Supernova Cosmology Project, 1999, ApJ, 517, 565 2, 3

Postman M., Lauer T. R., 1995, APJ, 440, 28 13

Potter W. J., Chongchitnan S., 2011, JCAP, 9, 5 15

Reid B. A., Percival W. J., Eisenstein D. J., Verde L., Spergel D. N., Skibba R. A., Bahcall N. A., Budavari T., Frieman J. A., Fukugita M., Gott J. R., Gunn J. E., Ivezić Ž., Knapp G. R., Kron R. G., Lupton R. H., McKay T. A.,

Meiksin A., Nichol R. C., Pope A. C., Schlegel D. J., Schneider D. P., Stoughton C., Strauss M. A., Szalay A. S., Tegmark M., Vogeley M. S., Weinberg D. H., York D. G., Zehavi I., 2010, MNRAS, 404, 60 14

Reid B. A., Samushia L., White M., Percival W. J., Manera M., Padmanabhan N., Ross A. J., Sánchez A. G., Bailey S., Bizyaev D., Bolton A. S., Brewington H., Brinkmann J., Brownstein J. R., Cuesta A. J., Eisenstein D. J., Gunn J. E., Honscheid K., Malanushenko E., Malanushenko V., Maraston C., McBride C. K., Muna D., Nichol R. C., Oravetz D., Pan K., de Putter R., Roe N. A., Ross N. P., Schlegel D. J., Schneider D. P., Seo H.-J., Shelden A., Sheldon E. S., Simmons A., Skibba R. A., Snedden S., Swanson M. E. C., Thomas D., Tinker J., Tojeiro R., Verde L., Wake D. A., Weaver B. A., Weinberg D. H., Zehavi I., Zhao G.-B., 2012, ArXiv e-prints 7, 38

Reyes R., Mandelbaum R., Seljak U., Baldauf T., Gunn J. E., Lombriser L., Smith R. E., 2010, Nature, 464, 256 3, 74

Riess A. G., Filippenko A. V., Challis P., Clocchiatti A., Diercks A., Garnavich P. M., Gilliland R. L., Hogan C. J., Jha S., Kirshner R. P., Leibundgut B., Phillips M. M., Reiss D., Schmidt B. P., Schommer R. A., Smith R. C., Spyromilio J., Stubbs C., Suntzeff N. B., Tonry J., 1998, AJ, 116, 1009 2, 3

Ross A. J., Ho S., Cuesta A. J., Tojeiro R., Percival W. J., Wake D., Masters K. L., Nichol R. C., Myers A. D., de Simoni F., Seo H. J., Hernndez-Monteagudo C., Crittenden R., Blanton M., Brinkmann J., da Costa L. A. N., Guo H., Kazin E., Maia M. A. G., Maraston C., Padmanabhan N., Prada F., Ramos B., Sanchez A., Schlafly E. F., Schlegel D. J., Schneider D. P., Skibba R., Thomas D., Weaver B. A., White M., Zehavi I., 2011, Monthly Notices of the Royal Astronomical Society, 417, 1350 15

Ross N., da Angela J., Shanks T., Wake D., Cannon R., Edge A., Nichol R., Outram P., Colless M., Couch W., et al., 2007, Monthly Notices of the Royal Astronomical Society: Letters, 381, 573 7, 38, 47

Schlegel D., Abdalla F., Abraham T., Ahn C., Allende Prieto C., Annis J., Aubourg E., Azzaro M., Baltay S. B. C., Baugh C., Bebek C., Becerril S.,

Blanton M., Bolton A., Bromley B., Cahn R., Carton P. ., Cervantes-Cota J. L., Chu Y., Cortes M., Dawson K., Dey A., Dickinson M., Diehl H. T., Doel P., Ealet A., Edelstein J., Eppelle D., Escoffier S., Evrard A., Faccioli L., Frenk C., Geha M., Gerdes D., Gondolo P., Gonzalez-Arroyo A., Grossan B., Heckman T., Heetderks H., Ho S., Honscheid K., Huterer D., Ilbert O., Ivans I., Jelinsky P., Jing Y., Joyce D., Kennedy R., Kent S., Kieda D., Kim A., Kim C., Kneib J. ., Kong X., Kosowsky A., Krishnan K., Lahav O., Lampton M., LeBohec S., Le Brun V., Levi M., Li C., Liang M., Lim H., Lin W., Linder E., Lorenzon W., de la Macorra A., Magneville C., Malina R., Marinoni C., Martinez V., Majewski S., Matheson T., McCloskey R., McDonald P., McKay T., McMahon J., Menard B., Miralda-Escude J., Modjaz M., Montero-Dorta A., Morales I., Mostek N., Newman J., Nichol R., Nugent P., Olsen K., Padmanabhan N., Palanque-Delabrouille N., Park I., Peacock J., Percival W., Perlmutter S., Peroux C., Petitjean P., Prada F., Prieto E., Prochaska J., Reil K., Rockosi C., Roe N., Rollinde E., Roodman A., Ross N., Rudnick G., Ruhlmann-Kleider V., Sanchez J., Sawyer D., Schimd C., Schubnell M., Scoccimaro R., Seljak U., Seo H., Sheldon E., Sholl M., Shulte-Ladbeck R., Slosar A., Smith D. S., Smoot G., Springer W., Stril A., Szalay A. S., Tao C., Tarle G., Taylor E., Tilquin A., Tinker J., Valdes F., Wang J., Wang T., Weaver B. A., Weinberg D., White M., Wood-Vasey M., Yang J., Yeche X. Y. C., Zakamska N., Zentner A., Zhai C., Zhang P., 2011, ArXiv e-prints 38

Schrabback T., Hartlap J., Joachimi B., Kilbinger M., Simon P., Benabed K., Bradač M., Eifler T., Erben T., Fassnacht C. D., High F. W., Hilbert S., Hildebrandt H., Hoekstra H., Kuijken K., Marshall P. J., Mellier Y., Morganson E., Schneider P., Semboloni E., van Waerbeke L., Velander M., 2010, AAP, 516, A63 3

Senevirathne K. W. P. B., 2010, Probing the large-scale galaxy density and peculiar velocity fields 75

Seo H., Eisenstein D. J., 2003, ApJ, 598, 720 65

Sherwin B. D., Dunkley J., Das S., Appel J. W., Bond J. R., Carvalho C. S., Devlin M. J., Dünner R., Essinger-Hileman T., Fowler J. W., Hajian A., Halpern

M., Hasselfield M., Hincks A. D., Hlozek R., Hughes J. P., Irwin K. D., Klein J., Kosowsky A., Marriage T. A., Marsden D., Moodley K., Menanteau F., Niemack M. D., Nolta M. R., Page L. A., Parker L., Reese E. D., Schmitt B. L., Sehgal N., Sievers J., Spergel D. N., Staggs S. T., Swetz D. S., Switzer E. R., Thornton R., Visnjic K., Wollack E., 2011, Physical Review Letters, 107, 021302 3

Silberman L., Dekel A., Eldar A., Zehavi I., 2001, ApJ, 557, 102 15, 17, 33, 34

Simpson F., Peacock J. A., 2010, PRD, 81, 043512 44, 45, 48

Smith R. E., Peacock J. A., Jenkins A., White S. D. M., Frenk C. S., Pearce F. R., Thomas P. A., Efstathiou G., Couchman H. M. P., 2003, MNRAS, 341, 1311 ii, 9, 23

Smoot G. F., Bennett C. L., Kogut A., Wright E. L., Aymon J., Boggess N. W., Cheng E. S., de Amici G., Gulkis S., Hauser M. G., Hinshaw G., Jackson P. D., Janssen M., Kaita E., Kelsall T., Keegstra P., Lineweaver C., Loewenstein K., Lubin P., Mather J., Meyer S. S., Moseley S. H., Murdock T., Rokke L., Silverberg R. F., Tenorio L., Weiss R., Wilkinson D. T., 1992, APJL, 396, L1 14

Spergel D. N., Verde L., Peiris H. V., Komatsu E., Nolta M. R., Bennett C. L., Halpern M., Hinshaw G., Jarosik N., Kogut A., Limon M., Meyer S. S., Page L., Tucker G. S., Weiland J. L., Wollack E., Wright E. L., 2003, The Astrophysical Journal Supplement Series, 148, 175 3

Springob C. M., Masters K. L., Haynes M. P., Giovanelli R., Marinoni C., 2009a, ApJl, 182, 474 18, 22

—, 2009b, VizieR Online Data Catalog, 217, 20599 18, 22

Tegmark M., 1997, Physical Review Letters, 79, 3806 42, 65

Tegmark M., Eisenstein D. J., Strauss M. A., Weinberg D. H., Blanton M. R., Frieman J. A., Fukugita M., Gunn J. E., Hamilton A. J. S., Knapp G. R., Nichol R. C., Ostriker J. P., Padmanabhan N., Percival W. J., Schlegel D. J.,

Schneider D. P., Scoccimarro R., Seljak U., Seo H., Swanson M., Szalay A. S., Vogeley M. S., Yoo J., Zehavi I., Abazajian K., Anderson S. F., Annis J., Bahcall N. A., Bassett B., Berlind A., Brinkmann J., Budavari T., Castander F., Connolly A., Csabai I., Doi M., Finkbeiner D. P., Gillespie B., Glazebrook K., Hennessy G. S., Hogg D. W., Ivezić Ž., Jain B., Johnston D., Kent S., Lamb D. Q., Lee B. C., Lin H., Loveday J., Lupton R. H., Munn J. A., Pan K., Park C., Peoples J., Pier J. R., Pope A., Richmond M., Rockosi C., Scranton R., Sheth R. K., Stebbins A., Stoughton C., Szapudi I., Tucker D. L., vanden Berk D. E., Yanny B., York D. G., 2006, PRD, 74, 123507 9, 67, 68

The Dark Energy Survey Collaboration, 2005, ArXiv Astrophysics e-prints 38

Thomas S. A., Abdalla F. B., Lahav O., 2010, ArXiv e-prints 14

Trotta R., 2008, icosmos 3, 4

Tully R. B., Fisher J. R., 1977, AAP, 54, 661 13

Uomoto A., Smee S., Rockosi C., Burles S., Pope A., Friedman S., Brinkmann J., Gunn J., Nichol R., SDSS Collaboration, 1999, in Bulletin of the American Astronomical Society, Vol. 31, American Astronomical Society Meeting Abstracts, p. 1501 74

Verde L., Heavens A. F., Percival W. J., Matarrese S., 2002, ArXiv Astrophysics e-prints 74

Viel M., Haehnelt M. G., Springel V., 2004, MNRAS, 354, 684 7, 38

Wang Y., Percival W., Cimatti A., Mukherjee P., Guzzo L., Baugh C. M., Carbone C., Franzetti P., Garilli B., Geach J. E., Lacey C. G., Majerotto E., Orsi A., Rosati P., Samushia L., Zamorani G., 2010, MNRAS, 409, 737 38, 44

Watkins R., Feldman H. A., Hudson M. J., 2009, MNRAS, 392, 743 ii, 14, 16, 17, 18, 22, 35

White M., Song Y.-S., Percival W. J., 2009, MNRAS, 397, 1348 44

Zaroubi S., Bernardi M., da Costa L. N., Hoffman Y., Alonso M. V., Wegner G., Willmer C. N. A., Pellegrini P. S., 2001, MNRAS, 326, 375 15

Zaroubi S., Zehavi I., Dekel A., Hoffman Y., Kolatt T., 1997, ApJ, 486, 21 15

Zuntz J., Baker T., Ferreira P., Skordis C., 2011, ArXiv e-prints 59